January 2014

Insights into the Epitaxial Relationships between One-Dimensional Nanomaterials and Metal Catalyst Surfaces Using Density Functional Theory Calculations

Debosruti Dutta
University of South Florida, dutta.debosruti@gmail.com

Insights into the Epitaxial Relationships between One-Dimensional Nanomaterials and Metal Catalyst Surfaces Using Density Functional Theory Calculations

by

Debosruti Dutta

A dissertation submitted in partial fulfillment
of the requirements for the degree of
Doctor of Philosophy
Department of Chemical and Biomedical Engineering
College of Engineering
University of South Florida

Major Professor: Venkat R. Bhethanabotla, Ph.D.
Babu Joseph, Ph.D.
John N. Kuhn, Ph.D.
Anna Pyayt, Ph.D.
Rudy Schlaf, Ph.D.
Matthias Batzill, Ph.D.

Date of Approval:
June 18, 2014

Keywords: SWCNT, InAs nanowires, CVD, chiral-selectivity, growth orientation

DEDICATION

To Dr. Upama Dutta, thank you.

ACKNOWLEDGMENTS

I express my sincere gratitude to Prof. Venkat R. Bhethanabotla for giving me a chance to work on my dissertation work and for constantly motivating to work harder and bring out the best of me. I would also like to thank Dr. Babu Joseph, Dr. John Kuhn, Dr. Anna Pyayt, Dr. Rudy Schlaf and Dr. Matthias Batzill for serving on my committee and helping me immensely in structuring my dissertation.

A major part for the success of my research work can be attributed to Prof. Mohan Sankaran at the Case Western Reserve University. He is instrumental in formulating many of the ideas discussed in the dissertation and also, took an active interest in transforming the obtained results in to published papers. Discussions with him have helped substantially in completing the various projects in this dissertation.

I thank all my labmates Debtanu, Parveen, Mandek, Sam, Chi-Ta, Nianthrini and Kassie for creating a congenial work atmosphere with a special mention of Debtanu for helping me write-up many parts of the dissertation. I enjoyed the company of my good friends Upama, Shubhabrata, Subhronil, Nitya, Kartikay and Nilesh, who made my stay in USF memorable.

Last but not the least, sincere gratitude to my parents, my sister and my brother-in-law. My family has been very supportive and encouraging during these years. I thank all my teachers for their guidance that helped me attain this position.

TABLE OF CONTENTS

LIST OF TABLES

LIST OF FIGURES

ABSTRACT

This dissertation involves the study of epitaxial behavior of one-dimensional nanomaterials like single-walled carbon nanotubes and Indium Arsenide nanowires grown on metallic catalyst surfaces. It has been previously observed in our novel microplasma based CVD growth of SWCNTs on Ni-Fe bimetallic nanoparticles that changes in the metal catalyst composition was accompanied by variations in the average metal-metal bond lengths of the nanoparticle and that in turn, affected nanotube chirality distributions. In this dissertation, we have developed a very simplistic model of the metal catalyst in order to explain the nanotube growth of specific nanotube chiralities on various Ni-Fe catalyst surfaces. The metal catalyst model is a two-dimensional flat surface with varying metal-metal bond lengths and comprising of constituent metal atoms. The effect of the composition change was modeled as a change in the bond length of the model catalyst surface and density functional theory based calculations were used to study specific nanotube caps. Our results indicated that nanotube caps like (8,4) and (6,5) show enhanced binding with increased metal-metal bond lengths in the nanoparticle in excellent agreement with the experimental observations. Later, we used this epitaxial nucleation model and combined with a previously proposed chirality-dependent growth rate model to explore better catalysts that will preferentially grow an enhanced chirality distribution of metallic nanotubes. From our DFT calculations and other geometrical considerations for nanotube growth, we demonstrated that the pure $Ni_{0.5}Cu_{0.5}$ metal nanoparticles and its lattice-strained surfaces can serve as a promising catalyst for enhanced growth of metallic nanotubes. Finally,

we extended this model of epitaxial growth to study the growth of <111>, <100> and <110>oriented nanowires on gold metal nanoparticles where a faster growth rate of <111> nanowires was previously observed in experiments on shaped nanoparticles than that on spherical nanoparticles. The DFT calculations indicated an enhanced growth selectivity of the <111>oriented nanowires on the Au(111) surfaces. However, the DFT results also show that the <110> and <100> NWs will preferentially grow on the Au(100) surface than on the Au(100) surface. The epitaxial model based DFT calculations of nanotube and nanowire growth on metal catalyst surfaces presented in this dissertation, provide a deep insight into their epitaxial growth mechansims and, can be easily exploited to layout better design principles of synthesizing catalysts that helps in growing these one-dimensional nanomaterials with desired material properties.

CHAPTER 1: INTRODUCTION

1.1 Dimensionality of Materials

The reduction of dimensionality in a material can create new materials that have properties significantly different from that of the bulk material properties. For example, the reduction of dimensionality in carbon gives rise to a wide variety of nanomaterials each with distinct structure and very exciting material properties. Figure 1.1 shows a few examples of nannomaterials available at each dimension of the carbonaceous material. The 3-dimensional (3D) carbon structure naturally exists in the form of diamond or graphite (Figure 1.1(a)). On reducing dimension to 2D, 1D and 0D; we obtain graphene, SWCNT and fullerene respectively (refer to Figures 1.1 (b), (c) and (d)). In this dissertation, we focus on the one-dimensional nanomaterials that are characterized by their high aspect ratios and anisotropic properties that make them suitable for a wide variety of applications.

1.2 One-Dimensional Nanomaterials

One-dimensional nanoscale materials (1D nanomaterial) such as single-walled carbon nanotubes (SWCNTs) and semiconductor nanowires (s-NWs) have attracted a great deal of interest for potential applications in advanced electronics, optical devices, sensors, renewable energy, and biology. 1D nanomaterials exhibit interesting and unparalleled properties due to effects of quantum confinement. For example, SWCNTs are capable of carrying enormous current densities, and can be either metallic or semiconducting depending on their atomic-scale structure, and III-V materials such as InAs NWs are characterized by high electron mobilities,

polarizable photoluminescence, and strong spin-orbit interactions. Both these 1D nanomaterials are grown by the metal-catalyzed chemical vapor deposition (CVD) method and over the years extensive research has enabled the growth of 1D nanomaterials with pure crystalline structures, higher yields and faster growth rates. Despite tremendous progress, a significant obstacle that remains for 1D nanomaterial research and technologies is precise control over their structure (i.e. defects, crystalline orientation, etc.). In the case of SWCNTs, current synthetic approaches are unable to control the chirality which refers to the rolling direction of the graphene sheet. Different chiralities of SWCNTs, whose diameters may only vary by fractions of nanometers, can be metallic or semiconducting. Current growth methods typically produce 67% semiconducting and 33% metallic tubes, preventing their applications in electronics where a high purity of material of a single electronic type is required. Similarly, the crystal structure of s-NWs which influences their electronic and optical properties has not been sufficiently controlled for applications. In particular, III-V NWs are characterized by twin defects, stacking faults, and polytypism that result in lower quantum efficiency, carrier lifetime, and carrier mobility. A deeper theoretical understanding of the structure-property relationships between the metal catalysts and 1D nanomaterials has been lacking. In this dissertation work, we have used Density Functional Theory (DFT) calculations to gain a deep insight into the epitaxial relationship between the structure of the metal catalyst surfaces and the properties of the 1D nanomaterials, such as the chirality and metallic behavior of SWCNTs and the growth orientation and phase stability of InAs nanowires. The dissertation work revolves around three major projects outlined below in the following section.

1.3 Outline of the Dissertation

In chapter 2, we detail the structural and electronic properties of one-dimensional nanomaterials like single-walled carbon nanotubes and semiconducting nanowires. In addition, we discuss the growth mechanism of these one-dimensional materials and also review the current literature involved in the epitaxial growth of these materials on different metal catalyst surfaces.

In chapter 3, we outline the basic principles of electronic structure theory. The role of density functional theory in providing a practical and an extremely accurate solution of the Schrödinger equation of many-body systems is explained. Finally, the implementation of the DFT code in the Vienna *ab-initio* software package (VASP) is discussed.

Chapter 4 deals with achieving narrow-chirality distributions of SWCNTs grown on various compositions of Ni_xFe_{1-x} bimetallic nanoparticles and understanding how the chirality can be controlled by changing the composition of the bimetallic nanoparticle. We have used DFT calculations to model cap nucleation on bimetallic catalyst surfaces and find that an epitaxial relationship between the bimetallic catalyst and the cap structure supports the preferential growth of specific nanotube chiralites. Our DFT calculations show that chiralities such as (8,4) and (6,5) are more stable on surfaces corresponding to $Ni_{0.27}Fe_{0.73}$ nanoparticles, while chiralities such as (9,4) and (8,6) are more stable on surfaces corresponding to Ni catalysts, in excellent agreement with experiments. Based on our DFT calculations, we conclude that tuning the composition of the metal nanoparticles changes the average metal-metal bond length in the nanoparticle and that in turn changes the nanotube chirality distributions.

In chapter 5, we explored the chiral enrichment of metallic nanotubes grown on Ni, Cu and Ni_xCu_{1-x} nanoparticles by studying nanotube cap nucleation and the nanotube growth rates of various nanotube chiralities. We used the epitaxial nucleation model developed in chapter 4 to

explore the binding strengths of various nanotube cap chiralities. Nanotube growth on various catalyst surfaces is studied by calculating differences in armchair and zigzag dangling bond energies, relative chemical activity ratios and nanotube growth rates of various nanotube chiralities. Based on the binding strengths of various nanotube chiralities obtained from the DFT calculations and the relative chemical activity ratios and the nanotube growth rates, obtained from differences in the armchair and zigzag dangling bond energies on various catalyst surfaces, we conclude that the Ni_xCu_{1-x} bimetallic nanoparticles with increased bond length or lattice-strained surfaces can be excellent metal catalysts in growing metallic nanotubes preferentially.

In chapter 6, we have explored the epitaxial relationship between the growth orientations of the InAs nanowires (NWs) grown on shaped Au nanoparticles. We have studied the epitaxial growth of small fragments of wurtzite (WZ) and zinc blende (ZB) phases of InAs nanowires (NW) and nanotubes (NT) with growth orientations of <111>, <100>and <110>on Au(111) and Au(100) surfaces. From our DFT calculations and electron charge redistribution calculations, we find an epitaxial growth selectivity of the <111> and <100>/<110>orientation of the InAs NWs with the Au(111) and Au(100) surfaces respectively.

In Chapter 7, we summarize the major findings of this dissertation and then conclude with general guidelines for future research directions to explore the epitaxial growth of these one-dimensional nanomaterials on metal nanoparticles.

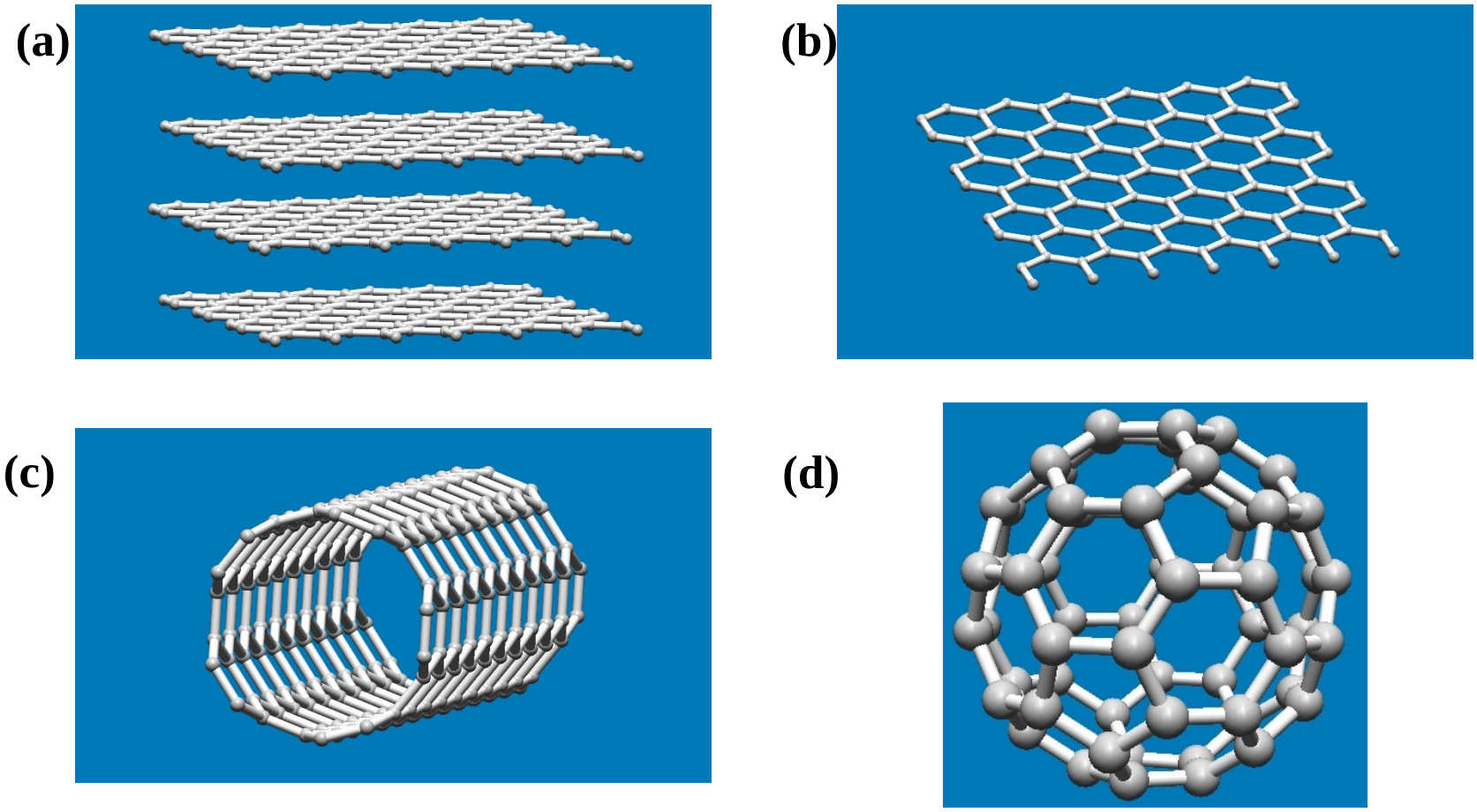

Figure 1.1: Dimensionality of nanomaterials: (a) 3D bulk graphite, (b) 2D graphene, (c) 1D SWCNT and (d) 0D Fullerene.

CHAPTER 2: ONE-DIMENSIONAL NANOMATERIALS: STRUCTURE, PROPERTIES, GROWTH AND EPITAXIAL BEHAVIOR

2.1 Introduction

In this chapter, we discuss the structural and electronic properties as well as the epitaxial growth mechanisms of one-dimensional nanomaterials like single-walled carbon nanotubes (SWCNTs) and semiconducting nanowires (s-NWs). There is an intimate relation between the structure and the properties of these one-dimensional nanomaterials. Hence, a detailed understanding of their atomic structure is imperative for tailoring their mechanical, electronic and photonic properties that can be exploited for a wide variety of commercial applications. Another important aspect is that the metal-catalyzed growth of these nanostructures is significantly influenced by choice of the metal nanoparticle and the reaction conditions like temperature and total pressure. A promising potential exists for tuning the growth parameters to yield specific nanostructures with distinct properties. Thus, a detailed understanding of the influence of the growth parameters on the as-grown nanostructures can help in growing these 1D nanomaterials with desired properties. In particular, we have discussed here how the chirality of a SWCNT and the growth orientation of InAs NW are influenced by the epitaxial relationship with the structure of the metallic nanoparticles.

2.2 Carbon Nanotubes

Carbon nanotubes are a class of one-dimensional nanomaterial called nanotubes which have a general cylindrical geometry with the tube diameter ranging from 0.3-10 nm and the tube

length can go as long as a few μm. Carbon nanotubes are the most commonly known as nanotubes though nanotubes of III-V materials like Boron-Nitride, Indium-Arsenide, etc. have also been observed. Among the nanotube materials, the carbon nanotubes have received huge interest over the last two decades for their extremely unique mechanical, optical and electronic properties. Carbon nanotubes are made of carbon atoms arranged in a cylindrical tube at the nanoscale. Carbon in its natural form exists in various allotropes like diamond and graphite with extremely different properties. Diamond is one of the hardest known materials and is used in cutting metals as the atoms in diamond form strongly bound sp^3-hybridized bonds. On the other hand, the graphite is used as a lubricant as graphite has a layered structure with in-plane sp^2-hybridized bonds in each layer but weakly bound carbon layers interacting through van der Waals interaction. The self-assembly of the carbon atoms at the nanoscale results in bond formation among the carbon atoms eventually leading to a growth of one-dimensional carbon chains and then, two-dimensional carbon mats. Under the correct growth conditions, these carbon chains and mats can form a wide variety of nanostructures like fullerenes, graphene sheets, carbon nanorods, carbon nanoribbons, carbon nanocones, carbon nanowhiskers, carbon nanoflowers, carbon nanoonions, carbon nanobulbs, carbon nanopipettes, multi-walled carbon nanotubes (MWCNTs) and single-walled carbon nanotubes (SWCNTs).

The nanoscale dimensions of the CNTs lead to quite interesting and often unexpected properties due to effects of quantum confinement. CNTs have unusually highly electrical conducting properties, exceptionally high mechanical strength and excellent thermal conducting properties. Based on these unique properties of the CNTs, many potential applications have been explored, including the use of nanotubes as field-effect transistors, nanoprobe tips, storage or filtering media and nanoscale electronic devices.

2.2.1 Structure and Chirality

The single-walled carbon nanotube has a hollow cylinder like structure. It can be imagined to be built of a rolled up sheet of hexagonal-oriented carbon atoms, called graphene. Many other properties can be derived from the properties of graphene (graphene sheet model) which serves as the basis for the nanotube structure and allows deriving the properties through boundary conditions/restrictions. A SWCNT, consists of only one wall, however, the way the atoms arrange on the wall, called chirality, determines the properties of the single-walled carbon nanotube. For example, the electronic band structure follows from the arrangement of the carbon atoms on the tube wall, called chirality.

We first describe the geometry of the 2D graphene model and then, we demonstrate how the chirality of the nanotube can be derived from this model. The nanotube can be atomistically modeled as a rolled up sheet of graphene, a planar sheet of carbon atoms arranged in a honeycomb lattice. Figure 2.1(a) shows the description of the geometrical parameters of the nanotube that can be derived from the graphene sheet model. The grapheme basis has two carbon atoms at $0.(\overrightarrow{a_1}+\overrightarrow{a_2})$ and $\frac{2}{3}.(\overrightarrow{a_1}+\overrightarrow{a_2})$, as shown at the right side of 2.1(a). To generate the structure of a nanotube of a certain chirality only two carbon atoms and some symmetry considerations are needed.[1,2] The two atoms are mapped onto a cylinder and the application of axial rotations and screw operations allow generating the positions of the other atoms.[1] The graphene basis vectors $\overrightarrow{a_1}$ and $\overrightarrow{a_2}$ form an angle of 60ºand can be defined as

$$\overrightarrow{a_1} = a\overrightarrow{e_1} = a\,.(1,0) \tag{2.1}$$

$$\overrightarrow{a_2} = \frac{a}{2}\overrightarrow{e_1} - \frac{\sqrt{3}}{2}\overrightarrow{e_2} = a\,.\left(\frac{1}{2}, -\frac{\sqrt{3}}{2}\right) \tag{2.2}$$

where, $a = \sqrt{3}d_{C-C} = 2.461$ Å, is the graphene lattice constant, $d_{C-C} = 1.421$ Åis the carbon-carbon bond length, and $\overrightarrow{e_1}, \overrightarrow{e_2}$are the unit vectors in ***x*** and ***y*** direction of the cartesian coordinate system shown at the right hand side of Figure 1(a). Rolling the graphene sheet around the circumference allows to completely define the geometry of the CNT by the two chiral indices (n,m) which specify the relative positions of two points on the hexagonal sheet of carbon atoms. The circumference of the rolled up sheet yields the chiral vector as:

$$\overrightarrow{C_h} = n\overrightarrow{a_1} + m\overrightarrow{a_2} \tag{2.3}$$

The chiral vector defines the chirality of any nanotube and joining the carbon atoms at the two ends of this chiral vector defines the circumference of the nanotube. The diameter of a nanotube can be derived from the formula of the circumference of a circle, representing the 2D projection along the tube axis of the cylindrical tube as

$$d = \frac{\left|\overrightarrow{C_h}\right|}{\pi} = \frac{a}{\pi}\sqrt{n^2 + nm + m^2} = \frac{a}{\pi}\sqrt{N} \tag{2.4}$$

with $N = n^2 + nm + m^2$ and $a = 2.461$ Å is the graphene lattice constant. As shown in Figure 2.1(a), the chiral angle θ is measured clockwise from $\overrightarrow{a_1}$ to the circumferential vector is given as:

$$\begin{aligned} \theta &= \cos^{-1}\left(\frac{\overrightarrow{a_1}.\overrightarrow{C_h}}{|\overrightarrow{a_1}|.\left|\overrightarrow{C_h}\right|}\right) = \cos^{-1}\left(\frac{2n+m}{2\sqrt{n^2+nm+m^2}}\right) \\ &= \tan^{-1}\left(\frac{\sqrt{3}m}{2n+m}\right) \end{aligned} \tag{2.5}$$

As shown in Figure 2.1(b), the chiral angle is ordinarily defined for 0 to 30° where the chiral angles of 0° and 30° refers to a zigzag (n,0) and armchair (n,n) nanotubes respectively and the intermediate chiral angles refer to chiral nanotubes. The translational vector describes the translational symmetry along the tube axis and can be represented in terms of the lattice vectors and chiral indices (n,m) as

$$\overrightarrow{T_h} = (2m + n)\overrightarrow{a_1} - (2n + m)\overrightarrow{a_2} \tag{2.6}$$

As shown in Figure 2.1(a), it can be constructed perpendicular to the circumferential vector $\overrightarrow{C_h}$ lying in the honeycomb lattice, which allows to determine the minimum translational repeat length along the nanotube axial direction by $T = \sqrt{3}\frac{|\overrightarrow{C_h}|}{L}$with $L = \gcd(2m + n, 2n + m)$, where gcd stands for the greatest common divisor.[1] This means$L = g$, with $g = \gcd(n, m)$, unless $\frac{(n-m)}{3g}$ is an integer, in that case $L = 3g$. The repeat unit of a nanotube along the cylindrical surface is the rectangular cross-sectional area formed by the translational repeat length along the nanotube axial direction *T* and the diameter *d* (refer to Figure 2.1(a)). The number of carbon atoms in the repeat unit can be quite large and that makes the DFT calculations of the nanotubes quite expensive. To estimate the number of the atoms in the repeat unit, we start with the number of atoms in a unit cell of graphene, which has 2 carbon atoms per unit cell. The area of the graphene unit cell can be calculated with$A_g = |\overrightarrow{a_1} \times \overrightarrow{a_2}| = \frac{\sqrt{3}}{2}a^2$. The area of the strip that is rolled up to form the minimum sized translational unit cell of the nanotube is given by $A_T = \sqrt{3}\frac{|\overrightarrow{C_h}|}{L}\left|\overrightarrow{C_h}\right| = \sqrt{3}\frac{|\overrightarrow{C_h}|^2}{L} = \sqrt{3}a^2(n^2 + nm + m^2)/L$. The number of carbon atoms in the unit cell n_c follows from the number of hexagons contained in the translational unit cell multiplied by 2:

$$n_c = 2\frac{A_T}{A_g} = 4\frac{(n^2 + nm + m^2)}{L} \tag{2.7}$$

with $n_C = 4g$ for chiral tubes.

The importance of controlling the chirality of the nanotube stems from the fact that the chirality of the nanotube governs the electronic properties i.e. the metallic/semiconducting behavior of the nanotube.[3,4] We can use the graphene sheet model to derive the electronic

properties of the nanotube in the following way. Figure 2.2 shows the first Brillouin zone, the reciprocal lattice vectors and the high symmetry k-points in the graphene lattice. The reciprocal lattice vectors of the graphene sheet can be calculated from the graphene basis vectors $\overrightarrow{a_1}, \overrightarrow{a_2}$.as

$$\overrightarrow{k_1} = \frac{2\pi}{a}\overrightarrow{e_1} + \frac{2\pi}{\sqrt{3}a}\overrightarrow{e_2} = \frac{2\pi}{a}\left(1, \frac{1}{\sqrt{3}}\right) \tag{2.8}$$

$$\overrightarrow{k_2} = -\frac{4\pi}{\sqrt{3}a}\overrightarrow{e_2} = \frac{2\pi}{a}\left(0, -\frac{2}{\sqrt{3}}\right) \tag{2.9}$$

$$\overrightarrow{k_3} = \frac{2\pi}{a}\overrightarrow{e_3} = \frac{2\pi}{a}(0,0,1) \tag{2.10}$$

This allows drawing the first Brillouin zone of graphene as shown in Figure 2.2. The high symmetry points can be found at

$$\Gamma = 0\,.\left(\overrightarrow{k_1} + \overrightarrow{k_2}\right) = (0,0) \tag{2.11}$$

$$K = \frac{1}{3}\,.\left(\overrightarrow{k_1} + 2\overrightarrow{k_2}\right) = \frac{2\pi}{a}\left(\frac{1}{3}, -\frac{1}{\sqrt{3}}\right) \tag{2.12}$$

$$M = \frac{1}{2}\overrightarrow{k_2} = \frac{2\pi}{a}\left(0, -\frac{1}{\sqrt{3}}\right) \tag{2.13}$$

The periodicity of the graphene lattice restricts the band structure to the first Brillouin zone.[1] The valence band and conduction band touch each other at the K points shown at the corners of the first Brillouin zone. The wave vectors of the K points are given with $\pm\frac{2\overrightarrow{k_1}+\overrightarrow{k_2}}{3}, \pm\frac{\overrightarrow{k_1}+2\overrightarrow{k_2}}{3}$and $\pm\frac{\overrightarrow{k_1}-\overrightarrow{k_2}}{3}$. By invoking a one-parameter tight-binding model with periodic boundary conditions for the circumferential vector as

$$\vec{k}.\overrightarrow{C_h} = 2\pi j \tag{2.14}$$

with integer *j*, we can determine whether a certain chirality is metallic or semiconducting.[1,3,4] The nanotube states are restricted to a set of parallel lines (as shown in red color in Figure 2.2 for

the (5,5) nanotube) in the reciprocal lattice of graphene by imposing the boundary conditions.[1,3,4] The red colored parallel lines are perpendicular to the chiral vector $\overrightarrow{C_h}$ and each parallel line corresponds to a different vale of *j* with the separation distance between the parallel lines given as $2\pi/\left|\overrightarrow{C_h}\right| = 2/D$.[1] Inserting the wavevector $\frac{\overrightarrow{k_1}-\overrightarrow{k_2}}{3}$ in the above equation yields the condition $n-m = 3j$, which means that about 1/3 of the nanotube chiralities will be metallic.[1] The other 2/3 of the nanotube chiralities are semiconducting with a bandgap that is inversely related to the diameter of the tube. Among all the metallic nanotubes, only the armchair tubes are truly metallic as the curvature shifts the lines slightly away from the K points, which leads to a small gap for tubes with bands of the same symmetry (non-armchair).

The precursor to the growth of an ultra-long cylindrical nanotube is the formation of a half fullerene nanostructure known as the nanotube cap. The nanotube cap forms the end structures of an ultra-long cylindrical nanotube. Figure 2.3 shows the structural relationship between the cylindrical nanotube, the nanotube cap and the fullerene structure with an example of the (5,5) nanotube. A capped (5,5) nanotube is shown with its constituents the hemispherical (5,5) nanotube cap and the cylindrical nanotube. The rim (highlighted in red) of the nanotube cap binds to the nanoparticle surface and plays an important role in the nucleation and the growth of the SWCNT by fixing the nanotube chirality. The nanotube cap structure can be derived from the structure of a fullerene and is in fact a half-fullerene as shown in Figure 2.3(d). According to the Euler criterion for curved surfaces, fullerenes require exactly 12 pentagons and rest hexagons to induce the curvature required to close them.[5] Since nanotube caps are half-fullerenes, they will have exactly 6 pentagons in their atomic structure to yield the curvature such that a nanotube can grow from it.[6,7] The rim of the nanotube cap has 3 distinct growth sites for the addition of carbon atoms viz. the armchair site (*aa.aa*), the zigzag site (*z.z*) and the kink site (*aa.z*). The

relative ease of carbon addition at these sites plays a key role for determining the growth rates of the nanotubes and hence, affecting the chirality distribution. Again the nanotube rim remains unchanged after 2 layers of carbon addition to the nanotube rim as shown in Figure 2.3(a) (highlighted in red and yellow). All these structural features of the nanotube caps are discussed in detail in chapters 4 and 5.

2.2.2 Nanotube Growth

There are primarily three different methods used to grow carbon nanotubes viz. arc discharge, laser ablation and chemical vapor deposition (CVD). Among these three growth techniques, the CVD method has become the most popular growth technique considering its scalability and the versatility in controlling the reaction parameters that enable chiral-selective growth.[8] The CVD growth method involves the thermal decomposition of a carbon precursor gas on a metal catalyst in a heating furnace. A wide variety of carbon precursor gases including CO and the hydrocarbons such as C_2H_2[9], C_2H_4[10], CH_4[9], CH_3OH[11] and C_2H_5OH[11] can be used to grow the SWCNT. There are primarily two modes of growth for the SWCNTs in the CVD method: the tip growth and the root-based growth. Figure 2.4 shows the schematic illustration for (a) the tip-based growth and (b) the root-based growth of the SWCNT on the metal nanoparticle. The tip growth model proceeds by the carbon atoms pushing the metal nanoparticle away from the substrate effectively lifting off the metal nanoparticle during the nanotube elongation. Two important factors are essential for the tip growth; firstly, the diffusion time of carbon atoms inside the bulk of the metal nanoparticle should be shorter than the time required by the carbon atoms to get saturated on the surface of the metal nanoparticle. Secondly, the gain in energy for the carbon atom in transferring from the metal nanoparticle to the nanotube should be higher than the adhesion energy between the metal and the substrate. In the root-based

growth mode, the metal nanoparticle remains attached to the substrate throughout the nanotube growth.[12] Once the surface of the metal nanoparticle is supersaturated with carbon atoms, it forms carbon chains and eventually lifts off as a nanotube cap. Further elongation of the nanotube proceeds by carbon atom addition at the base of nanotube (i.e. at the nanotube-nanoparticle interface). The primary requirement for the root-base growth method is moderate binding energy between the substrate and the metal nanoparticle, as strong interactions can flatten the nanoparticle thereby dampening the template effect of the metal nanoparticle on the nanotube. On the other hand, too weak interactions are detrimental to nanotube growth as the metal nanoparticle can become quite large for nanotube nucleation and can get encapsulated by amorphous carbon. In addition, there is a requirement for moderate binding energies between the carbon atoms and the metal nanoparticle as too strong adhesion strengths would prevent the nanotube cap to lift off from the nanoparticle surface and can result in the dome closure of the caps whereas, too weak carbon-metal adhesion strength can prevent the nucleation of the nanotube cap itself.[13,14]

Two basic models have been suggested for the growth of nanotubes, the vapor liquid-solid (VLS) model and the screw-dislocation model. The vapor-liquid-solid (VLS) model was first developed for the growth of silicon whiskers, which do not contain an axial screw dislocation making an impurity essential for the growth.[15] The impurity allows forming a liquid silicon-gold alloy droplet, which becomes saturated with silicon leading to the precipitation and growth of silicon atoms to a whisker.[15] For the nanotube growth the liquid droplet corresponds to a metal-carbide particle, which after saturation precipitates carbon atoms that grow into the nanotube.[12] The screw dislocation model is a standard model developed for the growth of crystals, which states that real crystals are not perfect. The imperfections, i.e. dislocations

ending in the surface with a screw component, serve as a site for the addition of a new layer and avoid the high energy barrier occurring for completed planes. The main paper on carbon nanotubes by Iijima suggested using a screw dislocation model to explain the growth of nanotubes, as the tubes can have spiral growth steps at the tube ends/rims.[16,17] Later Ding *et al.* used the model to derive dependence between the chirality and the growth rate of the nanotube.[18] They identified kinks (see *aa.z* growth sites) as low-energy-barrier addition sites for carbon atoms.[18] Following Ding *et al.* the growth is driven by a monotonous free energy decrease

$$\Delta G = -\Delta\mu \,.\, N \tag{2.15}$$

with "$\Delta\mu$ being the driving chemical potential drop between the carbon dissolved in the catalyst and its bound state in the tube lattice" and N the number of added carbon atoms.[18] However, only chiral tubes contain kinks during the whole elongation process, achiral tubes (armchair and zigzag) grow in layers. If a carbon layer is completed an activation energy $G^*$is required to initiate the growth of a new layer, which results from the under-coordinated carbon atoms at the newly emerging kinks.[18] This leads to the free energy decrease of

$$\Delta G = G^* - \Delta\mu \,.\, N \tag{2.16}$$

rendering the growth of achiral tubes significantly slower than compared to the growth of chiral tubes, if $G^* \gg k_b T$.[18]

In the following we present the detailed growth process of CNTs within the chemical vapor deposition method. The growth process of carbon nanotubes in the CVD method can be divided in four phases: the preparation/pretreatment phase, in which the catalyst and substrate are prepared[19,20] the nucleation phase, in which the nanotube caps form[21,22], the growth phase, in which the nanotubes elongate with a chirality dependent growth rate, and a termination phase, in which the growth ends.[20,23]

The aim of the preparation phase is to grow small clusters on a substrate as templates for the nanotube caps. Therefore a metal catalyst layer is epitaxially grown on a carefully chosen/designed substrate and a heat and/or plasma treatment induces the nucleation of catalyst particles due to inter-atomic diffusion and the difference in the surface free energy of the substrate and the metal catalyst. The pretreatment is often performed under a reducing gas atmosphere to increase the rate of reduction and sintering of metal clusters.

The introduction of a carbon precursor gas, initiates the nucleation phase. The precursor gas is generally accompanied by an etching buffer, and/or carrier gas to generate a gas flow in the system and to prevent the encapsulation of the catalyst particle, which likely terminates the growth.[20] The carbon precursor gas either impinges on the catalyst/substrate or it is partly decomposed in a plasma and the atoms impinge on the catalyst/substrate.[24] The precursor gas atoms adsorb at the catalyst surface to become decomposed in carbon atoms and a moiety of the precursor[24], meanwhile the etching gas removes excess carbon feedstock or prevents Ostwald ripening. The carbon atoms diffuse on the surface[24], sub-surface, or through the bulk of the catalyst and start to form carbon structures, e.g. chains, Y-like carbon chain junctions, or seed pentagons.[25,26] The carbon seed structures form curved graphene-like sheets through the curved template form of the catalyst.[25,26] The curvature is induced by the pentagons in the graphene-like sheets, which were found to be energetically favorable in the nucleation phase, as the bond saturation is increased due to the curvature.

The lift off of the graphene-like sheets in the form of a carbon nanotube cap ends the nucleation phase. The carbon nanotubes elongate with a chirality dependent growth rate without changing their chirality, as rearrangements of the chirality are costly.[27] Carbon atoms therefore add at the edge of the nanotube and elongate the tube until the growth phase is ended due to a

lack of carbon supply, named the termination phase.[20] The termination phase generally ends with the extraction of the nanotubes from the catalyst/substrate. The extracted nanotubes are then processed in a post processing phase for experiments or industrial use.

2.2.3 Chiral-selectivity and Epitaxial Behavior

In the earlier sections, we focused on the carbon vapor deposition (CVD) method and explained the nanotube growth mechanism in detail. Initial research on the nanotubes was aimed at growing nanotubes on various metal nanoparticles. When fabrication of nanotubes became relatively easy, researchers started focusing on the structure control at the mesoscopic level, that is, the alignment and growth orientation of the SWCNT arrays. The next stage was to focus on the structure control at the microscopic level, that is, the control of the length and diameter of the nanotubes and their overall yield. However, a great obstacle in their widespread usage in device applications comes from the inability to grow purely metallic or semiconducting nanotubes of distinct chiralities. Efforts have been made to control the chirality of the nanotube at the nucleation stage by growing nanotubes on a variety of metal and non-metal catalysts as well as by trying to separate the metallic and semiconducting nanotubes by various post-growth separation techniques. However, the control of growing a nanotube with a single chirality is the ultimate challenge in making their application widespread.

The physical appearance of CNT is black in color due to the agglomeration of individual nanotube chiraities. Nanotube solutions are mostly gray to black, depending on its concentration and the surfactant. Post-processing of the as-synthesized SWCNTs to separate the chiralities yields phases of various colors, representing an enrichment of nanotubes of certain chirality. Once separated the isolated tubes can be metallic, semi-metallic or semiconducting with various

bandgaps only depending on the way the atoms arrange on the tube surface, meaning the chirality.

A good starting point for chirality selection is to reduce the number of possible chiralities that can be accessed with the specific experimental growth conditions. Therefore a first step towards chirality selective growth is the preparation of the catalyst particles, as a strong correlation between the catalyst size and nanotube diameters has been suggested.[28] This makes the small diameter carbon nanotubes especially interesting for chirality selective growth, as the number of accessible chiralities is limited for diameters in a small diameter range. A narrow catalyst particle size distribution therefore leads to a narrow chirality distribution, simplifying the problem to select certain chirality.

An experimental study reported the enrichment of metallic tubes (91% up from 33%) due to the variation of the noble gas ambient during the thermal annealing of the catalysts.[29] The catalyst morphology changed in dependence of the noble gases ambient, which was suggested to demonstrate dependence between the catalyst morphology and the electronic structure of the grown carbon nanotubes. Another study reported enrichment of semiconducting tubes (88% up from 67%), especially of the (6,5) chirality (45%) due to the low temperature growth on a bimetallic FeCu/MgO catalyst.[30] A preferential growth of semiconducting nanotubes was suggested for smaller diameters, as their formation energy was found to be lower than the formation energy of semi-metallic and metallic tubes.[7] The use of bimetallic catalysts, e.g. NiFe[8], CoMo[31] was observed to lead to a narrowing of the chirality distribution.

It had been previously suggested that the formation energy for caps on a catalyst particle depend on the fit between the cap and the catalyst surface, which would allow designing catalyst particles that enhance the yield of certain chiralities in the nucleation phase.[2,32] This follows, as

the chirality of the nanotube grown from a specific nanotube cap is unique.[7] Another study, however, pointed out that only the diameter of the cap/nanotube can be controlled by the catalyst particle and excluded the chirality control.[33] The authors of the study argue, that the growth temperature required for the carbon diffusion on the catalyst would lead to a surface or bulk melting of the catalyst particle, preventing a lattice matched chirality selection mechanism.[33] They further argue, that the catalyst particles change their shape during the growth process even at low growth temperatures.[21] The catalyst particle was found to act as a template for the cap, while the cap also shapes the catalyst, meaning interplay of 'template' and 'inverse-template' effect, with a stronger effect from the catalyst on the nanotube.[34] Another study stated that the edge/surface energy of the nanotube (grapheme sheet) on the catalyst decides the chirality of the tube during the nucleation phase, as armchair and zigzag edge energies are different for different catalysts. The study, however, did not consider pentagons, 6 needed for the inclination of the cap[35,36] and neglected the change in the rim structure, especially the number of carbon addition sites, with every carbon addition.[37,38]

In an earlier study, the difference of the edge energy of armchair and zigzag sites on various metals had already been observed.[39] This difference in the edge energies of the armchair and zigzag sites was suggested to be the key parameter in governing the growth rate of the nanotube rim. If the chirality is "quenched" in the nucleation phase, the only way to change the yield of the chiralities during the elongation phase is by a chirality dependent growth rate.[37] The theoretical model presented by Ding *et al.* considers kinks as carbon addition sites and finds a linear dependence of the growth rate on the chiral angle.[18] In Dumlich *et al.*'s[37] growth model of a chirality dependent growth rate they extended the idea of Ding *et al.*'s model and included the influence of more external parameters, i.e. temperature and catalyst. They suggested that the key

is to manipulate the energy difference between armchair and zigzag dangling bonds through the choice of metal catalyst and growth conditions.[37] Recently, strong experimental evidence for the model of the chirality dependent growth rate was reported.[40] The experimental study used *in-situ* Raman spectroscopic measurements to determine the growth rates in dependence of the chirality and found that the growth rate of the tubes depends on their chirality. A recent growth model for the island growth of graphene of the Yakobson group[27] can be regarded as an extension to their previous growth models presented in the papers of Ding *et al.*[18] and Liu *et al.*[41]. In the extended version of the model various edge structures are considered and their energy stability is calculated.[27] This allows simulating the atom addition to a grapheme edge and deriving the addition probability to a certain site from the energy of the calculated edge configurations.[27] They find that the first carbon addition to a zigzag edge is strongly endoergic, and [the atom] is likely to fall back onto the substrate", which corresponds to a larger barrier for the growth of zigzag edges than for armchair edges.[27] After the first addition to the zigzag site the growth can occur very fast, as a kink site is created which grows without energy barrier.[27] The study further applied transition state theory and determined the decomposition rate of the nanotube to estimate an upper limit of the armchair growth rate (corresponding to the difference of carbon addition to the nanotube and decomposition of nanotube atoms) with, e.g., 1 mm/s for a growth temperature of 1300 K on Fe.

A recent study pointed out that the carbon solubility and wetting properties of catalyst nanoparticles are especially important to optimize the growth of nanotubes for specific chiralities.[42] The growth simulations of the study found that the wall of the nanotube cap grows parallel to the molten/surface-molten catalyst with addition of short carbon chains before the cap detaches and lifts off for elongation.[42] The nanotube stays connected to the catalyst through a

diffuse carbon network, which serves as carbon addition site.[42] *In-situ* transmission electron microscopy footage of the nanotube nucleation indicates that this growth model might be applicable for certain growth conditions[21], however, other growth conditions might lead to the conclusion that the cap elongates from the particle surface without the intermediate tangential growth step.[43] Another study which included the effect of the substrate found that the detachment of the cap depends on the adhesion energy between the catalyst and the substrate, as the capillary forces of the nanotube growth are counteracted by the substrate.[44] A high adhesion energy between the substrate and the catalyst particle were found to lead to a flattened shape of the catalyst particles with a low wetting angle.[44] The study further suggested that the occupation of hollow sites is a key factor to establish a good fit between the nanotube edge and the catalyst particle, which increases the interaction strength. The interplay between the adhesion energy and the strain energy was found to be important for the lift-off step of the cap, which was suggested to be chirality selective.

The chirality, however, does not necessarily need to remain constant during the nucleation process.[45] In a reactive molecular dynamics/Monte Carlo simulation which applied a force field (ReaxFF) a change of the chirality was observed during the nucleation process of the cap, which resulted from the restructuring of the cap structure due to the interaction with the metal catalyst.[45] Another study, which simulated preformed nanotube caps without a catalyst (in vacuum), found that the change of the chirality is possible with the addition of single carbon atoms to the edge of the nanotube cap, while the caps/tubes are elongated for carbon dimer addition.[46]

Even though extensive research effort has been put into the topic of chirality selective growth, it is still not possible to grow a specific chirality. It is not even clear, if chirality

selective growth is possible in the sense that certain growth conditions grow only one specific nanotube chirality. It has been shown, however, especially in the last few years, that the chirality distributions can be narrowed and certain control of the chirality is possible.[30,47] Combined with post processing, we are nowadays able to produce samples of only a few or even one chirality.[47,48] However, we still do not understand the details of the chirality selection completely.

In this dissertation in chapters 4 and 5, we have tried to address the issue of chiral-selectivity of SWCNTs by studying the epitaxial relationship of the as-grown SWCNTs on the metal catalyst nanoparticles. In chapter 4, we explain our experimental observations of enhanced growth of certain semiconducting chiralities like (8,4) and (6,5) nanotubes on Ni_xFe_{1-x} catalyst surfaces through an epitaxial nucleation model. In chapter 5, using a combination of the epitaxial nucleation model and a chirality-dependent growth rate proposed by Dumlich *et al.*[37], we predict suitable catalysts for the enhanced growth of metallic nanotube chiralities.

2.3 Semiconducting Nanowires

Among the various other 1D nanostructures, semiconducting nanowires (s-NWs) have attracted a great deal of interest for potential applications in advanced electronics[49], photonics[50], sensors[51] and energy conversion[52]. These 1D nanomaterials are ideal building blocks for nanoscale devices, similar in shape and geometry to wires, but reduced to the nanoscale where quantum confinement effects are present.[50] As a result, s-NWs exhibit interesting and unparalleled properties. For example, III-V materials such as InAs NWs are characterized by high electron mobilities[53], polarizable photoluminescence[54], and strong spin orbit interactions[55]. Various combination of materials have been used to synthesize semiconducting nanowires: group IV elements like diamond, Si or Ge; group II-VI compounds like ZnO, ZnS, ZnSe, CdSe,

CdS, CdTe and a large variety of group III-V nanowires like BN, BP, Bas, AlN, AlP, AlAs, AlSb, GaN, GaP, GaAs, GaSb, InN, InP, InAs, InSb. The reason for exploring such a wide variety of s-NWs stems from the fact that the bandgap range for these s-NWs can vary from 0.3-7 eV and bandgap type can be direct or indirect; such a wide variance in their properties makes them useful for a wide variety of electronic and photonic applications.

2.3.1 Structure and Phase Stabiltiy

Nanowire can be defined as a solid crystalline fiber having a cylindrical nanostructure where the diameter is confined to tens of nanometers but the length dimension is unconstrained along the axial direction. Structurally, the key feature that distinguishes the nanowire from the nanotube is that whereas all the carbon atoms of the nanotube have sp^2-hybridization and are entirely on the cylindrical surface, the interior of the nanowire consist of atoms forming tetrahedral bonds and the nanowire surface has atoms with dangling bonds. The diameter of the nanowire is the most important geometrical parameter for the stability of the nanowire as it governs the surface to bulk ratio of the atoms in the nanowire. This stability is governed by a competition between the expensive surface energy and a much lower bulk cohesive energy. A nanowire having lower atomic surface fraction stabilizes itself as the contribution of the expensive surface energy is much reduced.

Other important geometrical features of the nanowire are the nanowire orientation (axial direction), the areal cross-section and the surface facets. Table 2.1 lists the nanowire orientation, the areal cross-section (if known) and the size and possible defects of various nanowires as reported in the literature. The growth of the nanowires in specific orientations is important because the anisotropy of the nanowire determines various electronic and optical properties. The geometry of the areal cross-section and the orientation of the surface facets of the nanowire

influence the formation of crystal defects in the nanowire like stacking faults and twinning thereby affecting the overall purity and stability of the nanowire.

The phase purity of the nanowire is another important structural feature that affects its electronic properties. It is well-known that various compound semiconducting nanowires exhibit polytypism between wurtzite (WZ) and zinc blende (ZB) phases. The primary difference between the WZ and ZB phase is in the atomic layer stacking: whereas the WZ has a hexagonal closed packed (hcp) *ABAB…* stacking, the ZB has a face centered cubic (fcc) *ABCABC…* stacking. The bulk crystal structure for most III-V materials is the cubic zinc blende (ZB) whereas the nitrides exhibit hexagonal wurtzite (WZ) structure. However, a random intermixing of WZ and ZB structures separated by twinning planes is commonly observed for most III-V materials grown as nanowires. Since the WZ and ZB phase has different band structures, such intermixing of the WZ and ZB phases in the nanowire introduces abrupt band offsets at the interfaces. Also, the presence of various crystal defects at the interfaces like stacking faults and twinning planes as well as the kinking and branching of the nanowires during their growth can significantly affect the electronic, optical and thermal transport properties of the nanowires. It is quite clear that the presence of such defects and the random mixing of such nanowire structures can make them unsuitable for use in advanced nanoscale devices. Hence, the objective is to grow ultra-long phase-pure and defect-free nanowire arrays with specific growth orientations by suitably controlling the metal catalyst and the reaction conditions.

2.3.2 Nanowire Growth

Nanowires have been grown by a variety of techniques including chemical vapor deposition (CVD), laser ablation, supercritical fluid solution phase, metal organic chemical vapor deposition (MOCVD), chemical beam epitaxy (CBE) and molecular beam epitaxy (MBE).

Among these techniques, the CVD method has been the one that has been extensively researched because of its versatility and scalability. Similar to the growth of the carbon nanotubes, the growth method for CVD synthesis of s-NWs can be explained by the vapor-liquid-solid (VLS) growth mechanism, which describes the reaction of a vapor precursor with a metal nanoparticle (i.e. catalyst). Wagner and Ellis[15] were the first to describe the VLS mechanism in order to explain the growth of Si whiskers on Au metal nanoparticle. Figure 2.5 shows the schematic illustration of the VLS growth of Si whiskers on Au nanoparticles. At sufficiently high temperatures, the vapor precursor (or moieties of the precursor) diffuses into the solid metal particle and melts to form a liquid alloy. As more and more of the precursors diffuse into the particle, the particle is eventually saturated with the precursor. When the concentration of the precursor in the particle reaches super-saturation, a solid nanowire is nucleated.

The major role of the metal nanoparticle is to form a liquid alloy droplet with the reactant semiconductor gas such that the resultant liquid droplet has a relatively low freezing temperature that helps to readily nucleate and grow the nanowire. The size of the metal particle has been found to control the as-grown s-NW diameter.[56,57] As shown in Figure 2.5, the metal nanoparticle is present at the tip of the NW during growth and can influence the epitaxial growth of the nanowire. The obvious question that arises is that if the metal nanoparticle forms a liquid alloy droplet, the surface faceting of the nanoparticle is lost and hence, it cannot any epitaxial influence on the NW. However, in recent years, it has been shown that the nanowire growth can occur by a vapor-solid-solid (VSS) mechanism in which the reaction temperature is below the eutectic temperature and the metal nanoparticle remains solid during the growth process. In addition, the nanoparticle material is also important. Au is often used because of its low eutectic melting temperature which facilitates VLS growth; for example, the eutectic temperature for Au

and Si alloy is ~360 ^{o}C which allows Si NW growth at relatively low temperatures of ~400-500 ^{o}C.[15,57]

The striking feature of the VLS mechanism is its flexibility and versatility in growing a variety of complex nanostructures. For example, axial hetero-junctions in the nanowire can easily be introduced by modifying the reactant material precursors present in the reaction chamber.[58-60] On the other hand, radial hetero-junctions can be preferentially grown by increasing the reaction temperature as it suppresses the VLS growth and it enhances the deposition of material on the sidewalls of the nanowire.[61] Impurity doping for both n-type and p-type materials can be achieved by adding a suitable precursor.[62,63] Also, a wide variety of s-NWs can be grown as the induced strain of highly lattice-mismatched hetero-junctions can be easily accommodated through lateral relaxation.[64] This allows for efficient and robust growth of relatively defect-free s-NWs on highly dissimilar substrate materials (e.g. III–V nanowires on Si substrates[65]); an important feature that is quite difficult for nanowire growth on two-dimensional thin films. These unique properties have led to s-NWs being used for fabrication of a large variety of nanoscale devices including field-effect transistors[66,67], lasers[68], light-emitting diodes[69], photo detectors[70] and solar cells[71] among others.

2.3.3 Controlling Nanowire Growth Orientations by Epitaxial Growth on Metal Catalysts

Precise control over growth orientation of nanowires has several technological implications. For example, the large-scale manufacturing of vertical arrays of nanowire field-effect-transistors involves growing vertically aligned <111> oriented nanowires on (111) substrates.[72] Though there has considerable success in the lab-scale integration of small arrays of nanowires, commercial logic gate technologies based on nanowires will involve defect-free

growth of billions of vertically-aligned nanowires on a single chip. Again, from a fundamental scientific point of view, the growth direction of the nanowires can significantly affect the optical, electrical and mechanical properties of the nanowires and there can be useful applications of the nanowires that can be tailored by orientation and nanowire growth direction. Especially, the <111>B directional growth of the III–V semiconductors often exhibit a large number of stacking fault defects accompanied by polytypism that considerably degrades the electronic and optical performance characteristics of the device. Hence, the growth of nanowires in other directions like <100> and <110> is of great interest primarily due to the defect-free growth of nanowires in these directions.

The metal-catalyzed CVD growth of s-NWs via the VLS or VSS mechanisms, yield NWs with axial growth direction primarily in the <111> direction. Other low-index growth directions like <100>, <110> and <112> have also been occasionally reported. Table 2.1 lists all the typical nanowire growth orientations and areal cross-sections (if known) of several important nanowire materials. Nanowires tend to grow in a direction that minimizes the total free energy of the nanowire and in most cases; this free energy is dictated by the surface energy of the nanowire-nanoparticle interface. For cubic zinc-blende crystals like the Si, Ge, InAs, GaAs, etc. the most stable plane for the semiconductor-catalyst interface is the (111) surface and hence, most of these s-NWs tend to grow in the <111> direction. For compound III-V nanowires like GaAs, InAs, etc., the<111> nanowire orientation can be further differentiated into <111>A and <111>B directions due to differences in atomic layer stacking and hence, surface termination. The <111>B (group-V terminated) is the lower energy plane[73] and therefore nanowires have been generally observed to grow in the <111>B direction.[74] For nanowires with a wurtzite crystal structure, the commonly observed growth orientation is along the <0001>direction (*c*-

axis). However, there is no preference for nanowire growth orientation of III-nitride nanowires and growth axes perpendicular to the *a*-planes[75], *m*-planes[76,77] and *c*-plane[78] have been observed. In case of III–V nanowires, both the wurtziteand zinc blende crystal phases are observed and often, the grown nanowires exhibit polytypism[79] with alternating bands of zinc-blende and wurtzite atomic layering.

Another important feature is the growth orientation of the nanowires with the substrate. Figure 2.6 shows the growth orientations of <111> nanowires on both elemental and compound semiconducting substrates with 3 different substrate orientations viz. (111), (001) and (110). In particular, the <111>B growth direction has been highlighted in blue in each of the figures. The number of possible <111> growth directions on each substrate as well as the geometrical angles between the various <111> growth directions and their azimuthal angles with the substrate are reported for elemental semiconducting substrates in Table 2.2 and compound semiconducting substrates in Table 2.3. In recent years, planar nanowires that grow in-plane with the growth substrate have been fabricated that are more suitable for conventional planar processing techniques. In particular, planar ZnO nanowires have been grown on sapphire[80] and GaN[81] substrates and the epitaxial influence of the substrate on the planar nanowire has been demonstrated quite convincingly.

The primary advantage of a metal-catalyzed CVD growth of a s-NW is that a wide variety of reaction parameters can be easily controlled to obtain s-NWs with desired mechanical, optical and electronic properties. Among the various parameters possible, the common ones that can control the nanowire growth direction are as follows: (a) substrate crystal orientation effect, (b) effect of substrate surface treatment and catalyst initial condition, (c) diameter dependence of nanowire orientation, (d) reaction conditions: (i) temperature (ii) total pressure and precursor

partial pressure and (iii) III-V ratio. Although extensive research has been done in studying the effects of each of these parameters in growing specifically-oriented nanowire arrays, there have been very few studies to understand the effect of controlling the metal nanoparticle surface to influence the nanowire growth directions. This has been so because under the VLS mechanism the NW-metal particle interface is thought to be in a liquid state and hence, no epitaxial behavior is expected. However, an alternate vapor-solid-solid (VSS) mechanism of nanowire growth on some semiconducting substrates like NiGa[82] and Au-catalyzed metal nanoparticles has been observed. As mentioned earlier, Au is often used as a catalyst because it has a low eutectic reaction temperature and the gold seed nanoparticle is likely to remain solid. Hence, an epitaxial influence of the Au nanoparticle on the nanowire growth orientations can be expected. In particular, in a previous work[83], our collaborators at CWRU has shown that the InAs nanowires tend to grow at a faster rate on the shape-controlled Au nanoparticles than on spherical nanoparticles thereby implying that initial morphology of the metal nanoparticle can be utilized for tailoring the NW growth orientation. Inspired by these exciting experimental findings, in chapter 6, we have explored whether epitaxial relationships can be established between various growth orientations of InAs nanowires and various gold surfaces.

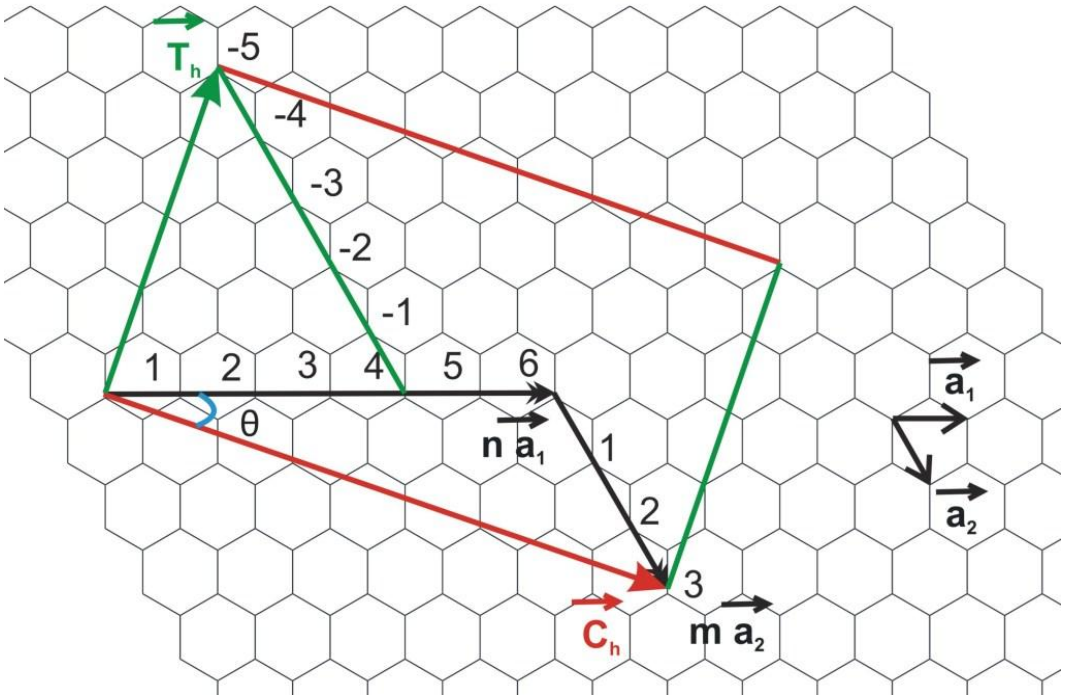

(a)

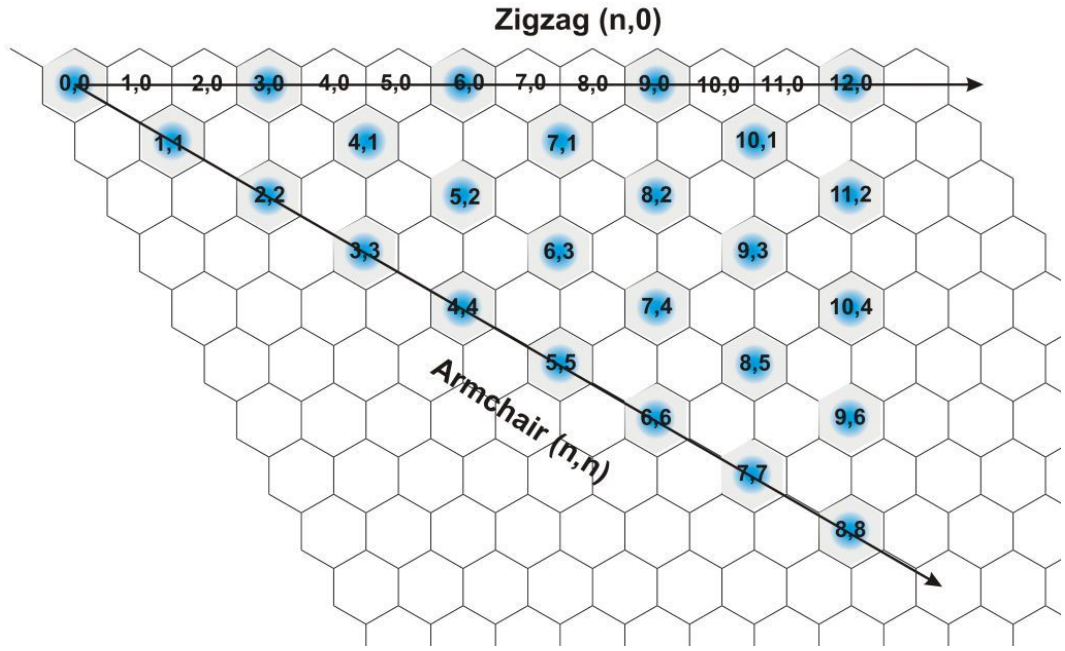

(b)

Figure 2.1: Chirality of SWCNTs derived from the graphene sheet model

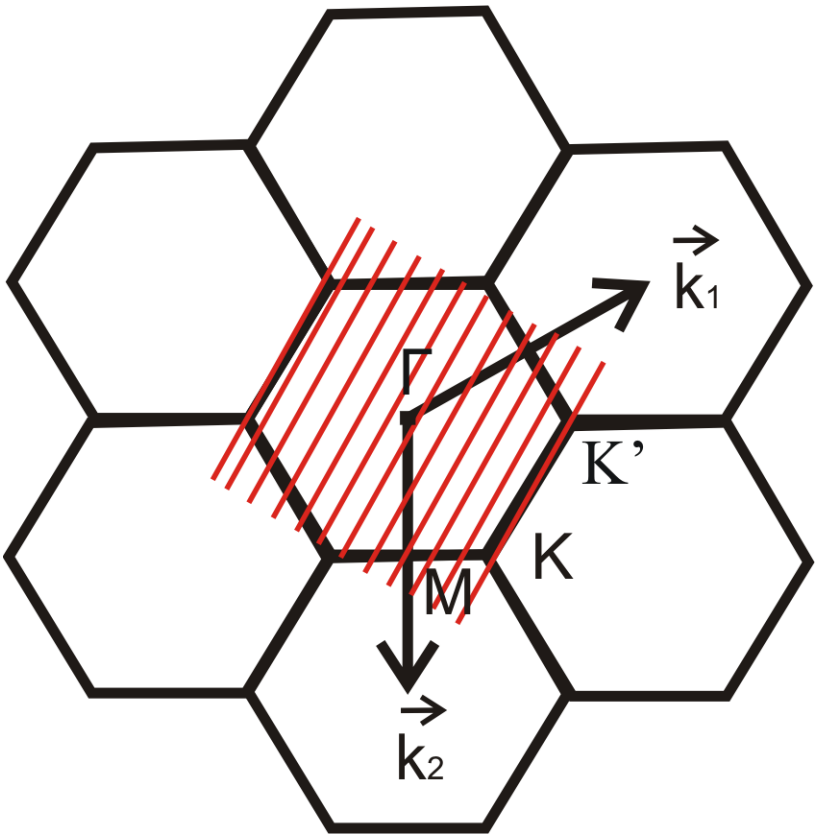

Figure 2.2: Metallic/semiconducting behavior of SWCNTs derived from the first Brillouin zone of graphene.

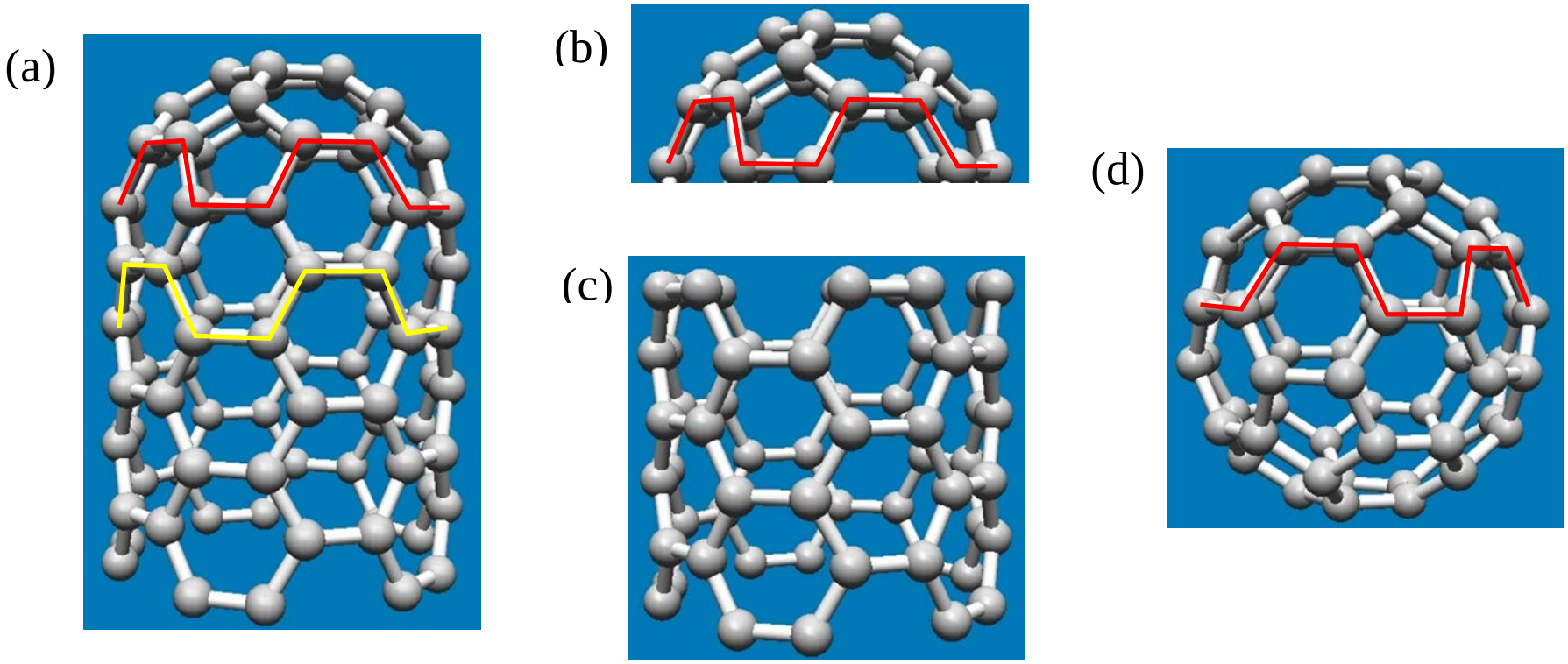

Figure 2.3: Structure of nanotube cap and fullerene in relation to the (5,5) SWCNT. (a) Capped SWCNT, (b) Isolated cap, (c) Isolated SWCNT and (d) Fullerene – C60 Bucky ball

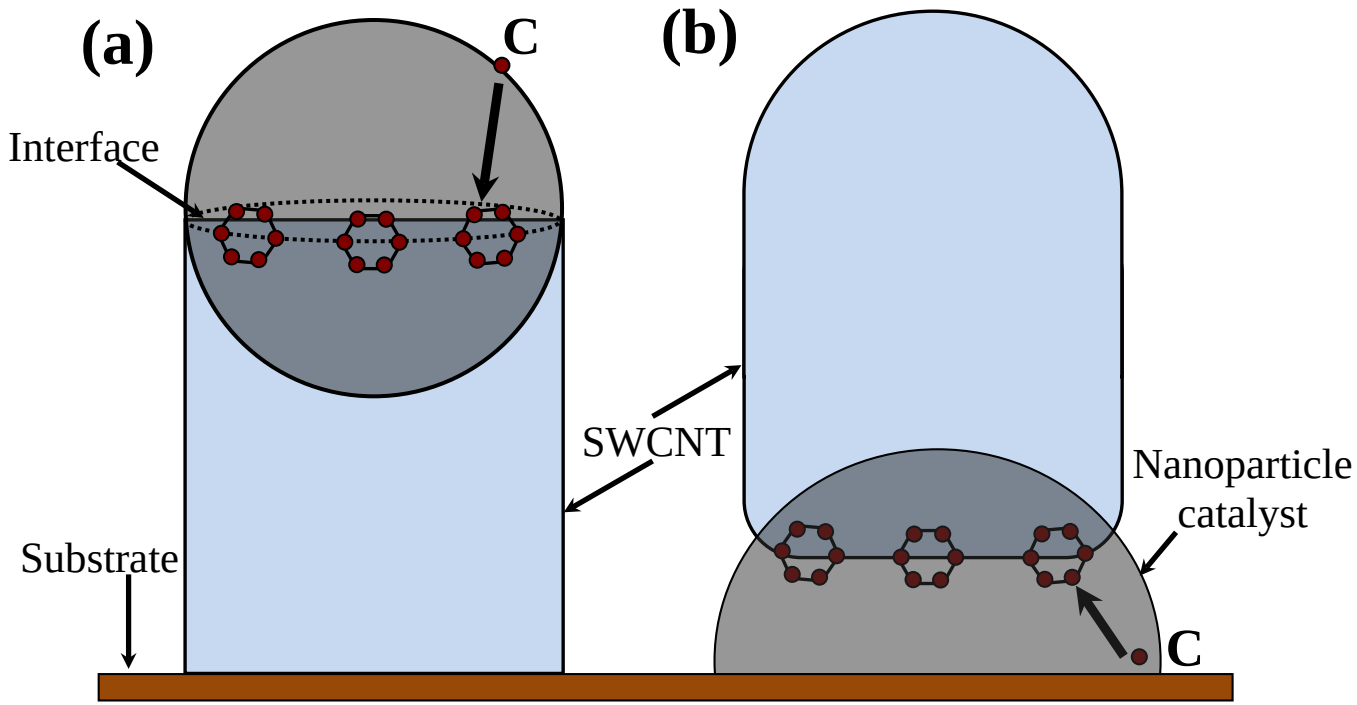

Figure 2.4: Schematic diagrams for (a) the tip-based growth and (b) the root based growth of SWCNTs on metal catalyst nanoparticle.

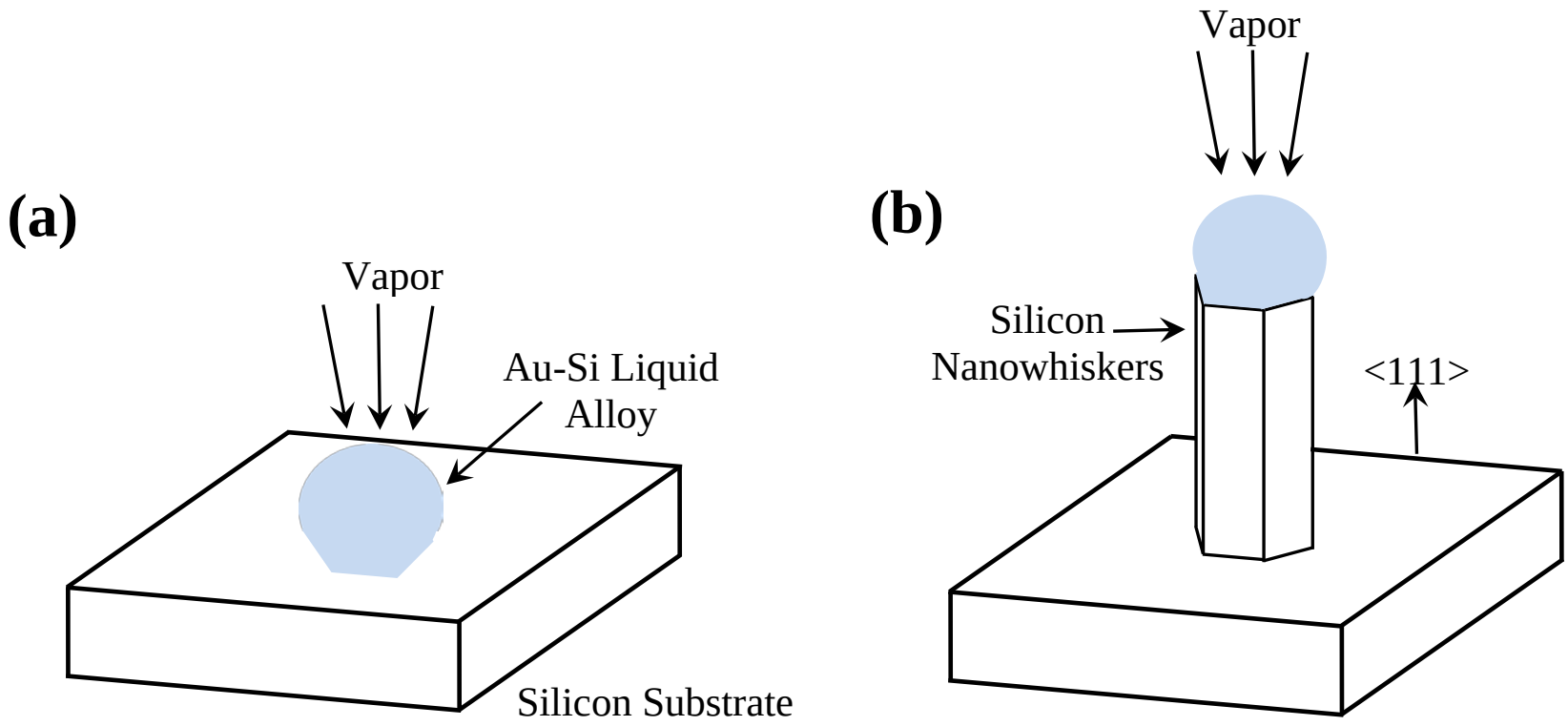

Figure 2.5: Schematic diagram for the Vapor-Liquid-Solid (VLS) growth mechanism of Silicon whiskers on Au nanoparticle. (*Adapted from Wagner et al.*[15])

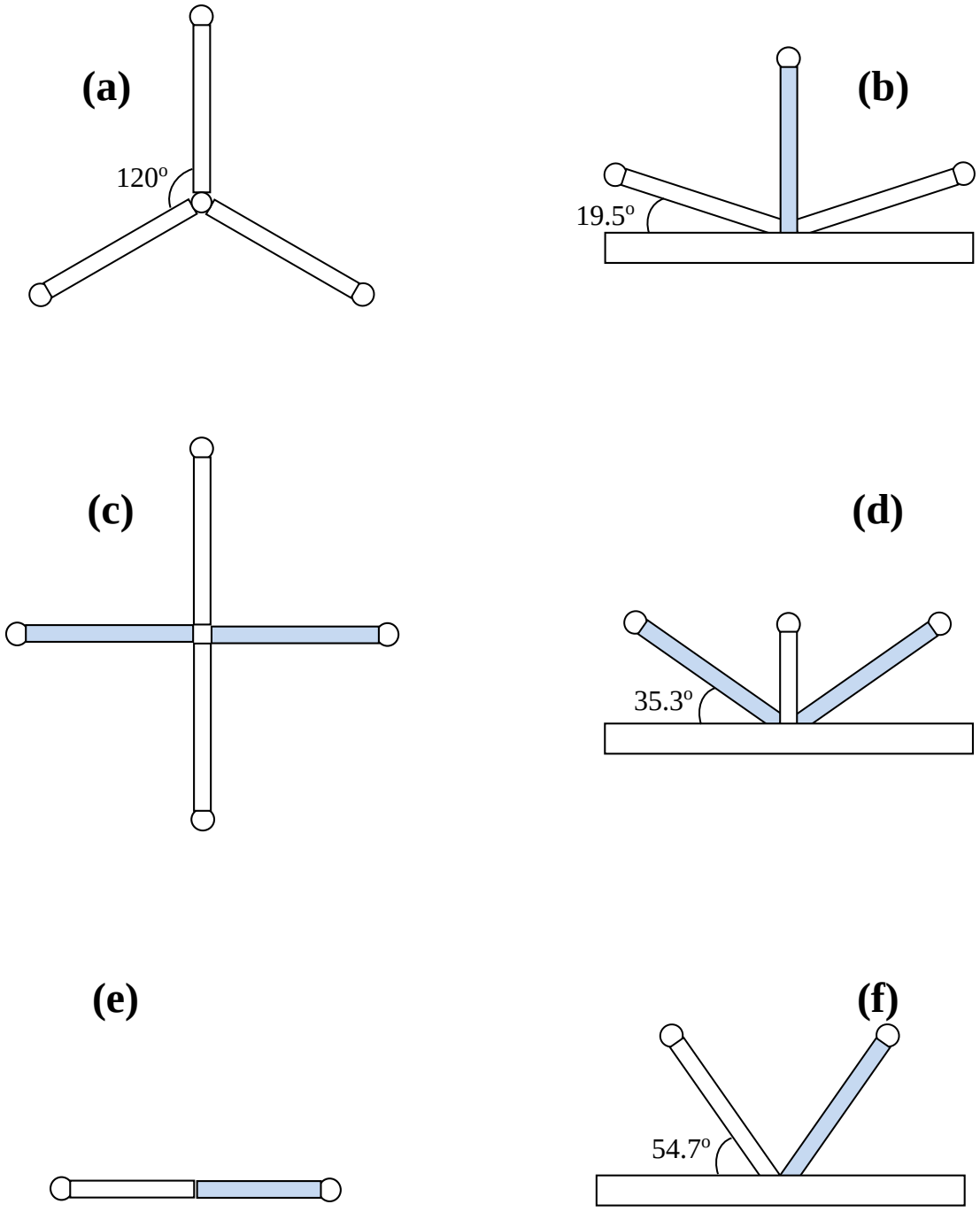

Figure 2.6: Schematic illustrations of the <111> nanowires grown epitaxially on various different substrate orientations. (a,c,e) top views and (b,d,f) side views. (a,b) (111)B substrate. (c,d) (001) substrate and (e,f) (110) substrate. The<111>B nanowire orientation has been highlighted in blue. (*Adapted from Fortuna et al.*[84])

Table 2.1: Typical nanowire growth orientations and areal cross-sections (if known) of several important nanowire materials. (*Adapted from Fortuna et al.*[84])

Material	Growth directions	Nanowire cross-sectionalgeometry (if known)	Notes	References
Si	<111>		>20nm diameter	15,85,86
	<110>		< 20 nm diameter	57,85-87
	<112>	Square	< 20 nm diameter	87,88
	<100>			57,89
Ge	<111>	Hexagon		90
	<110>	Hexagon		90
	<112>	Square		90
GaAs	<111>B/[0001]	Hexagon	Often polytypic (ZB/WZ) with stacking faults	74
	<110>	Trapezium	No stacking faults, lateral growth on (001) GaAs surface	91-93
	<110>			94
	<112>			95
	<100>		Si (111) substrate, no stacking faults	96
	<111>A	Triangle	No stacking faults	97
InP	<111>B/[0001]	Hexagon	Often polytypic (ZB/WZ) with stacking faults	50
	<110>			98
	<100>	Square	No stacking faults	99
InAs	<111>B/[0001]	Hexagon	Often polytypic (ZB/WZ) with stacking faults	74
	<100>			100
	<110>		Lateral growth on the InAs (001) surface	100
	<112>		Lateral growth on the GaAs (111)B surface	101
ZnO	[0001]	Hexagon		68,102,103
	<10-10> m-axis		Aligned lateral growth on the a-plane sapphire	104
GaN	[0001] c-axis	Hexagon	Polar direction	78,105,106
	<10-10> m-axis	Triangle	Nonpolar direction	78,102,107
	<11-20> a-axis	Triangle	Nonpolar direction	106-108

Table 2.2: The geometrical relationship between possible growth directions of <111> oriented nanowires grown on various elemental semiconductor substrate orientations. (*Adapted from Fortuna et al.*[84])

Substrate	Number of <111> growth directions	Angle with respect to the substrate surface	Azimuth between nanowires
(001)	4	35.3°	90°
(110)	2	54.7°	180°
(111)	4	3 directions – 19.5°	120°
		1 direction – 90°	n/a

Table 2.3: The geometrical relationship between possible growth directions of <111>B oriented nanowires grown on various compound semiconductor substrate orientations. (*Adapted from Fortuna et al.*[84])

Substrate	Number of <111>B growth directions	Angle with respect to the substrate surface	Azimuth between nanowires
(001)	2	35.3°	180°
(110)	1	54.7°	n/a
(111)A	3	19.5°	120°
(111)B	1	90°	n/a

CHAPTER 3: THEORETICAL METHODS

3.1 Introduction

In this chapter, we discuss the underlying fundamental aspects of the theoretical methods that we have extensively used in all our calculations. The theoretical method involves carrying out electronic structure calculations using density functional theory (DFT) in order to understand the epitaxial nucleation and growth of one-dimensional nanomaterials on bimetallic nanoparticle surfaces.

3.2 Electronic Structure Calculations

Matter is made up of atomic nuclei and electrons, and the complex interactions of these atomic particles are responsible for all the intrinsic characteristic properties of materials. In order to understand the properties of materials and to design new materials and predict their properties, a thorough understanding of these complex interactions between atomic particles is required. Quantum mechanics provides a theoretical framework to study these materials by explaining the electronic structure of the material. It was already known a century ago that solving the many particle Schrödinger equation can in principle yield all the material properties. Many qualitative features of material properties was obtained from independent electron approximations.[109,110] However, quantitative predictions need a more sophisticated treatment. In the 1960's the formal theory of actually calculating the material properties were laid down in the form of *ab-initio* density functional theory (DFT). With the help of DFT and the vast improvements in computers, only now is it possible to perform numerical calculations similar to those described in this

dissertation. In the following sections, we lay out the underlying formalism and a brief description of some of the techniques used in actual DFT calculations.

One can write the many-body Schrödinger equation for a given system in terms of its Hamiltonian as,

$$\{H_{nn} + H_{ne} + H_{ee}\}\Psi_{tot} = E\Psi_{tot} \quad (3.1)$$

where, H_{nn}, H_{ee} and H_{ne} are the Hamiltonian for the nuclei-nuclei, electron-electron and nuclei-electron respectively and, ψ_{tot} is the wave-function of the total system comprising of nuclei and associated electrons and E is the corresponding total energy of the system.

The many-body Schrödinger equation relates the Hamiltonian of the system to the total energy of the system of interacting ions and electrons and in principle, all the properties associated with a particular material can be derived from its solution. However, the apparent simplicity of the equation belies the actual complexity involved in solving the problem. It is generally impossible to find the true solution for the many-body total wave-function ψ_{tot}, even for very small systems involving a few ions and electrons. Hence, to obtain the solution involving a large number of ions and electrons, it is often necessary to introduce suitable approximations and reformulations of the above equation. In the following subsections, we detail the following points.

1. The Born-Oppenheimer approximation for separating the nuclear degrees of freedom, H_{nn} from the electronic degrees of freedom.

2. The density functional theory for handling the ground-state electronic interactions in H_{ee}.

3. The plane-wave pseudo potential framework for the efficient calculation of interactions between nucleus and electrons in H_{ne} using plane-wave basis sets.

3.2.1 The Born-Oppenheimer Approximation

The mass of an electron is much smaller than that of the nucleus. Hence, the velocity of the electron is significantly faster than that of the nucleus giving rise to different time scales. Thus the nuclear degrees of freedom can be separated from the electronic degrees of freedom thereby decoupling the H_{nn} term in the above equation from H_{ee} and H_{ne}. The Born-Oppenheimer approximation makes use of this fact, stating that electrons adjust instantaneously to a given configuration of the ion, i.e., the electrons are always in their ground-state for a set of nuclear positions.

3.2.2 Density Functional Theory

Density functional theory (DFT) is required to deal with the complex electronic interactions in the many-body Schrödinger equation. The fundamental idea of density functional theory is that any property of a system of non-interacting particles can be viewed as a functional of the ground state electronic density $n_0(r)$, that is, only a knowledge of $n_0(r)$ determines all the information in the many-body wave-functions for the ground state. Using DFT, we can find out the total energy, electronic eigenvalues and the forces on the atoms. From the total energy of the system one can further inspect various properties of the system, e.g. cohesive energy, lattice constant and adsorption energies. In addition, DFT can capture all the subtle electronic interactions that are ignored in classical potentials. This feature is particularly important for studying properties of materials in the presence of defects such as those found in actual laboratory samples.

3.2.2.1 The Hohenberg-Kohn (H-K) Theorems

In 1964, Hohenberg and Kohn[111] developed a variational principle approach to determine the ground-state energy of the many-body system, where the ground-state electronic density $n_0(r)$

is used as the fundamental variable. The first H-K theorem established a unique one-to-one correspondence between the ground-state density $n_0(r)$ and the external potential $V_{ext}(r)$. The quantity $V_{ext}(r)$ is the external potential that arises due to the action of the nuclei on the electrons. Thus, the external potential can be uniquely obtained from the ground-state density to within an additive constant. The second H-K theorem proceeds by establishing a variational approach for the electronic energy functional and defining a universal functional $F_{HK}[n]$ of the electronic density n(r). The variational character of E_{HK} means that the ground state electronic density $n_0(r)$ of the system corresponds to the ground state value of the electronic total energy functional. The H-K theorems reduce the 3N dimensional minimization problem of finding the wave-functions to a 3 dimensional problem of determining the ground state electronic density. However, they give no method of computing $F_{HK}[n]$ and hence, no practical way for finding the ground state density of the system. A method of computing $F_{HK}[n]$ was proposed by Kohn and Sham[112] in 1965 and since then DFT has evolved into a powerful computational tool in present day materials science.

3.2.2.2 The Kohn-Sham (K-S) Method

Kohn and Sham[112] derived a method for mapping the complex physical system of interacting electrons onto a much simpler fictitious system of non-interacting electrons that gives rise to the same ground state electronic density $n_0(r)$ and therefore, possesses the same ground-state physical properties. The Kohn-Sham method imagines a system of N non-interacting electrons that gives rise to N independent single-particle Schrödinger equations each acting under the effect of a fictitious Kohn-Sham potential, V_{KS}. The solution to this scheme of K-S equations is to solve the set of equations self-consistently. For a given atomic configuration, we use methods like steepest descent or conjugate gradients to solve the electronic degrees of freedom iteratively and then move the atoms towards their minimum energy configuration based

on the calculated forces acting upon them. Thus, we minimize the energy and obtain a self-consistent solution to the K-S equations.

3.2.2.3 Exchange and Correlation

The total energy of the system as given in the DFT formulation is an exact representation of the ground state electronic density within the Born-Oppenheimer approximation. However, an explicit representation of the exchange correlation, E_{XC} is unknown and this is where the exact nature of the density functional theory breaks down. The exchange-correlation functional is made up of two quantum-mechanical quantities, the exchange energy and the correlation energy. The exchange energy arises due to the spin-spin interactions of electrons as a result of the Pauli's exclusion principle and physically this amount to change in the quantum-mechanical energy due to the wave-function overlap. The correlation energy describes how the probability of finding an electron at a particular position is related to the positions of other electrons in the system.

3.2.3 The Plane-Wave Pseudopotential Framework

For a practical implementation of DFT in computations, we need to express the abstract mathematical concept of the electronic wave-function$\psi_0(r)$ and the Kohn-Sham orbital wave-function ψ_j in terms of basis sets to represent the problem. For isolated systems, like atoms and molecules, descriptions based on Gaussian and atomic orbitals basis sets work quite well. However, for extended systems, it is often convenient to express the wave-function in terms of mutually orthogonal plane wave basis sets. In principle, to describe an extended system an infinite number of plane waves are required. However, this problem is circumvented by taking advantage of the periodicity of the lattice. The extended system is represented as a repeated array of super-cells, with periodic boundary conditions imposed on the periodic edges.

3.2.3.1 The Pseudopotential Approximation

Though the plane waves are quite useful, they suffer from a major drawback. An unacceptably large number of plane waves are required to depict the electronic wave-function in the vicinity of the nucleus accurately. A solution to this problem can be found out by using the pseudopotential approximation, which replaces the actual nuclear potential in the electron-ion interactions with a much weaker counterpart but the retaining the chemical behavior of the full potential. This is done by redefining the term "ion" so as to include not only the atomic nuclei but also the core electrons and the term "electron" becomes valence electrons. The logic behind doing so is that the core electrons have a screening effect on the nucleus and results in a much weaker potential. The core region is defined by a cut-off radius r_c, which is chosen such that all the nodes of the all-electron valence wave-function are contained within r_c (i.e. inside the core region). Outside the core region the pseudo wave-function matches exactly the all electron wave function. There are various kinds of pseudo-potentials viz. (i) Norm-conserving, (ii) Ultrasoft Pseudopotentials, etc. where the norm of the pseudo wave-function is equal to the norm of the all electron wave-function within the core region are said to be norm-conserving. These are more accurate and have good transferability properties, i.e., the pseudopotential for an atom/element is independent of its environment; the same pseudopotential should work if the atom is placed in the bulk, on a surface, or in a compound with some other elements. However, they require a fairly high value of E_{cut} making them computationally expensive.

3.2.3.2 Projector-Augmented-Wave Method

The projector augmented wave (PAW) method is a generalization of the pseudopotential and linear augmented wave methods. This method was introduced to significantly enhance the computational efficiency of the density functional theory calculations. Valence wave-functions

tend to have rapid oscillations near the ion cores due to the requirement of orthogonality to the core states and hence, a large number of Fourier components are required to represent the valence wave-function. The introduction of the PAW potentials transforms these rapidly oscillating wave-functions into a smooth wave-function thereby making the overall DFT calculation extremely computationally efficient. In general, the PAW method gives reliable results for materials with strong magnetic moments or large differences in electronegativity.

3.3 Vienna *Ab-initio* Simulation Package (VASP)

Vienna ab initio Simulation package (VASP) is a computer simulation package used for atomistic modeling of materials based on *ab-initio* electronic structure theory and quantum mechanical molecular dynamics. The code was developed by the computational physics group led by Jürgen Hafner and in association with George Kresse and Jürgen Furthmüller at Universität Wien, Sensengasse, Austria. The VASP code is written in the Fortran 90 program and is useful for calculating the properties of systems with periodic boundary conditions. Plane wave basis sets are used to probe the entire unit cell and the ion-electron interaction is described by the ultrasoft pseudopotentials (US-PP) or projector-augmented wave (PAW) method. The energy optimized geometric configuration of the atomic system is obtained iteratively by first assigning an electronic charge density to calculate the Hamiltonian and then subsequently solving the Hamiltonian to obtain the new set of wave-functions. The new set of wave-functions is used to evaluate the new charge density matrix and after suitable mixing with the old charge density, the iteration is repeated. The ground state energies are optimized until the net forces acting on each atom are converged to a pre-set tolerance limit. For accurate results, the geometry optimized ground state energy needs to be adequately converged to the cut-off energies and k-point sampling.

CHAPTER 4: EPITAXIAL NUCLEATION MODEL FOR CHIRAL-SELECTIVE GROWTH OF SINGLE-WALLED CARBON NANOTUBES ON BIMETALLIC CATALYST SURFACES

4.1 Introduction

In the last two decades, single-walled carbon nanotubes (SWCNTs) have attracted significant interest for technological applications because of their unique structure-dependent physical and chemical properties, including the ability to exhibit either metallic or semiconducting behavior. The atomic-scale structure of SWCNTs is defined by their chirality, which can be visualized as the diameter and angle at which a graphene sheet is rolled. The different possible structures of SWCNTs have been indexed by a set of (n,m) chiral indices, where n and m are integers. While numerous strategies have been developed to study and grow SWCNTs, a critical challenge that remains for applications is the synthesis of *specific* (n,m) chiralities.

SWCNTs are normally grown by exposing a catalytic metal nanoparticle less than 5 nm in size to a hydrocarbon gas at high temperature. It is generally believed that the catalyst particles are first supersaturated with carbon by dissolution of carbon atoms on the particle surface and carbon diffusion on the surface or in the bulk of the particle, followed by carbon segregation and, finally, emergence of an open fullerene that grows into a nanotube.[113] Subtle changes in the properties of the catalyst such as composition[8,47,114-116] and shape[29], have been

This chapter was published in *Carbon*, 2012, 50, 3766-3773, [Ref 132]. Copyright permission is included in Appendix A.

empirically observed to induce dramatic changes in the as-grown SWCNT structures. However, a clear relationship behind SWCNT chirality and the catalyst remains poorly understood, making it difficult to perform *a priori* catalyst design for the selective growth of specific (n,m) SWCNTs.

Recent theoretical efforts have provided significant insight into the catalytic growth process and hinted at a strong correlation between the SWCNT chirality and the structure of the catalyst. Several articles by Balbuena and co-workers[117,118] have explored the various steps involved in the growth mechanism of SWCNT on Ni and Co nanoclusters: the competition between the nanotube-nucleation and carbon-catalyst adhesion, the mechanism for the carbon addition process and the relation between the catalyst size and metal-carbon interactions. Using reactive molecular dynamics/force-biased Monte Carlo simulations, Neyts and co-workers[25,45,119] have demonstrated a step-by-step atomistic description of the metal-catalyzed nucleation process and the subsequent growth of the SWCNT. Their simulations show that the nanotube changes chirality during the growth process resulting in a nanotube with a definable chirality. Other computations have shown that the nucleation of the cap on the catalyst is the rate-determining step in nanotube growth.[120] Using a tight-binding model coupled with grand canonical Monte Carlo (GCMC) simulations, Amara *et al.*[22] demonstrated that the primary role of the catalyst is to confine carbon atoms on or close to the surface so that a critical concentration is reached beyond which carbon atoms start forming chains that eventually form a cap. Once the cap nucleates, the catalyst prevents the growing cap structure from closing into a fullerene cage and keeps the carbon "edge" alive for the addition of new carbon material.[26] Ding *et al.*[13] showed via density functional theory (DFT) that commonly used metals for nanotube growth such as Fe, Ni, and Co are characterized by strong metal-carbon adhesion (compared to other metals such as Cu and Pt)

which facilitates cap nucleation. Building on these ideas, Reich *et al.*[2,32] proposed that the critical function of the catalyst during nanotube nucleation is binding and stabilization of the cap and that lattice matching of the cap and the catalyst, in terms of their respective atomic-scale structures, determines which tube chirality grows. Along the same lines, Börjesson *et al.*[35] argued that when there is a lattice mismatch, there is significant restructuring of the metal to fit the SWCNT cap and not *vice-versa*. However, none of these previous studies has attempted to calculate the stability of caps on bimetallic catalyst surfaces.

Here, we use DFT calculations to model cap nucleation on bimetallic catalyst surfaces and find that an epitaxial relationship between the bimetallic catalyst and the cap structure supports the preferential growth of specific nanotube chiralites. To perform our study, we used a simplified two-dimensional (2D) (111) surface which is considered to be the most common and important edge on a metal catalyst nanoparticle for nanotube nucleation because of its close overlap with the graphite lattice.[116,121] Based on our experimental characterization of the bimetallic nanoparticles, we varied the atomic spacing on our 2D model surface and systematically performed a series of calculations. We tried a surface consisting of only Ni atoms, both Ni and Fe atoms in different ratios, and multi-layered surfaces (2 layers). We studied the energetics of 6 representative nanotube chiralities (as caps)including (8,4), (6,5), (9,4), (8,6), (10,3), and (7,5) which are predominantly detected in our experiments. In all cases, our calculations show that chiralities such as (8,4) and (6,5) are more stable on surfaces corresponding to $Ni_{0.27}Fe_{0.73}$ catalysts, while chiralities such as (9,4) and (8,6) are more stable on surfaces corresponding to Ni catalysts, in excellent agreement with experiments. In addition to explaining our experimental results, these findings suggest that a potential route to (n,m)

selectivity is to design bimetallic catalysts with lattice matching criterion as a guide for the desired tube chirality.

4.2 Experimental Background

We begin with a brief discussion of our experimental results which inspired the theoretical efforts. In Figure 4.1, the relative abundances of various semiconducting chiralities grown with Ni, $Ni_{0.67}Fe_{0.23}$, $Ni_{0.5}Fe_{0.5}$, and $Ni_{0.27}Fe_{0.73}$ bimetallic catalyst nanoparticles of the same size are shown. Details of the experimental approach and the experimental results have been reported elsewhere.[122-125] The relative abundances were obtained from photoluminescence (PL) spectroscopy. We first collected spectra at various excitation and emission wavelengths to determine the PL emission of the various semiconducting tube chiralities. We then corrected the PL emission by a recently reported model[126] for quantum efficiency and absorption extinction coefficients for different chiralties and finally estimated the fractions of the different chiralities from the partial derivative of the PL emission peak intensity.[16] From this semi-quantitative analysis, we found that Ni and $Ni_{0.67}Fe_{0.33}$ bimetallic catalysts produce a relatively broad chirality distribution composed of (in order from smallest to largest diameter) (6,5), (8,3), (7,5), (8,4), (10,2), (7,6), (9,4) and (10,3), (8,6), (9,5), and (8,7) tubes, while $Ni_{0.5}Fe_{0.5}$ and $Ni_{0.27}Fe_{0.73}$ bimetallic catalysts yield a much narrower chirality distribution (in comparison) with mostly (6,5), (8,3), (7,5), (8,4), and (7,6) tubes. The overall trend of smaller diameter tubes for Fe-rich catalysts has been previously observed.[47] Based on our previous experiments which showed that changing the catalyst size did not affect the chirality distribution, we believe that the chirality distributions are mainly influenced by the catalyst composition. In Figure 4.2, X-ray diffraction (XRD) spectra of our nanoparticle catalysts are shown. We find that Ni catalysts exhibit face-centered cubic (fcc) structure, in agreement with the crystal structure of bulk Ni. When Fe is

added to the catalyst, the fcc diffraction peaks shift to lower 2Θ values, indicating an expansion of the lattice. At high Fe content, additional peaks appear in the spectrum corresponding to the body-centered cubic structure of Fe. Overall, these results suggest that compositional changes to the bimetallic catalysts lead to perturbations to the crystal structure, which then cause the chirality distributions of as-grown nanotubes to shift.

4.3 Computational Methods and Models

To understand the epitaxial relationship between bimetallic catalyst composition and the nanotube chirality, we applied lattice matching criterion and performed DFT calculations of nanotube cap nucleation. The total energy DFT calculations were done using the Vienna *ab-initio* simulation package (VASP).[127] The electron exchange-correlation energy was calculated using the generalized gradient approximation (GGA) as parameterized in the Perdew–Wang functional (PW91).[128] The nickel, iron, and carbon core electrons were treated using ultrasoft pseudopotentials, and the cutoff energy of the plane-wave basis set for expanding valence electrons was 400 eV. Supercell sizes were sufficiently large to allow for single Γ-point k-space sampling. All calculations were spin-polarized. Total energies were converged to 5 meV. The nanotube cap for a specific chirality is arbitrarily chosen for our calculations from the ones that follow the isolated pentagon rule – the exact nanotube cap is not critical to assessing metal-cap interactions and once the cap is stabilized, all the dangling bonds are saturated.

We used the (111) lattice plane of face-centered cubic (fcc) Ni as our 2D model of a bimetallic catalyst surface, with *d*, the distance between neighboring atoms in the plane, as a variable parameter (Figure 4.3(a)). While we realize that, in reality, catalyst nanoparticles are complicated surfaces that consist of a random distribution of crystal planes, facets, and steps, this simplified model surface captures the most likely exposed, catalytically-active surface on a Ni

nanoparticle. The Ni(111) surface is believed to be the nucleation site for nanotubes because of its close lattice match with graphite, and it is one of the lower energy surfaces on a Ni catalyst particle. To study the role of different metals in the stabilization of the nanotube caps, we also performed calculations with catalyst surfaces containing both Ni and Fe atoms (Figure 4.3(b)). The Ni and Fe atoms were distributed randomly on the catalyst surface in the same relative proportion as those used in experiments (e.g. $Ni_{0.67}Fe_{0.33}$, $Ni_{0.5}Fe_{0.5}$, $Ni_{0.23}Fe_{0.67}$).

To calculate the overall energy associated with cap nucleation, E_b, the isolated (and re-optimized) fullerene cap and Ni structures were used as the references, i.e.,

$$E_b = E_{cap+catalyst} - E_{cap} - E_{catalyst} \quad (4.1)$$

where $E_{cap+catalyst}$ is the energy of the (relaxed) cap bound to the catalyst, E_{cap} is the energy of the isolated cap, and $E_{catalyst}$ is the energy of the isolated catalyst surface. A negative E_b indicates that the cap-catalyst system is more stable than the separated cap and catalyst. The structure of the cap is governed by the Euler criterion, which says that the atoms in the cap should be connected in such a way that there are only six pentagons and rest of them are hexagons.[6,129] Previous reports have shown that cap structures with isolated pentagons are more stable than those with adjacent ones, which is known as the isolated pentagon rule (IPR).[7] For the chiralities considered in this work, numerous possible cap structures exist with a given chirality that follow the IPR, except for (6,5) which has only one cap that obeys the IPR.

4.4 Results and Discussions

Calculations were systematically performed by varying the bond length in the 2D catalyst surface, *d*, from 2.47to 2.57Å in intervals of 0.02 Å, and attempting to minimize the overall energy, E_b, in each case. The bond length, *d*, represents the compositional and structural changes to the catalyst surface induced by alloying Ni with Fe. The variations in the lattice spacing (and

neighboring atom distance in the (111) plane) are consistent with our experimental measurements; for example d~2.49 Å for Ni and d~2.53 Å for $Ni_{0.27}Fe_{0.73}$ catalysts (see Table 4.1). Initially, we modeled the catalyst surface with only Ni atoms present and the effect of a second metal was not considered, *i.e.* only *structural* changes to the Ni(111) surface were considered. Later, we included Fe atoms in the modeled bimetallic catalyst surface to compare and clarify the role of two metals on epitaxial nucleation.

Calculations were limited to the following cap chiralities: (8,4), (6,5), (9,4), (8,6) (7,5) and (10,3). In each of these cases, we placed all the C atoms in the cap at least 1Å above the model surface. In Figure 4.4, results for the calculated binding energies, E_b, of (8,4), (6,5), (9,4), and (8,6) caps on the model Ni(111) surface are shown as a function of bond length d. For the (8,4) cap, a minimum energy configuration is obtained when d is equal to 2.53 Å which is equivalent to the bond length of a (111) surface corresponding to $Ni_{0.27}Fe_{0.73}$ (see Table 4.1), while the (9,4) and (8,6) nanotube caps have minimum energy configuration at d=2.49 Å, which is close to the bond length of the initial Ni(111) surface. In the case of the (6,5) cap, E_b continues to decrease up to d=2.57 Å which is the maximum value used in the calculations, but we can infer that this cap is more stable at higher bond lengths. For the (7,5) and (10,3) caps, we failed to obtain binding energies because the calculations did not yield a stable cap on the catalyst surface, i.e. the caps were completely distorted after relaxation (see Figure 4.8).

We further analyzed the nucleation of the various caps on our model catalyst surfaces. In the initial configuration, some of the "edge" carbon atoms had dangling bonds and were unsaturated (not bonded). After energy minimization, we found that the nanotube cap changed shape and became elongated, as shown in Figure 4.5(a) for the (8,4) cap. At this point, the dangling bonds were saturated by forming C-Ni bonds (refer to Figure 4.5(b)). This

phenomenon was common to all 4 nanotube chiralities studied and indicate that our calculations reflect stable cap formation (*i.e.,* no dangling bonds). Our calculations for the (8,4) cap showed the best agreement with experiments. The lowest energy for cap nucleation (E_b) occurs at the exact same bond length (2.53 Å) as experimentally determined by XRD for $Ni_{0.27}Fe_{0.73}$bimetallic catalysts (see Table 4.1) which were found to preferentially grow (8,4) tubes. In the case of the (6,5) cap, the lowest energy was not determined and we speculate that catalysts with bond lengths close to or perhaps greater than 2.57 Å in the (111) lattice plane may be optimal for (6,5) tubes. Indeed, Ghorannevis *et al.*[130] recently reported high yields of (6,5) tubes with Au catalysts which have a cubic closed-packed structure and an average bond length of 2.88 Å. As for the (9,4) and (8,6) nanotube caps, we find the highest cap stability at d=2.49 Å which corresponds to the bond length of atoms in the (111) lattice plane of Ni catalysts (see Table 4.1). This is again consistent with our experimental results which showed a higher abundance of (9,4) and (8,6) tubes on Ni catalysts as compared to any other composition of Ni-Fe bimetallic catalysts.

While the modeling results suggest that the structure of the catalysts is responsible for the predominance of certain chiralities, the role of different metals in binding has been neglected. To address this issue, we performed similar calculations with catalyst surfaces containing both Ni and Fe atoms. The surfaces were modeled as (111) surfaces, as before, with a random configuration of Ni and Fe atoms corresponding to the composition of the catalyst (see Figures. 4.6(a) & 4.6(b)); for example, given a unit cell consisting of 56 total atoms, a $Ni_{0.23}Fe_{0.73}$ and $Ni_{0.67}Fe_{0.33}$ surface were arranged with 15 Ni atoms and 41 Fe atoms and 37 Ni and 19 Fe atoms, respectively. The lattice spacings were varied while keeping the same atomic arrangement to obtain binding energies of nanotube caps on strained bimetallic surfaces. These results could be compared to those obtained for pure Ni surfaces.

Our calculations show that the binding energy of the (8,4) nanotube cap on both the $Ni_{0.27}Fe_{0.73}$ and $Ni_{0.67}Fe_{0.33}$ (111) surface has an energy minimum (maximum binding strength) at a bond length of 2.53 Å between the metal atoms (Figure 4.7(a)). In comparison, the binding strength of the (6,5) nanotube cap on both the $Ni_{0.27}Fe_{0.73}$ and $Ni_{0.67}Fe_{0.33}$ (111) surface is maximum at an average bond length of 2.57 Å (Figure 4.7(b)). These results are entirely consistent with those obtained with the pure Ni(111) surface. However, a noticeable feature is that the absolute binding energies of a particular nanotube cap on the Ni_xFe_{1-x}(111) surfaces are lower than those on the Ni(111) surfaces. This has been previously documented by Ding *et al.*[13] who reported that the binding strengths of the C-Fe bond is lower (i.e. stronger) than that of C-Ni bond and hence, the introduction of Fe atoms in modeling the 2D catalyst surface lowers the absolute binding strength.

Since real catalysts are not single layers of metal atoms, we also attempted to incorporate under-layers in the modeled catalyst surface. We note that modeling the catalyst surface with multiple layers makes the DFT calculations extremely time-consuming and expensive. To simplify the calculation, we calculated the stability of a (8,4) nanotube cap on a bilayer Ni(111) surface with bond lengths of 2.49 and 2.53 Å and compared the results with a single layer. We find that the calculation shows only a negligible difference and, thus, conclude that the second layer does not significantly alter the binding and stabilization of the caps. In our simulations, the Ni and Fe atoms are "frozen" and the influence of the second layer may not be as substantial as if we had allowed for perturbations to the structure of the surface layer.

The notion of nanotube nucleation on a catalyst surface by lattice matching was first proposed by Reich *et al.*[32] In their calculations, the binding energies of chiral and achiral nanotube caps were obtained for a Ni(111) surface and the cap-catalyst binding was separated

into two types of interactions: a *global matching* where the diameter of the achiral caps matches exactly with the metal lattice and a *local matching* where the edge C atom in the cap "rim" lies in the stable sites. Our method of calculating the adsorption energy of the cap-catalyst system accounts for both the global and local matching of the nanotube cap edge with the 2D catalyst surface. A chiral cap like the (8,4) contains both armchair and zigzag edges and these irregular edges forbid a global match, but a local match is still possible. This local matching is responsible for the lower energy of cap formation for the (8,4) cap when the average bond length in the 2D catalyst surface increases from 2.49 to 2.53Å. As noted by Reich *et al.*[2,32], the energy differences among the chiral caps are very small and cannot completely explain the large differences in relative abundances of various chiralities obtained by growing SWCNTs on different bimetallic catalysts. However, for the (8,4) or (6,5) nanotube cap, the energy gain obtained by changing *d* is sufficient to alter the relative stabilities of the cap-catalyst system and suggests that the preferential growth of (8,4) or (6,5) tubes on specific bimetallic catalysts is due to the catalyst structure and its relationship to the nanotube chirality. These trends hold true even when we include both Ni and Fe atoms which reaffirms our argument that the structural relationship is paramount to chiral selectivity.

We observed an interesting correlation between the rim structure of the stabilized nanotube caps and the type of sites present on our model catalyst surfaces. The model catalyst surface can be broadly classified as having three different sites for carbon atom binding: the three-fold hollow site (H), the bridge site (B) and the atop site (A) (refer to Figure 4.3(a)). As demonstrated previously by Reich *et al.*[32] and recently by Gómez-Gualdrón*et al.*[44], the 3-fold hollow sites and the bridge sites are more favored than the atop sites for epitaxial matching of the nanotube cap. Table 4.2 summarizes the types of binding sites for the edge C atoms present in

the different chiralities of nanotube caps stabilized on our model catalyst surfaces. Though in some cases a clear distinction cannot be made between the hollow and bridge sites, our results suggest that epitaxial matching occurs when the edge carbon atoms occupy more hollow (H) and bridge (B) sites than atop (A) sites, in accordance with previous reports. In our case, this observation is shown to hold for different catalyst surfaces. For example, in the case of the (8,4) nanotube cap, we observe that for d=2.53 Å, the rim carbon atoms occupy 5 H, 4 B, and 3 A sites whereas for d=2.49 Å, the rim atoms occupy 4 H, 4 B and 4 A sites. Thus, the change in bond length from d=2.49 Å to 2.53 Å leads to the rim carbon atoms occupying more H sites and less A sites, resulting in increased stability of the (8,4) nanotube cap on d=2.53 Å. Similar trends are observed for the (6,5), (9,4) and (8,6) nanotube caps.

We attempted to extend our calculations to other chiralities like the (10,3) and (7,5) nanotube caps detected in our experiments, but were not able to achieve stable caps. The lack of a stable cap at the end of our simulation indicates an important limitation to our model: certain chiralities may nucleate on the mono-atomic step edges at the end of (111) facets, as shown by Helveg *et al.*[121], or require a catalyst with a different surface composition or other lattice planes [e.g. (200), (110), etc.], which have not been considered by our model catalyst surface. Future refinements in our modeling approach are planned to address these issues.

Finally, we would like to acknowledge that since DFT calculations are performed at zero temperature, this work assumes a thermodynamic view of nanotube nucleation and growth. In reality, kinetic aspects are also important in determining the chirality of nanotubes during nucleation and growth, as shown by Ostrikov *et al.*[131] and very recently, by Rao *et al.*[40] Although the presented model is still able to adequately explain our experimental results, a

complete and accurate picture of the chiral dependence of catalytic growth of SWCNTs will require a combination of both thermodynamic and kinetic effects.

4.5 Summary and Conclusions

We have used DFT calculations in combination with lattice matching criterion to relate the stability of various cap chiralities on model catalyst surfaces that represent bimetallic catalysts of varying compositions. The results of the calculations provide fundamental insight into why the growth of certain nanotube chiralities such as the (8,4) nanotube is preferred on bimetallic catalysts of a particular composition. Future studies will allow us to use lattice matching as a guide to design new catalysts for the growth of desired chiralities, including ones that are not often observed in experiments such as large diameter semiconducting tubes, metallic species, and zigzag structures.

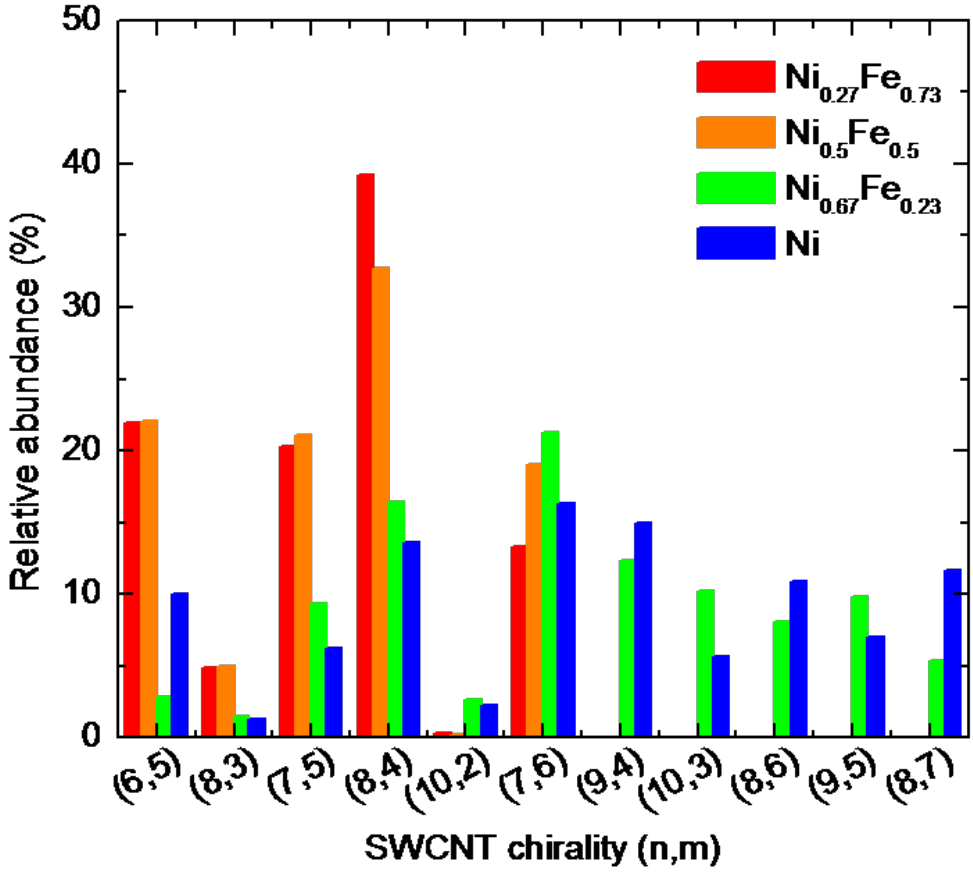

Figure 4.1: Relative abundance of various semiconducting chiralities in SWCNT samples grown with compositionally-tuned Ni_xFe_{1-x}nanocatalysts (mean particle diameter = 2.0 nm). The relative abundances were obtained from photoluminescence (PL) measurements of SDS-dispersed and applying a semi-quantitative analysis.[8,132]

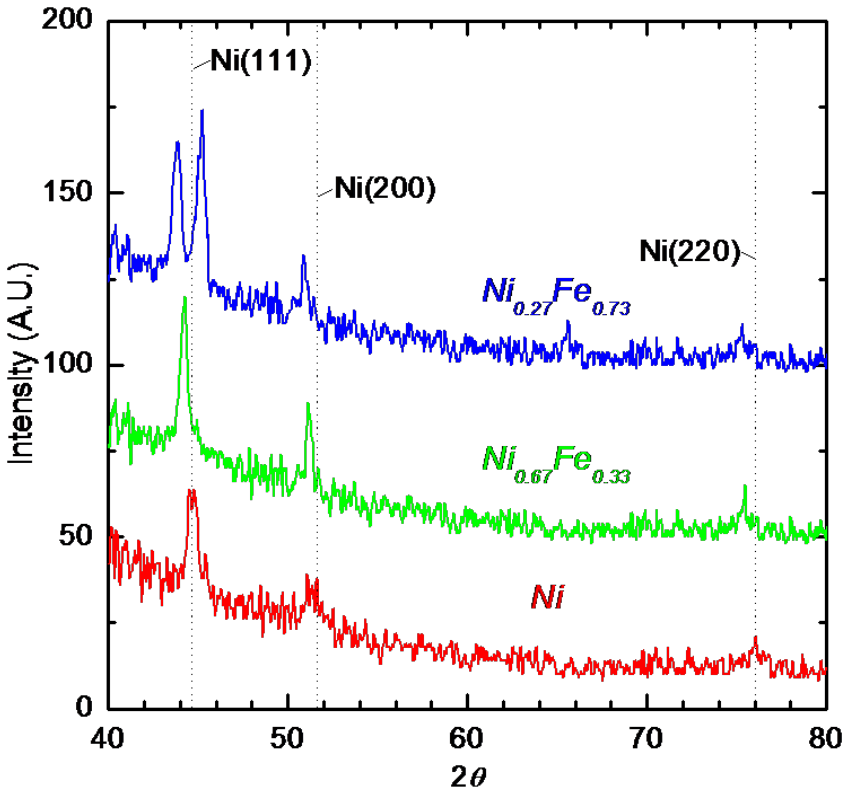

Figure 4.2: XRD spectra of NixFe1-x nanocatalysts (mean particle diameter = 2 nm, x = Ni atomic fraction). The nanocatalysts were prepared by dissociating mixtures of nickelocene and ferrocene in an atmospheric-pressure microplasma.[8,123]

Table 4.1: XRD analysis of Ni_xFe_{1-x}nanocatalysts (x=Ni atom fraction). The lattice constants, a_{fcc}, and bond lengths are calculated from the 2Θ values corresponding to the (111) planes of the face-centered cubic (fcc) diffraction peaks for the respective nanocatalysts.

Catalyst	2Θ (degree)	a_{fcc} (Å)	Bond length (Å)
Ni	44.67	3.51	2.48
$Ni_{0.67}Fe_{0.33}$	44.2	3.56	2.52
$Ni_{0.27}Fe_{0.73}$	43.86	3.58	2.53

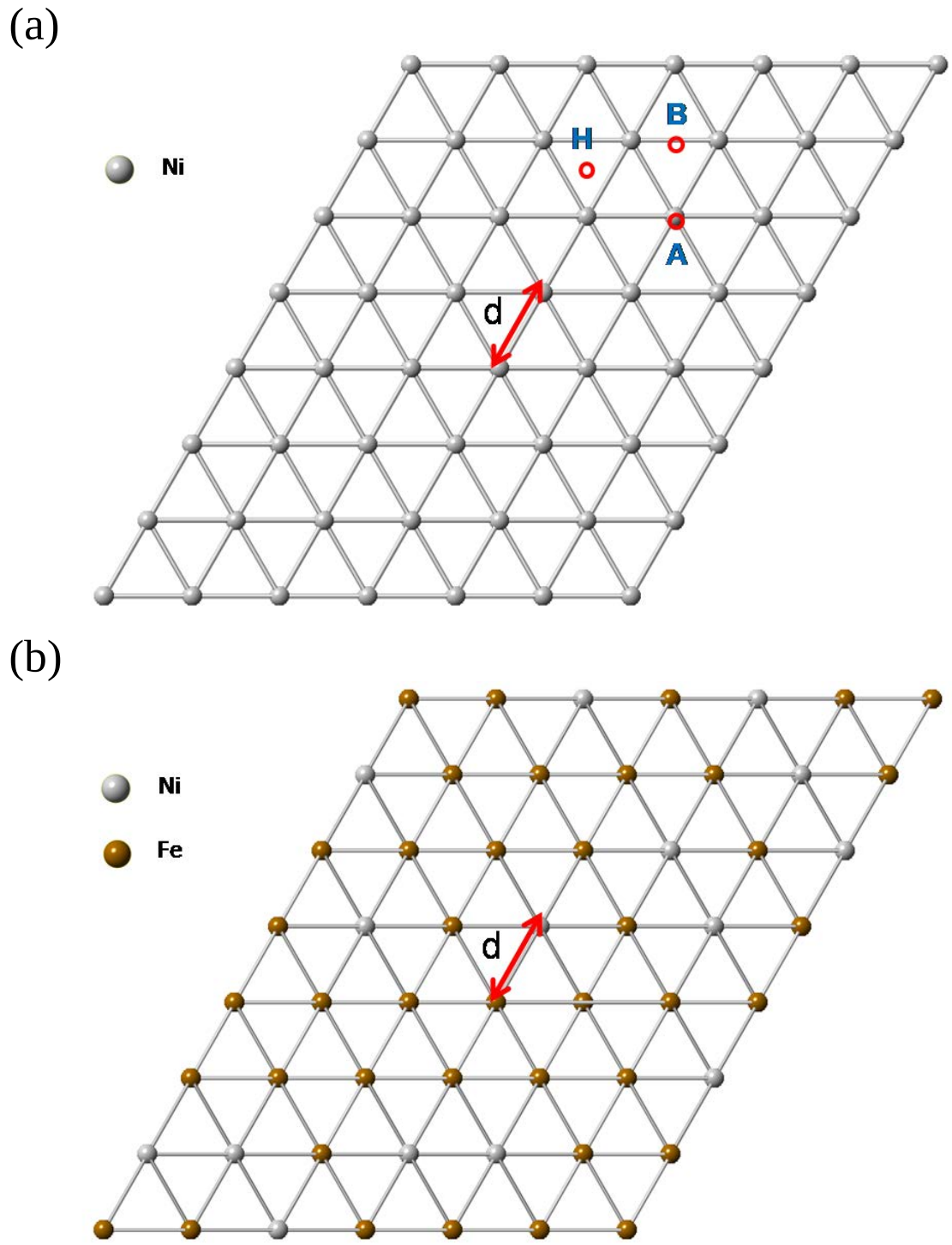

Figure 4.3: Model catalyst surfaces chosen to represent NixFe1-x nanocatalysts for DFT calculations comprised of (a) only Ni atoms and (b) both Ni and Fe atoms, where the bond distance *d* on the (111) surface varies in accordance with the Ni atomic fraction, x. Color code: Ni atoms (gray) and Fe atoms (brown). Various carbon binding sites on the model catalyst surface are shown as: H-hollow site, B-bridge site and A-atop site.

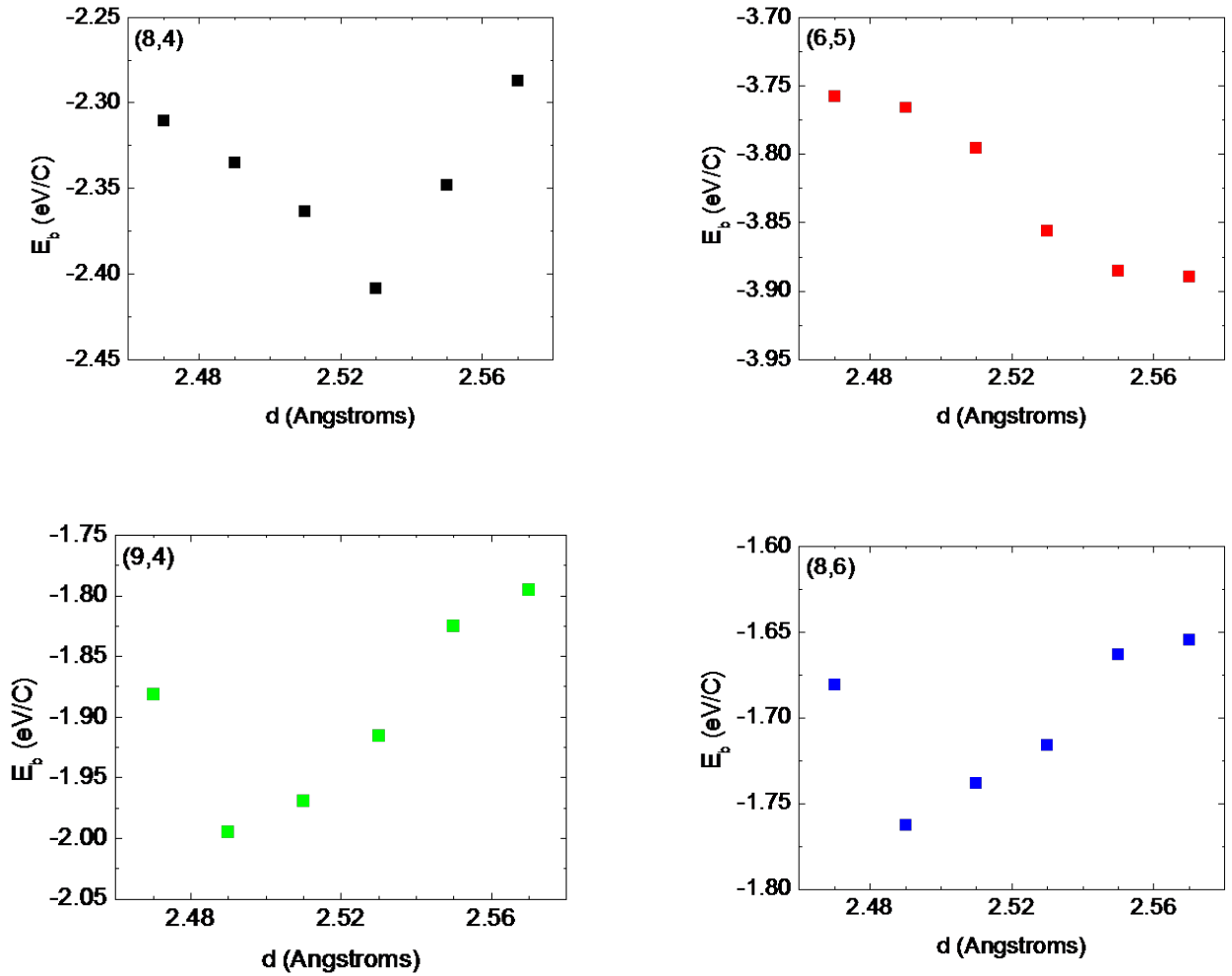

Figure 4.4: Binding energies obtained from DFT calculations for the (8,4), (6,5), (9,4) and (8,6) nanotube caps after geometry optimization on our model Ni catalyst surfaces as a function of bond length, *d*. The Ni-Ni bond length on a pure Ni(111) surface is 2.49 Å.

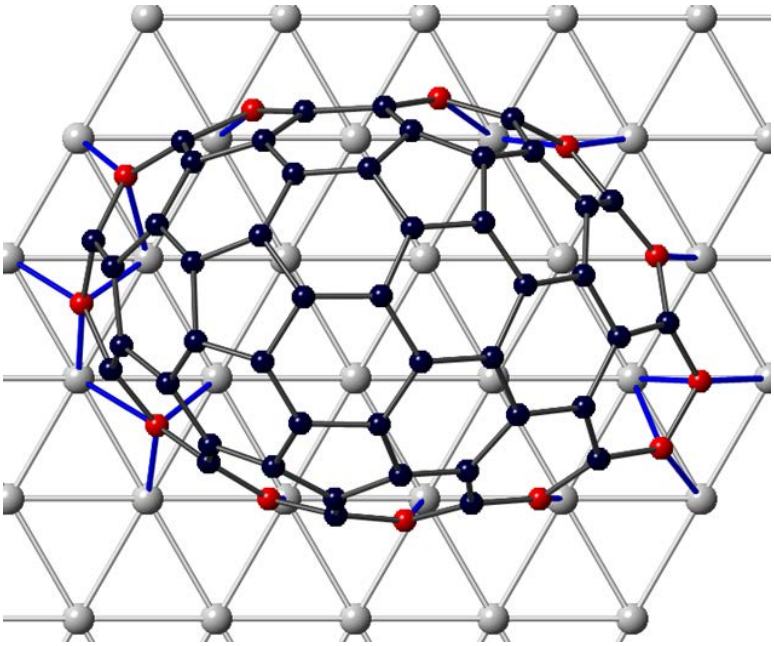

(a)

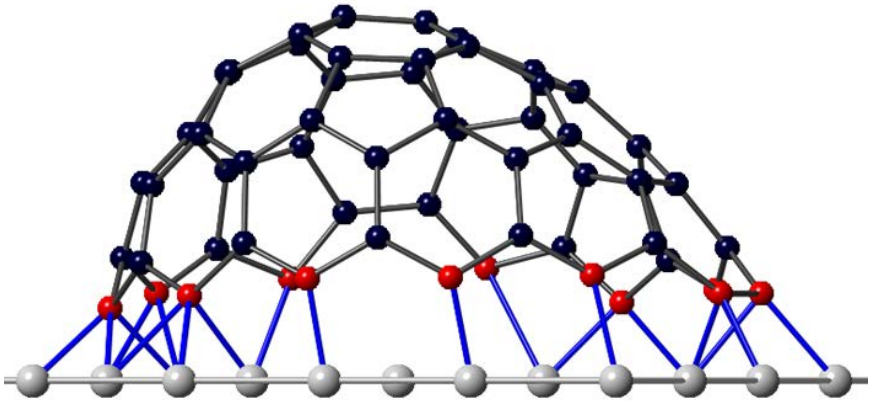

(b)

Figure 4.5: A relaxed (8,4) cap on our model catalyst surface where *d*, the bond distance, is 2.53 Å. (a) Top view and (b) side view. Color code: atoms: C (black), Ni (grey), edge C (red); bonds: C-C (black), C-Ni (blue), Ni-Ni (grey).

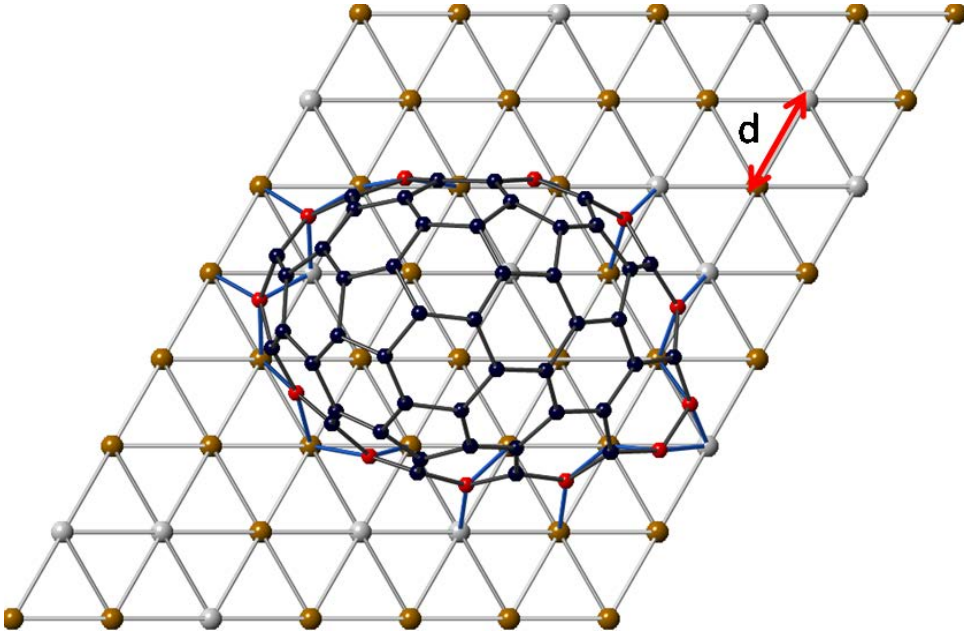

(a)

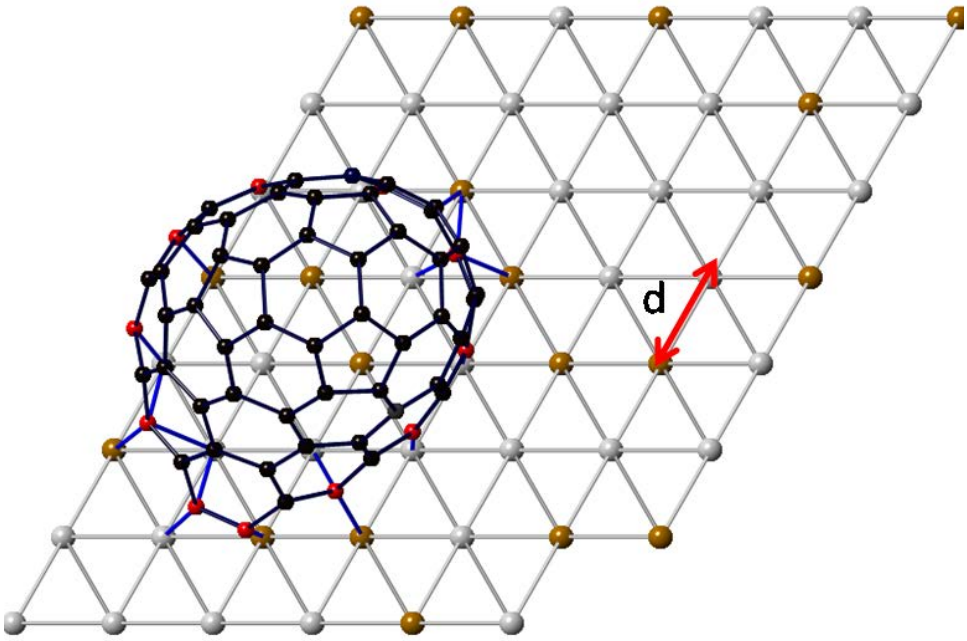

(b)

Figure 4.6: (a) A (8,4) nanotube cap adsorbed on the $Ni_{0.27}Fe_{0.73}$ (111) catalyst surface with *d*=2.53 Å. (b) A (6,5) nanotube cap adsorbed on the $Ni_{0.67}Fe_{0.33}$ (111) catalyst surface with *d*=2.52 Å. Color code: Atoms: C (black), Ni (grey), Fe (brown), edge C (red); Bonds: C-C (black), C-Ni (blue), Ni &Fe (grey).

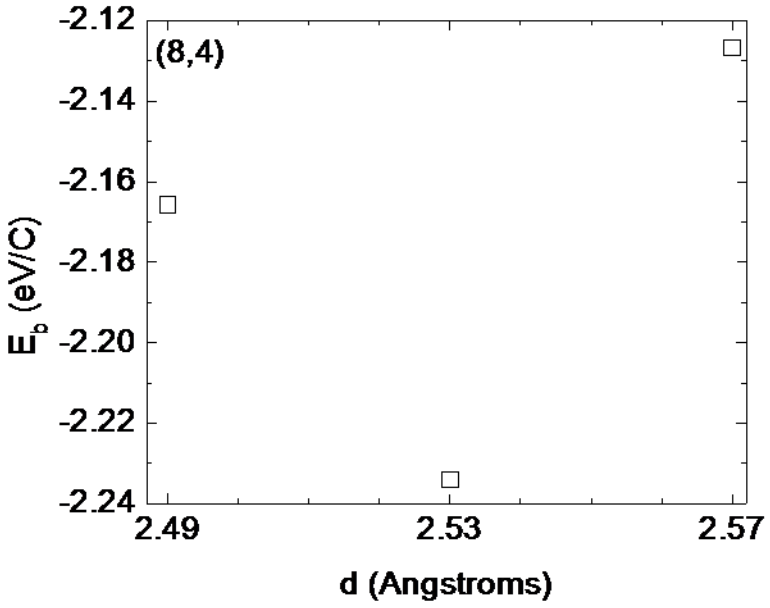

(a)

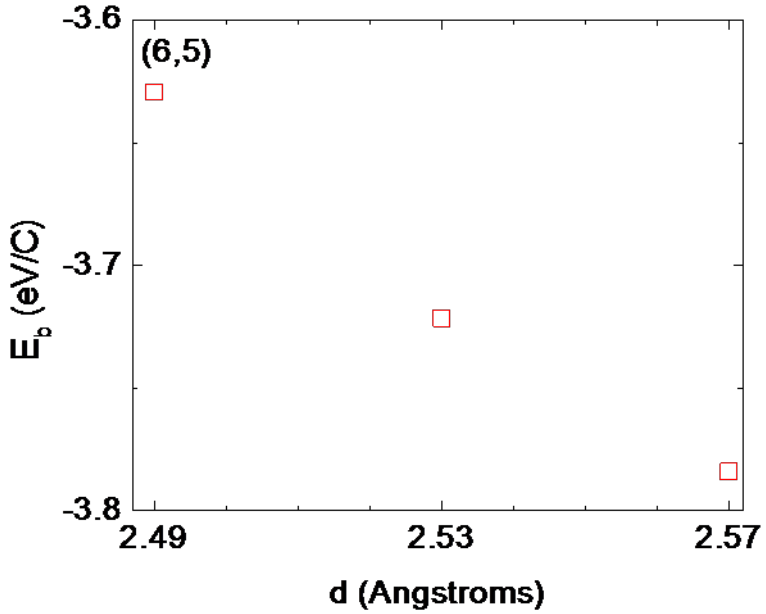

(b)

Figure 4.7: (a) Calculated binding energies, E_b, for (8,4) nanotube caps stabilized on $Ni_{0.27}Fe_{0.73}$(111) catalyst surfaces as a function of the nearest neighbor atom distance, *d*. (b) Calculated binding energies, E_b, for (6,5) nanotube caps stabilized on $Ni_{0.67}Fe_{0.33}$(111) catalyst surfaces as a function of the nearest neighbor atom distance, *d*.

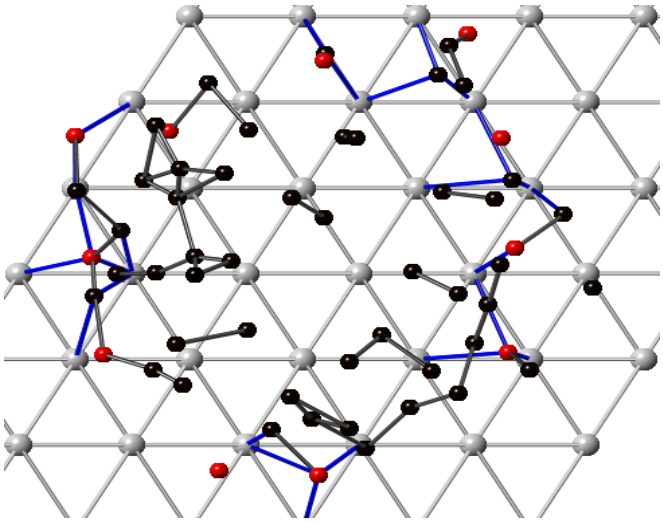

(a)

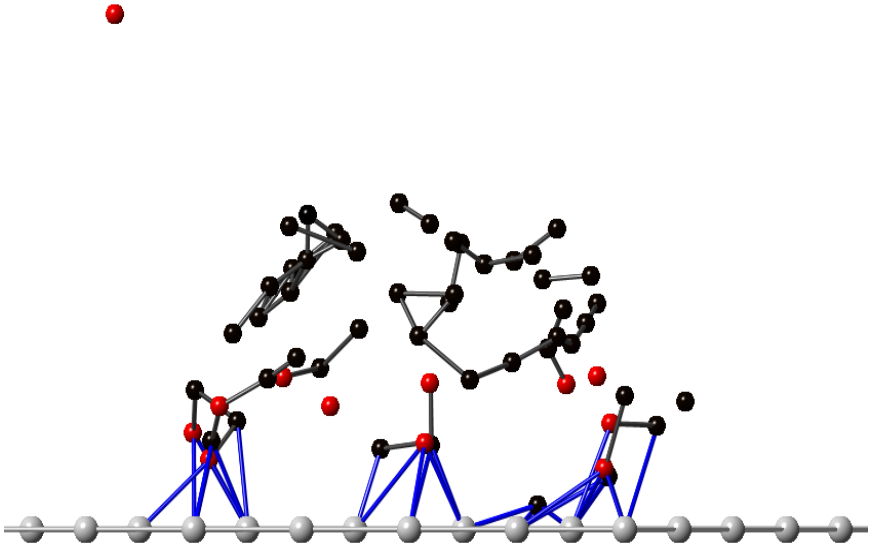

(b)

Figure 4.8: A (10,3) nanotube cap after energy minimization on our Ni (111) model catalyst surface. (a) Top view and (b) Side view. A relaxed cap is not achieved at the end of the energy minimization calculations.

Table 4.2: Correlation of the nanotube rim structure of various chiralities and a specific bond length with the type of binding sites viz. bridge (B), hollow (H) & atop (A), on a model catalyst surface. The nanotube cap for a specific chirality preferably binds to a metallic substrate (specific *d*) where the numbers of atop sites are lower.

Chirality	**d (Å)**	**Hollow (H)**	**Bridge (B)**	**Atop (A)**	**Total edge C atoms**
(8,4)	2.49	4	4	4	12
	2.53	5	4	3	12
(6,5)	2.49	3	4	4	11
	2.57	4	5	2	11
(9,4)	2.49	3	6	4	13
	2.53	4	3	6	13
(8,6)	2.49	4	5	5	14
	2.53	4	4	6	14

CHAPTER 5: PREDICTINGTHE CHIRAL ENRICHMENT OF METALLIC SWCNT ON NICKEL-COPPER BI-METALLIC NANOPARTICLES BY EPITAXIAL MATCHING

5.1 Introduction

Single-walled carbon nanotubes (SWCNTs) are a unique class of nanomaterials, possessing a structure-property relationship that can produce either metallic or semiconducting behavior. Unfortunately, this versatility also presents a significant barrier to technological applications as current growth processes are unable to produce homogeneous material with uniform electrical properties. The atomic-scale structure of SWCNT is defined by a (n,m) chirality which can be visualized as the three-dimensional folding of a graphene sheet into a cylindrical tube. However, nanotubes cannot be formed this way and are instead typically synthesized by exposing a catalytic metal nanoparticle to a carbon precursor gas at high temperatures referred to as catalytic chemical vapor deposition (CCVD).[8,133] The carbon containing gas is cracked at the metal particle surface and the resulting carbon atoms diffuse and dissolve in the particle. When carbon saturates the particle, precipitation of solid carbon occurs in the form of carbon chains and fragments on the metal catalyst surface, eventually leading to the formation of a nanotube cap (i.e. a half-open fullerene).[134] Recent nanotube growth models suggest that the cap is the precursor to a fully-grown nanotube and represents the nucleation step for nanotubes.[135] Following cap nucleation, additional carbon atoms diffuse to the metal-carbon interface, leading to the growth of a full nanotube.

Among the various growth parameters, the metal nanoparticle plays a pivotal role in nanotube nucleation and growth. There has been significant empirical evidence in recent experimental efforts that suggest subtle changes in the size and composition of the nanoparticles can dramatically change the chirality distribution of as-synthesized nanotubes.[8,114] However, a clear correlation between the structure and composition of the nanoparticles and the nanotube chirality-distributions has not yet been established. Recent modeling efforts have hinted at a correlation between the SWCNT chirality and the catalyst structure. Reich *et al.*[32] were the first group to demonstrate how the metal catalyst could preferentially nucleate specific nanotube caps by epitaxial matching. They proposed that lattice matching criterion determine which cap is stabilized on a catalyst and argued that since it is energetically unfavorable to change the nanotube chirality in the growth step, the cap chirality fixes the nanotube chirality. Others have suggested that the nanotube chirality changes during growth[25], but recent evidence indicates such a change is energetically unfavorable.[27] Recent atomistic growth mechanisms for graphene edges on various metal catalysts reveal how carbon atoms can dock at the edges and avoid forming defects by adding only hexagons in the nanotube growth phase.[27] Ding *et al.*[18] have shown that the elongation of the nanotube proceeds by the addition of kinks along the rim of the nanotube that allow only hexagon addition and a 2-layer addition of such armchair kinks leaves the chirality unchanged. Since armchair kinks are more stable than zigzag kinks, armchair tubes preferentially grow. However, external parameters such as metal catalyst and temperature may change this picture. Dumlich *et al.*[37] have showed that energy barriers associated with the conversion of armchair to zigzag kinks can be reduced by the metal catalyst and temperature. In this work, we proposed an epitaxial nucleation model for growth of SWCNTs on Ni_xFe_{1-x} bimetallic catalyst surfaces demonstrating how changes in the catalyst composition and lattice

structure affect the nucleation and growth of specific nanotube chiralities.[8,132] The epitaxial nucleation model is general and can be extended to other bimetallic catalysts, including those that have not been explored experimentally, to predict chirality distributions.

The most commonly used metals for catalyzing nanotube nucleation and growth are transition element metals such as Fe, Ni, and Co that have a strong carbon-metal (C-M) adhesion to stabilize nanotube nucleation.[13] Among these, Ni is especially popular because of its strong C-M adhesion which leads to high nanotube yields, faster growth rates, and structural control in terms of length and diameter of the nanotubes. However, Ni-catalyzed nanotube growth produces a wide distribution of nanotube chiralities.[8] To narrow the distribution of as-synthesized nanotube chiralities, various combinations of metals such as CoMoCAT[114], NiFe[8], and FeCu[30,136] have been explored. These bimetallic nanoparticles narrow down the nanotube chirality distributions to mostly near-armchair nanotubes with semiconducting electronic properties. Fewer reports exist of metallic nanotube enrichment in metal-catalyzed CVD growth processes. Harutyunyan *et al.*[137] recently demonstrated that by changing the noble gas ambient from argon to helium during the thermal annealing of a Fe catalyst, the fraction of metallic tubes could be increased from 30% to more than 90%. Zhou *et al*.[138] showed the growth of high-quality metallic SWCNTs on Si wafers and silica microspheres via a Cu-catalyzed CVD growth process. Using DFT calculations, Yazyev *et al*.[39] studied the binding of mono- and di-atomic carbon species on late transition and coinage metals. Their results showed that Cu favors metallic nanotube growth due to its low diffusion barrier and lower selectivity for the binding of graphene fragments on stepped and flat surfaces.

In this work, we use the epitaxial nucleation model to explain the preferential growth of metallic nanotubes on Cu-based metal catalysts. We compared Cu to Ni, the most commonly

used metal catalyst, and studiedNi_xCu_{1-x} bimetallics which may be an interesting candidate as the advantages of nanotube nucleation and growth on Ni and Cu can be combined to obtain unique populations of nanotubes. We first calculated the energies associated with nanotube cap nucleation on model catalyst surfaces by epitaxial matching. Based on the calculated binding energies, E_b, for each nanotube cap on various metal catalyst surfaces, we observe that the E_b's are in the same order as the C-M adhesion strength. This suggests that the choice of the metal nanoparticle and its C-M adhesion strength are key factors in determining cap nucleation. Also, certain armchair and zigzag nanotube caps show a stronger E_b and hence, a higher chance of nucleation than the chiral caps. Later, we address how the chirality of the nanotubes affects the growth rate and alters the final chirality distribution. We started by calculating the energy barriers involved in the inter-conversion of armchair and zigzag dangling bonds on various metal catalysts. We observe that the differences in armchair and zigzag dangling bond energies decreases as Ni > Cu > $Ni_{0.5}Cu_{0.5}$. It is well known that Cu preferentially grows more metallic nanotubes than Ni due to a smaller difference in dangling bond energies.[39] Hence, the $Ni_{0.5}Cu_{0.5}$ catalyst is likely to be an even better catalyst than Cu in growing metallic nanotubes. This trend is again reflected in the finite-temperature chemical activity ratios where we have incorporated the energy barriers to calculate and predict how a metal catalyst favors the growth of specific nanotube chiralities. Finally, using the chirality-dependent nanotube growth model proposed by Dumlich *et al.*[37,139], we calculated the nanotube growth rates on different metal catalyst surfaces. Certain metallic nanotube chiralities like (5,5), (8,5) and (7,4) show much higher growth rates overall and the nanotube growth rates on any metal catalyst increases in the same order as predicted by the chemical activity ratios. Interestingly, we found that nanotubes grown on lattice-strained $Ni_{0.5}Cu_{0.5}$ surfaces (d=2.56 Å) showed a much higher increase in the chemical

activity ratios and the nanotube growth rates. This suggests that by introducing strain in the Ni_xCu_{1-x} nanoparticle or by changing its composition so as to increase its average bond length, we can preferentially grow metallic nanotubes with much higher abundance than that grown on Cu.

5.2 Computational Details

We applied density functional theory (DFT) calculations to study nanotube cap nucleation and nanotube growth on Ni, Cu, and Ni_xCu_{1-x} catalyst surfaces via epitaxial matching. The total energy DFT calculations were performed using the Vienna *ab-initio* simulation package (VASP).[127] The electron exchange-correlation energy was calculated using the generalized gradient approximation (GGA) as parameterized in the Perdew–Wang functional (PW91).[128] The Ni, Cu, and C core electrons were treated using ultrasoft pseudopotentials[140], and the cutoff energy of the plane-wave basis set for expanding valence electrons was 400 eV. Supercell sizes were sufficiently large to allow for single Γ-point k-space sampling. All calculations were spin-polarized. Total energies were converged to 5 meV. All the nanotube caps used in this study obey the isolated pentagon rule (IPR) as these caps are more stable than those with adjacent pentagons.[7] The nanotube caps were further screened based on the concept of "minimal seed cap"- nanotube caps with the maximum possible number of armchair kinks in the rim structure and having the least number of C atoms to generate the nanotube chirality were selected. However, in some cases, the minimal seed cap could not be stabilized and we selected a non-minimal cap. We used a combination of the CaGe[129] and Avogadro softwares to generate these nanotube cap structures. However, it is important to note that the exact nanotube cap structure is not critical to assess the metal-cap interactions as all dangling bonds are saturated once the nanotube cap stabilizes on the catalyst surface.

Both Ni and Cu are face-centered cubic (fcc) metals with an average metal-metal bond length, *d*, of 2.48 and 2.56 Å respectively. Alloys of Ni and Cu, Ni_xCu_{1-x},also exhibit fcc lattice structures and follow Vegard's law.[141] For example, the $Ni_{0.47}Cu_{0.53}$ alloy has an average bond length of 2.52 Å.[142] The fcc (111) plane has the densest packing of atoms in a surface and is energetically the most stable lattice plane for all fcc metals. We have previously used the 2D fcc (111) surface for Ni_xFe_{1-x} to study the nucleation of various nanotube cap chiralities on Ni_xFe_{1-x} bimetallic catalysts and shown excellent agreement between model and experiments[132]; here, we use a similar approach to study nanotube cap nucleation on Ni_xCu_{1-x} surfaces. Figure 5.1 shows the 3 different model catalyst surfaces used to represent the metallic nanoparticles viz. (a) Ni, (b) Cu and (c) $Ni_{0.5}Cu_{0.5}$.

Well-established rules were used to determine if the nanotube caps were metallic or semiconducting. Based on scanning and tunneling microscopy (STM) images[143] as well as density functional theory calculations[113], it has been concluded that armchair (n=m) nanotubes are always metallic. For the rest of the nanotubes (zigzag and chiral), there exist two possibilities. When the chirality of the nanotube satisfies the relation $n-m=3l$, it is metallic. For $n-m\neq 3l$, the nanotube is semiconducting.

5.3 Results and Discussions

In CCVD growth of a full nanotube on a metal catalyst surface, the final nanotube chirality distributions may depend on a combination of two factors: (a) the nucleation of the carbon cap and its stability on the metal catalyst surface and, (b) a chirality-dependent growth rate of the nanotubes that is based on the interplay between the armchair and zigzag dangling bond energies. In the following sections, we report the results of the DFT calculations obtained

for the nanotube cap nucleation and nanotube growth studies of various Ni, Cu and Ni_xCu_{1-x}surfaces.

5.3.1 Nanotube Cap Nucleation

5.3.1.1 Dangling Bond Energies in Vacuum

For a given nanotube (n,m) chirality, there exist multiple cap structures. It has been previously shown by Reich *et al.*[32] that caps obeying the isolated pentagon rule (IPR) are energetically more stable than those caps having adjacent pentagons. Hence, IPR is a good criterion to reduce the number of possibilities cap structures; however, caps not obeying IPR can also exist for most nanotube chiralities. In this regard, the nanotube caps (5,5) and (9,0) are unique because they have only one nanotube cap structure obeying the IPR. Again, since the cap (5,5) and (9,0) are armchair and zigzag nanotube caps, their rims have only armchair and zigzag dangling bonds, respectively. The armchair and zigzag dangling bond energies in vacuum are given by

$$E_a^{vac} = \frac{E_{C_{60}}/2 - E_{cap}^{(5,5)}}{2\,.\,m} \tag{5.1}$$

$$E_z^{vac} = \frac{E_{C_{78}}/2 - E_{cap}^{(9,0)}}{n - m} \tag{5.2}$$

where, $E_a^{vac}$and $E_z^{vac}$are the armchair and zigzag dangling bond energies in vacuum respectively, $E_{C_{60}}$and$E_{C_{78}}$are the energies of the isolated fullerenes of 60 and 78 C atoms respectively, and, $E_{cap}^{(5,5)}$and $E_{cap}^{(9,0)}$are the energies of the isolated nanotube caps. The (5,5) and (9,0) caps have 30 and 39 atoms, respectively, which can be obtained by dissecting their fullerene analogues of 60 and 78 carbon atoms. E_a^{vac} and E_z^{vac}as were estimated to be 2.33 and 2.80 (eV), respectively, from DFT calculations. The zigzag dangling bond energy compares well with previous DFT

calculations reported in literature of 2.83 eV; however, the armchair dangling bond energy based on DFT calculations reported in the literature is slightly lower (~2.13 eV) than those obtained from our DFT calculations.[36] This discrepancy can be attributed to differences in the carbon nanostructures used in our calculations: whereas we used the entire (5,5) nanotube cap, others used smaller carbon fragments to obtain the dangling bond energies.

5.3.1.2 Epitaxial Matching of Nanotube Caps and Metal Catalyst Surfaces

We applied our 2D fcc (111) model catalyst surface to study the nucleation of a variety of nanotube cap chiralities (total of 14 caps) in the diameter range of 0.65-1.05 nm. The following metal surfaces were studied: Ni, Cu, and $Ni_{0.5}Cu_{0.5}$. In Table 5.1, the structural and electronic properties of the nanotube caps studied are summarized: metallic caps including (5,5), (6,6), (9,0), (12,0), (10,1) and (7,4), and semiconducting caps including (10,0), (11,0), (6,5), (7,5), (8,6), (8,4), (9,4) and (10,3). For the pure Ni and Cu metal catalyst surfaces, the entire surface was comprised of only Ni and Cu atoms, respectively. For the $Ni_{0.5}Cu_{0.5}$ bimetallic catalyst, Ni and Cu atoms were distributed randomly on the catalyst surface in the same relative proportion as their stoichiometric ratio. The average bond lengths were d=2.48 Å and d=2.56 Å for the Ni(111) and Cu(111) surfaces, respectively, consistent with known values. We also studied nanotube cap nucleation on the $Ni_{0.5}Cu_{0.5}$ (111) surface where the average bond length d was systematically changed from 2.48 to 2.52 to 2.56 Å. The bond length was varied in order to understand and decouple the effects of catalyst composition and the average metal-metal bond lengths on the overall chiral-selectivity.

To calculate the overall binding energy associated with cap nucleation, E_b, the difference in energies between the isolated (and re-optimized) nanotube cap and the model catalyst surface was calculated, i.e.,

$$E_b = -(E_{tot} - E_{cap} - E_{catalyst}) \quad (5.3)$$

where, E_{tot} is the energy of the geometry optimized nanotube cap bound to the catalyst, E_{cap} is the energy of the isolated cap and $E_{catalyst}$ is the energy of the isolated catalyst surface. A net negative E_b indicates that the cap-catalyst system is more stable than the separated cap and the catalyst.

Table 5.2 summarizes the binding strengths of the various nanotube caps on the Ni, Cu and $Ni_{0.5}Cu_{0.5}$ fcc (111) catalyst surfaces as well as the lattice-strained $Ni_{0.5}Cu_{0.5}$ fcc (111) catalyst surfaces with d = 2.48 and 2.56 Å E_b for all nanotube caps stabilized on the various metal catalyst surfaces are found to follow Ni > $Ni_{0.5}Cu_{0.5}$ > Cu, in agreement with the ordering of the carbon-metal (C-M) adhesion strengths for the respective metals.[13] All the zigzag nanotube caps have higher binding strengths when compared with the chiral and armchair nanotube caps, irrespective of the metal catalyst surface. Another noticeable feature is that although the nanotube cap binding on the Cu surfaces is significantly lower than that on Ni surfaces, the nanotube cap binding on the $Ni_{0.5}Cu_{0.5}$ is significantly higher than that of Cu and closer to Ni. This suggests that even a relatively small fraction of Ni atoms in a Ni-Cu alloy can contribute to enhanced binding of the nanotube caps. For the nanotube caps bound to lattice-strained $Ni_{0.5}Cu_{0.5}$ (111) surfaces with d=2.48, 2.52 and 2.56 Å, a majority of the semiconducting nanotube caps, except for (11,0), have higher E_b for d=2.56 Å and E_b increases with increasing d. However, no clear trend in E_b emerges is observed for the metallic nanotube caps. Overall, the highest E_b's are observed for the zigzag and near-zigzag (10,1) nanotube caps. It is important to note that the energy differences (~±0.1eV) due to changes in d on the same Ni_xCu_{1-x} surface are significantly lower than changes estimated for E_b on different metal surfaces.

The nucleation of nanotube caps on a metal catalyst surface is facilitated by the gain in energy of the nanotube cap due to the carbon-metal adhesion strength which overcomes the armchair and zigzag dangling bond energies of the isolated nanotube cap. The difference in these energies is the energy cost E_c that has to be supplied externally to the carbon atoms in the form of thermal energy for the nanotube cap to nucleate. In Table 5.1, we have listed the number of armchair kinks (n_{AC}) and zigzag kinks (n_{ZZ}) in the rim of the nanotube cap for all nanotube cap chiralities. We have calculated E_c as

$$E_c = (n_a E_a^{vac} + n_z E_z^{vac}) - E_b \quad (5.4)$$

where, n_a and n_z are the number of armchair and zigzag kinks respectively and, E_a^{vac}, E_z^{vac} and E_b are obtained from Eq. 5.1 and 5.2, respectively. Table 5.3 summarizes the external energy costs, E_c, for all the nanotube caps on the above-mentioned metal catalyst surfaces. The trend for E_c on the various metal catalyst surfaces follows Ni < $Ni_{0.5}Cu_{0.5}$ < Cu which is opposite to the trend in carbon metal adhesion strengths. For most of the achiral caps (armchair and zigzag), E_c is significantly lower than those of the chiral caps. This can be attributed to the *global matching* of achiral caps with the metal catalyst surface which apparently overwhelms the *local matching* of the edge carbon atoms bound to energetically favorable hollow and bridge sites of the metal surface. G*lobal matching* is not possible for the chiral caps as their rim structures are curved which leads to relatively higher E_c than those of the achiral caps. This suggests that certain armchair and zigzag nanotube caps have a higher probability of nucleation on the metal surface than the chiral caps. However, the very strong carbon-metal adhesion in the case of Ni-catalyzed nanotube growth is detrimental to further carbon addition and subsequent growth of metallic nanotubes which explains their very low abundance in experiments. On the other hand, weaker C-M adhesion in the case of Cu could explain the previously reported increase in the abundance

of metallic armchair species on Cu catalysts.[138] Additionally, Ni-Cu catalysts with intermediate adhesion strengths may enable the preferential nucleation of armchair and zigzag nanotube caps. In the following section, we study the nanotube growth process subsequent to cap nucleation and explore the role of the various metal catalyst surfaces in promoting the growth of specific nanotube chiralities.

5.3.2 Nanotube Growth

5.3.2.1 Dangling Bond Energy Differences on Various Metal Catalysts

The nanotube rim consists of zigzag and armchair edges and can have only 3 types of growth sites: armchair (*aa.aa)*, zigzag (*z.z)* and chiral (*aa.z)*.[144]Addition of carbon dimers transforms the rim by continuously changing the number of energetically favorable sites. Thus, the nanotube chirality continuously changes as the nanotube elongates; however, the chirality stops changing after addition of 2 layers of carbon dimers. There is an activation energy barrier associated with the addition of carbon dimmers and this energy barrier is relatively higher for zigzag rims than armchair rims. This is one reason why zigzag nanotubes are rarely observed in CVD growth; however, lowering this activation energy barrier should lead to an increase in the relative abundance of zigzag or near-zigzag nanotubes.

In order to calculate the carbon-metal adhesion strength of armchair and zigzag edges on various metal catalysts, we again used the unique "minimal-seed" nanotube cap structures of (5,5) and (9,0) as in the case of vacuum dangling bond energies. We studied the binding of (5,5) and (9,0) nanotube caps on Ni, Cu and $Ni_{0.5}Cu_{0.5}$ 2D (111) surfaces using DFT calculations. The average bond length, *d*, of the catalyst surfaces was systematically changed from 2.48 to 2.52 to 2.56 Å for each of the metals. When a nanotube cap binds to the metal surface, the C-M

adhesion strength alters the armchair and zigzag dangling bond energies. For any metal surface, the armchair and zigzag dangling bond energies due to C-M binding are given by

$$E_a^{cat} = \frac{E_{(5,5)/cat} - E_{(5,5)} - E_{cat}}{2\,.\,m} \tag{5.5}$$

$$E_z^{cat} = \frac{E_{(9,0)/cat} - E_{(9,0)} - E_{cat}}{n - m} \tag{5.6}$$

where, $E_{(5,5)/cat}$and $E_{(9,0)/cat}$are the combined energies of the cap/catalyst system, $E_{(5,5)}$and $E_{(9,0)}$ are the energies of the isolated nanotube caps, and E_{cat} is the energy of the isolated catalyst.

Figure 5.2 shows the geometry optimized configurations of the nanotube caps (5,5) and (9,0) bound to $Ni_{0.5}Cu_{0.5}$, Ni, and Cu (111) surfaces. The unsaturated carbon atoms with dangling bonds have been highlighted in red and are found to form C-M bonds with atoms in the metal catalyst. The rim of the nanotube is found to restructure and reorient so that most of the edge C atoms occupy the more favorable bridge and hollow sites. Tables 5.4 and 5.5 summarizes the calculated binding energies, E_b, of the nanotube caps (5,5) and (9,0) on Ni, Cu, and $Ni_{0.5}Cu_{0.5}$ (111) surfaces with varying bond lengths, *d*. E_b for both caps shows the trend: Ni > $Ni_{0.5}Cu_{0.5}$ > Cu, irrespective of the average bond lengths. This is consistent with trends in C-M binding for these metal surfaces. Increasing *d* from 2.48 to 2.56 Å increases the C-M binding strength for all the metal surfaces, although the changes are small. An interesting trend is observed for the $Ni_{0.5}Cu_{0.5}$ (111) surface: with an increase in average bond length *d*, the C-M binding strength for the armchair cap (5,5) increases, while the C-M binding strength for the zigzag (9,0) nanotube cap decreases. This suggests that the $Ni_{0.5}Cu_{0.5}$ nanoparticle and its various lattice-strained surfaces are a potential candidate for growing nanotubes having significantly different chirality distributions than those grown on Cu and Ni nanoparticles.

The activation energy barrier associated with the conversion *aa.aa* → *aa.z* sites can be defined as

$$\Delta_a = |E_{za.az} - E_{aa.aa}| = |2E_z - 2E_a| \quad (5.7)$$

From the C-M binding strengths shown in Tables 5.4 and 5.5, we obtained the parameter Δ_a for the various metal surfaces. Figure 5.3 shows that Δ_a for $Ni_{0.5}Cu_{0.5}$ is lower than that for Cu by ~0.06 eV which in turn is lower than that for Ni by ~0.06 eV. Since Δ_a represents the differences in armchair and zigzag dangling bond energies, lowering of Δ_a reflects the possibility of growing more zigzag and near-zigzag nanotubes. Lowering of Δ_a in our calculations for Cu suggest that Cu should have a preference for metallic tubes over Ni, consistent with previous reports.[39] Surprisingly, $Ni_{0.5}Cu_{0.5}$ should have an even stronger preference for metallic tubes than either Ni or Cu. Figure 5.4 shows the optimized geometry of minimal seed nanotube caps (5,5) and (9,0) adsorbed on $Ni_{0.5}Cu_{0.5}$ (111) surfaces with average metal-metal bond length *d* as 2.48, 2.52 & 2.56 Å. We also calculated Δ_a for Ni, Cu, and$Ni_{0.5}Cu_{0.5}$surfaces with *d*=2.48, 2.52 and 2.56 Å (Figure 5.5). We observe an insignificant change in Δ_a for nanotubes grown on pure Ni and Cu metals with varying bond length *d*; however, a significant difference is observed in the case of the $Ni_{0.5}Cu_{0.5}$ surface. For *d*=2.48 Å, Δ_a is higher than that for Ni whereas *d*=2.56 Å reduces Δ_a drastically to 0.42 eV. This suggests that lattice strained surfaces of $Ni_{0.5}Cu_{0.5}$ with a larger bond length could produce a very narrow distribution of metallic nanotubes, in addition to the less often observed zigzag nanotubes. The bond length could be increased in experiments by increasing the Cu content in Ni_xCu_{1-x}bimetallics, as predicted by Vegard's law.

5.3.2.2 Relative Chemical Activity Ratios on Various Metal Catalysts

The binding energy of armchair and zigzag nanotubes can be quantified by the chemical potential per edge atom

$$\mu_{edge} = \mu_{edge}^{vac} + \mu_{edge}^{cat} \tag{5.8}$$

where, $\mu_{edge}^{vac}$and $\mu_{edge}^{cat}$are the chemical potential of the edge atoms in vacuum and attached to a metal catalyst, respectively. Defining μ_{edge}^{vac}=E_a^{vac} and μ_{edge}^{cat}=E_a^{cat} for armchair nanotubes and μ_{edge}^{vac}=$E_z^{cat}$and μ_{edge}^{vac}=$E_z^{cat}$for zigzag nanotubes, the chemical potential per edge atom for the armchair and zigzag edges can be written as

$$\mu_{edge}^{a} = -E_a^{vac} + E_a^{cat} \tag{5.9}$$

$$\mu_{edge}^{z} = -E_z^{vac} + E_z^{cat} \tag{5.10}$$

The chemical potential μ_{edge} provides insight into the abilityof different metal catalysts to grow nanotubes with specific chiralities. A more quantitative measure of the selectivity at a given temperature, T, is estimated by defining the chemical activity ratio

$$R^T = exp\left[-\frac{\mu_{edge}^{a} - \mu_{edge}^{z}}{kT}\right] \tag{5.11}$$

Assuming a reaction temperature of 900ºC, we calculated the R^T values for various metal surfaces based on the C-M binding energies calculated in Table 5.2. Figure 5.6 shows R^T@900ºC for the different metal surfaces: Ni, Cu, and $Ni_{0.5}Cu_{0.5}$, and the lattice-strained surfaces of $Ni_{0.5}Cu_{0.5}$ (d=2.56 Å). We observe a systematic increase in R^T for Ni, Cu, and $Ni_{0.5}Cu_{0.5}$, indicating that $Ni_{0.5}Cu_{0.5}$ exhibits a higher relative selectivity for metallic nanotubes. In addition, the lattice-strained $Ni_{0.5}Cu_{0.5}$surface with an average bond length of 2.56 Å shows a many-fold increase in the R^T value over that of Cu which suggests that lattice-strained Ni_xCu_{1-x} bimetallics may be an excellent candidate for the growth of metallic nanotubes.

5.3.2.3 Chirality Dependent Nanotube Growth Rates on Various Metal Catalysts

Using geometrical arguments, Dumlich *et al.*[37] proposed a method to calculate the effective growth rate of nanotubes on any catalyst at a specific temperature. For a given nanotube cap (n,m) in its starting configuration, the number of growth sites on its rim can be calculated as

$$N_{aa.aa} = \max(2m - n, 0) \tag{5.12}$$

$$N_{aa.z} = \min(m, n - m) \tag{5.13}$$

$$N_{z.z} = 0 \tag{5.14}$$

For tubes with 2m-n ≤ 0 there are only *aa.z* sites and there are no growth sites for zigzag tubes (m=0) and the growth of zigzag nanotubes is suppressed. During nanotube growth, the number of armchair sites *aa.aa* changes continuously whereas the number of zigzag sites *aa.z* remains constant. Growing a full layer of armchair rims on a (n,m) nanotube requires the addition of *n*+*m* carbon dimers. The average growth rate of the nanotubes as a function of nanotube chirality (n,m), activation energy barrier, and temperature dependence is given as,

$$\Gamma(\mathrm{n,m}) = \begin{cases} \dfrac{\Lambda_{aa.aa}(n,m).\delta_a + \Lambda_{aa.z}(n,m).\delta_{az}}{n+m} & \text{if } 2\mathrm{m}-\mathrm{n} > 0, \\ \dfrac{\Lambda_{aa.z}(n,m).\delta_{az}}{n+m} & \text{otherwise,} \end{cases} \tag{5.15}$$

where,

$$\Lambda_{aa.aa}(n,m) = 2m - n - 1 + \frac{1}{2m-n} \tag{5.16}$$

$$\Lambda_{aa.z}(n,m) = N_{aa.z} \tag{5.17}$$

$$\delta_a = exp(-\Delta_a/k_bT) \tag{5.18}$$

$$\delta_{az} = exp(-\Delta_{az}/k_bT) = 1 \tag{5.19}$$

Since there is no activation energy barrier for carbon dimer addition on a *aa.z* rim site, Δ_{az}=0. We calculated the Arrhenius temperature dependent exponential factor, δ_a, for each metal

surface, using Δ_a values from Eq. 5.7. For any given chirality (n,m), we calculated the geometrical probabilities of carbon dimer addition at each of the armchair and zigzag dangling bond sites using Eq. 5.16 and 5.17. We then calculated the growth rates Γ(n,m) for all the nanotube chiralities within a diameter range of 0.65-1.05 nm and at a growth temperature of 900ºC using Eq. 5 15. Γ(n,m) provides the relative differences in growth rate of nanotubes based only on nanotube chiralities. Depending on the nanotube chirality (n,m), the growth factor Γ(n,m) goes from 0 to 0.5. However, the epitaxial growth model assumes that the nanotube diameter and the chirality are both fixed at the nucleation phase. The dependence of the nanotube diameter on the final chirality distribution of nanotubes is taken into account by multiplying a Gaussian distribution function of the nanotube diameters $f(D;\mu,\sigma^2)$ with the nanotube growth rate Γ(n,m),

$$\Gamma^*(n,m) = \frac{1}{\sigma\sqrt{2\pi}} e^{-\frac{(D-\mu)^2}{2\sigma^2}} . \Gamma(n,m) \tag{5.20}$$

We calculated the growth rates Γ*(n,m) for 37 nanotubes with nanotube diameter D varying from 6.87 to 10.68 Å which covers all possible nanotube chiralities within our specified diameter range. We estimated σ=1.137 Å and μ=8.847 Å and calculated the diameter dependent growth rates for each of the nanotube chiralities using Eq. 5.17. The nanotube growth rates Γ*(n,m) for a few of the metallic nanotube chiralities on various metal catalyst surfaces are plotted in Figure 5.7. For all the metallic nanotubes, Γ*(n,m) increases in the order Ni < Cu < $Ni_{0.5}Cu_{0.5}$ < lattice-strained $Ni_{0.5}Cu_{0.5}$(d=2.56Å). The metallic armchair nanotubes have a significant increase in their growth rates Γ*(n,m), with the (5,5) nanotube exhibiting the highest growth rate. Incidentally, the nanotube cap (5,5) was found to have a strong binding strength E_b on the $Ni_{0.5}Cu_{0.5}$ catalyst surface in our nanotube cap nucleation studies. Thus, the (5,5) cap shows the highest probability of growth on $Ni_{0.5}Cu_{0.5}$ and lattice-strained $Ni_{0.5}Cu_{0.5}$ metal catalyst

surfaces. In addition, other metallic chiralities such as (8,5), (7,4) and (9,6) show a significant increase in their growth rates when grown on the bimetallic Ni_xCu_{1-x} catalyst surfaces, suggesting that the Ni_xCu_{1-x} catalyst can serve as an excellent candidate for growing the metallic nanotube species.

5.4 Summary and Conclusions

We have employed DFT calculations to study nanotube cap nucleation and nanotube growth of various SWCNT chiralities on Ni, Cu and $Ni_{0.5}Cu_{0.5}$ surfaces. The binding strengths of the caps with the metal catalyst surfaces follow in decreasing order Ni > $Ni_{0.5}Cu_{0.5}$ > Cu, in accordance with the order of carbon-metal adhesion strengths. Differences in the armchair and zigzag dangling bond energies are lowest for the $Ni_{0.5}Cu_{0.5}$ catalyst suggesting the possibility of a higher abundance of metallic and zigzag nanotubes. The chemical activity ratios and nanotube growth rates confirm that $Ni_{0.5}Cu_{0.5}$ is an excellent candidate for preferentially catalyzing metallic nanotubes. Interestingly, lattice-strained $Ni_{0.5}Cu_{0.5}$ surfaces show an even higher chemical activity ratio and faster nanotube growth rate suggesting that inducing lattice-strain or increasing the average bond length in Ni_xCu_{1-x} bimetallic nanoparticles can lead to significant increase in the populations of metallic nanotubes grown.

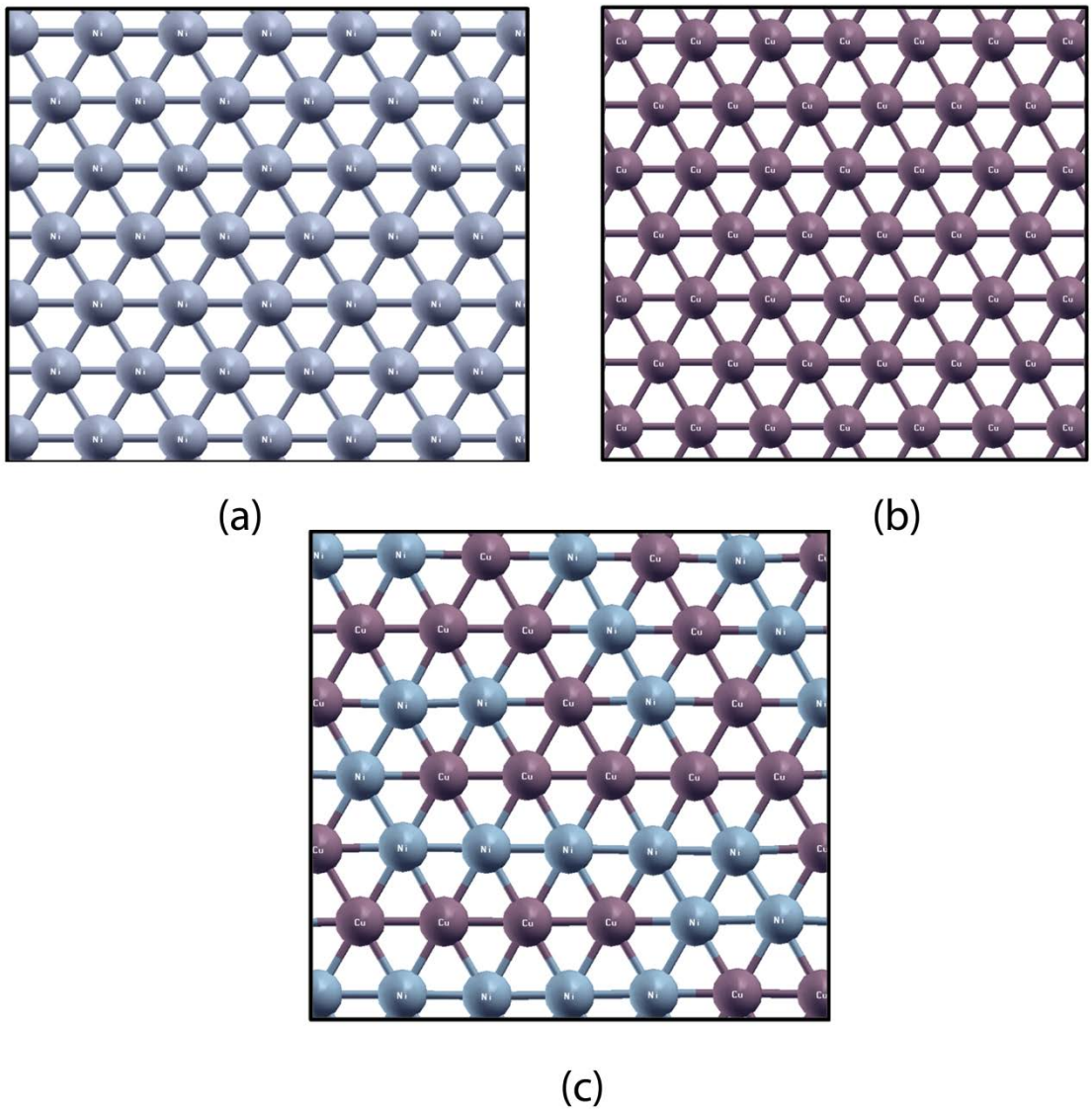

Figure 5.1: Model catalyst surfaces used for studying the epitaxial nucleation of SWCNT cap. 2D fcc (111) planes of (a) Ni, (b) Cu and (c) $Ni_{0.5}Cu_{0.5}$.

Table 5.1: Structural and electronic properties of carbon nanotube caps studied in this work. " * " indicates the metallic nanotube cap chiralities.

(n,m)	**D (Å)**	**Θ (deg)**	**Chiral (C) / Armchair (A) / Zigzag (Z)**	**Rim armchair kinks (n_a)**	**Rim zigzag kinks (n_z)**
(5,5)*	6.87	30	A	10	0
(6,6)*	8.25	30	A	12	0
(9,0)*	7.15	0	Z	0	9
(12,0)*	9.52	0	Z	0	12
(10,1)*	8.36	4.7	C	2	9
(7,4)*	7.66	21.5	C	2	9
(10,0)	7.94	0	Z	0	10
(11,0)	8.73	0	Z	2	9
(6,5)	7.57	27	C	10	1
(7,5)	8.29	24.5	C	10	2
(8,6)	9.66	25.3	C	2	12
(8,4)	8.4	19.1	C	2	10
(9,4)	9.15	17.5	C	2	11
(10,3)	9.36	12.7	C	6	7

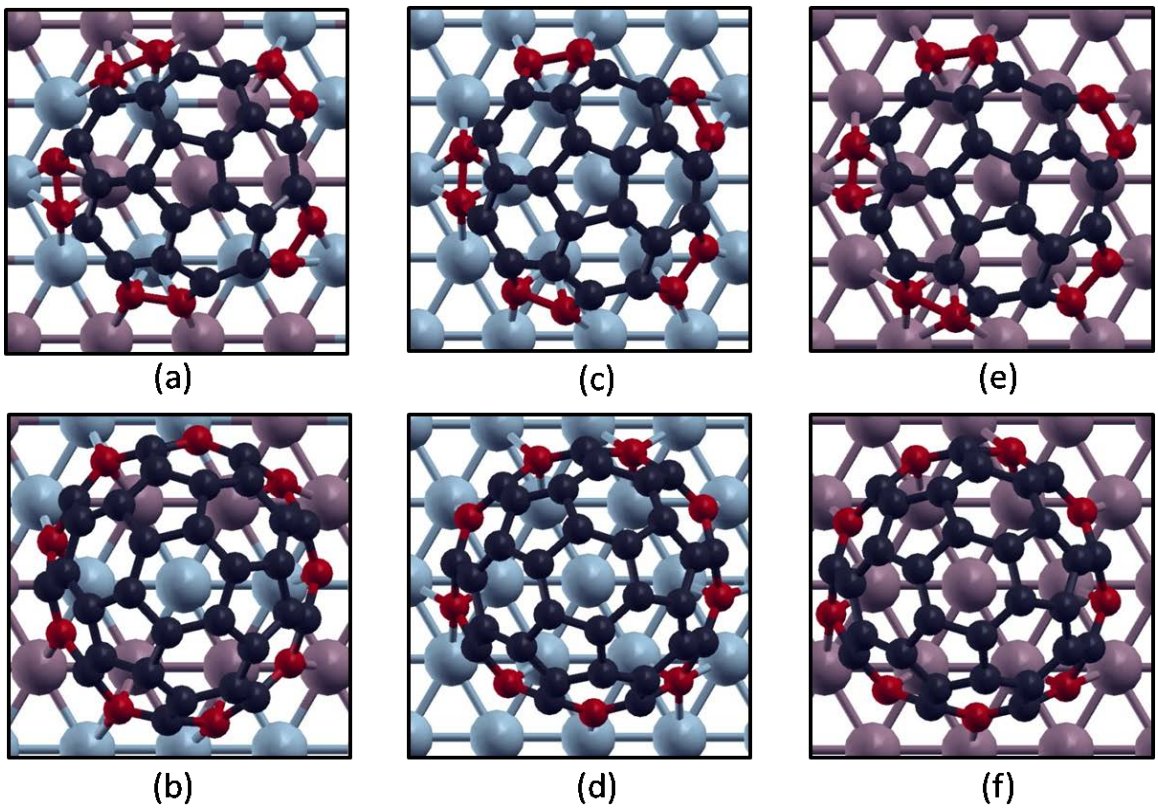

Figure 5.2: Minimal seed SWCNT caps (5,5) and (9,0) adsorbed on (a,b) $Ni_{0.5}Cu_{0.5}$, (c,d) Ni and (e,f) Cu (111) surfaces respectively.

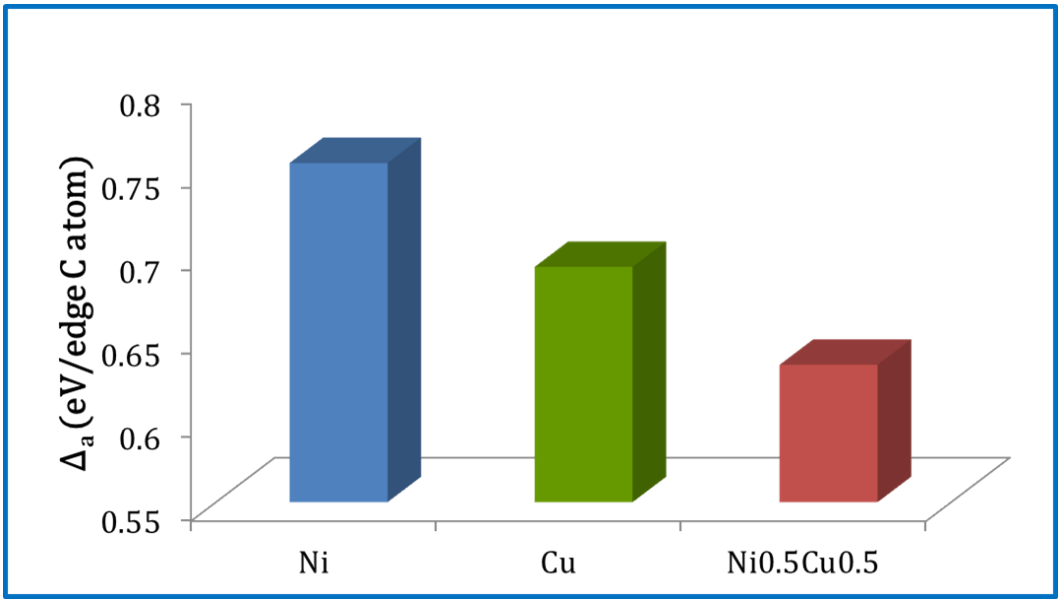

Figure 5.3: Calculated energy barriers in the inter-conversion of armchair and zigzag dangling bonds on various metal catalyst surfaces.

Table 5.2: Binding energies, E_b (eV/edge C atom) of the metallic and semiconducting nanotube caps adsorbed on Ni, Cu, $Ni_{0.5}Cu_{0.5}$ (111) surfaces. Similarly, E_b's for lattice-strained $Ni_{0.5}Cu_{0.5}$ (111) surfaces with d = 2.48 and 2.56 Å are also reported. " * " indicates metallic nanotube caps and " ! " indicates non-minimal nanotube caps used in this study.

Chirality	**Ni**	**Cu**	**$Ni_{0.5}Cu_{0.5}$**	**$Ni_{0.5}Cu_{0.5}$@ d=2.48Å**	**$Ni_{0.5}Cu_{0.5}$@ d=2.56Å**
(5,5)*	2.24	1.39	1.94	1.88	1.98
(6,6)*	1.84	1.13	1.57	1.68	1.65
(9,0)*	2.62	1.73	2.25	2.28	2.19
(12,0)*	2.39	1.57	2.19	2.16	2.24
(10,1) *!	2.30	1.50	2.06	2.00	2.11
(7,4) *!	2.02	1.11	1.74	1.70	1.47
(10,0)	2.57	1.63	2.11	2.07	2.18
(11,0)	2.34	1.60	2.25	2.07	2.13
(6,5) !	2.18	1.59	1.80	1.76	1.98
(7,5) !	2.11	1.29	1.97	1.93	1.99
(8,6) !	2.28	1.46	1.91	1.88	1.98
(8,4)	2.23	1.37	1.92	1.94	1.94
(9,4)	2.18	1.27	1.95	1.92	1.98
(10,3)	1.90	1.15	1.70	1.64	1.75

Table 5.3: External energy costs E_c (eV/edge C atom), which is the difference between the vacuum dangling bond energies and the carbon-metal adhesion energies of the nanotube nucleation on various metal catalyst surfaces. " * " indicates metallic nanotube caps and " ! " indicates non-minimal nanotube caps used in this study.

Chirality	**Ni**	**Cu**	**$Ni_{0.5}Cu_{0.5}$**	**$Ni_{0.5}Cu_{0.5}$@ *d*=2.48Å**	**$Ni_{0.5}Cu_{0.5}$@ *d*=2.56Å**
(5,5)*	0.09	0.94	0.39	0.45	0.35
(6,6)*	0.49	1.20	0.76	0.65	0.68
(9,0)*	0.18	1.07	0.55	0.52	0.61
(12,0)*	0.41	1.23	0.61	0.64	0.56
(10,1) *!	0.41	1.21	0.65	0.71	0.60
(7,4) *!	0.69	1.60	0.97	1.01	1.24
(10,0)	0.23	1.17	0.69	0.73	0.62
(11,0)	0.37	1.11	0.46	0.64	0.58
(6,5) !	0.19	0.78	0.57	0.61	0.39
(7,5) !	0.30	1.12	0.44	0.48	0.42
(8,6) !	0.45	1.27	0.82	0.85	0.75
(8,4)	0.49	1.35	0.80	0.78	0.78
(9,4)	0.55	1.46	0.78	0.81	0.75
(10,3)	0.68	1.43	0.88	0.94	0.83

Table 5.4: Carbon-Metal (C-M) binding energies E_a of nanotube cap (5,5) adsorbed on Ni, $Ni_{0.5}Cu_{0.5}$ and Cu (111) surfaces with *d* = 2.48, 2.52 and 2.56 Å for each surface.

Cap (5,5)	***d* = 2.48 Å**	***d* = 2.52 Å**	***d* = 2.56 Å**
Ni	**2.24**	2.30	2.34
Cu	1.29	1.34	**1.39**
$Ni_{0.5}Cu_{0.5}$	1.88	**1.94**	1.98

Table 5.5: Carbon-Metal (C-M) binding energies E_z of nanotube caps (9,0) adsorbed on Ni, $Ni_{0.5}Cu_{0.5}$ and Cu (111) surfaces with *d* = 2.48, 2.52 and 2.56 Å for each surface.

Cap (9,0)	***d* = 2.48 Å**	***d* = 2.52 Å**	***d* = 2.56 Å**
Ni	**2.62**	2.67	2.71
Cu	1.64	1.69	**1.73**
$Ni_{0.5}Cu_{0.5}$	2.28	**2.25**	2.19

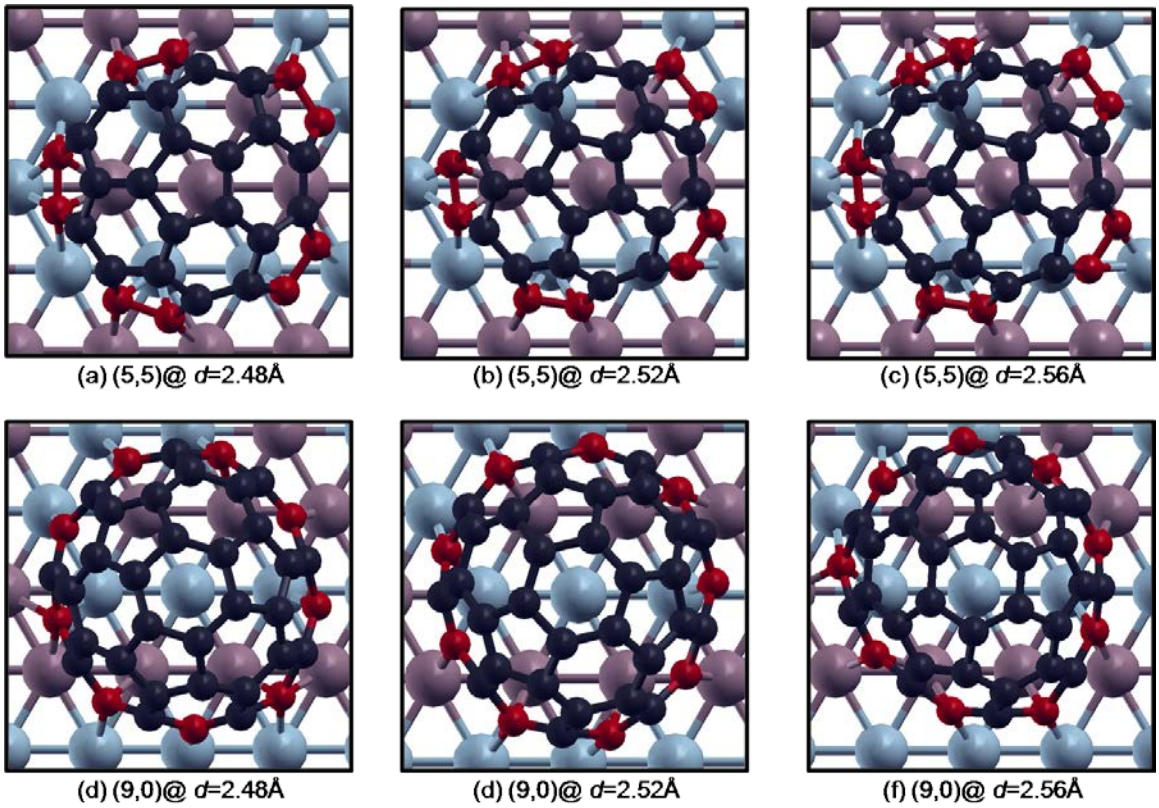

Figure 5.4: Minimal seed nanotube caps (5,5) and (9,0) adsorbed on $Ni_{0.5}Cu_{0.5}$ (111) surfaces with average bond length ***d*** as 2.48, 2.52 & 2.56 Å.

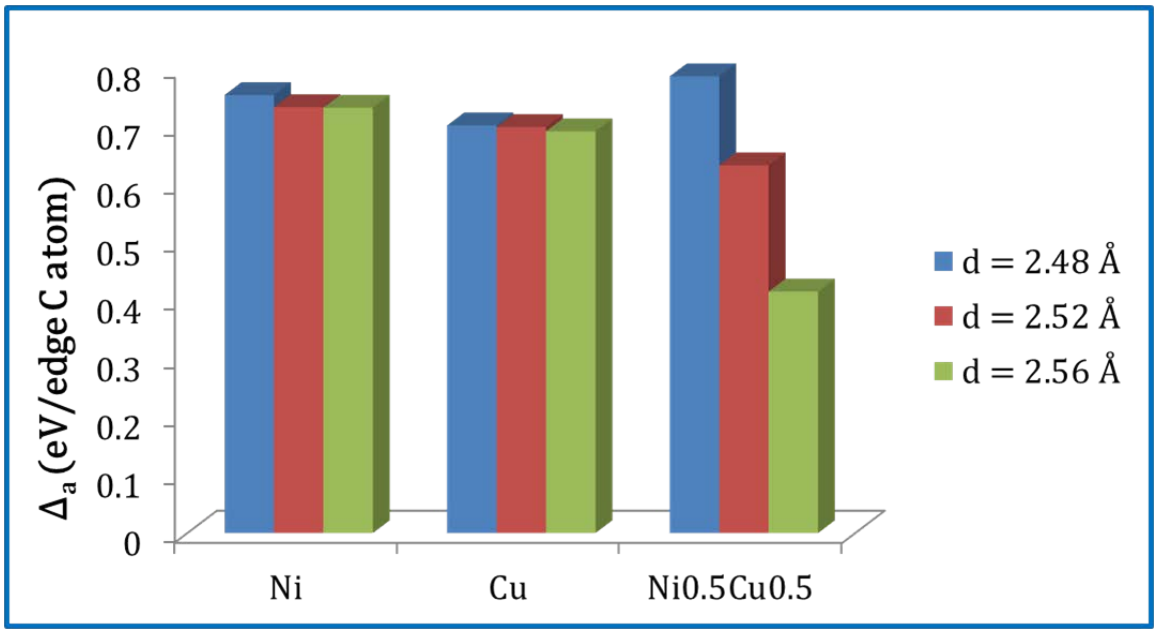

Figure 5.5: Calculated energy barriers for the armchair to zigzag conversion on various metal catalysts with varying metal-metal bond lengths, ***d***.

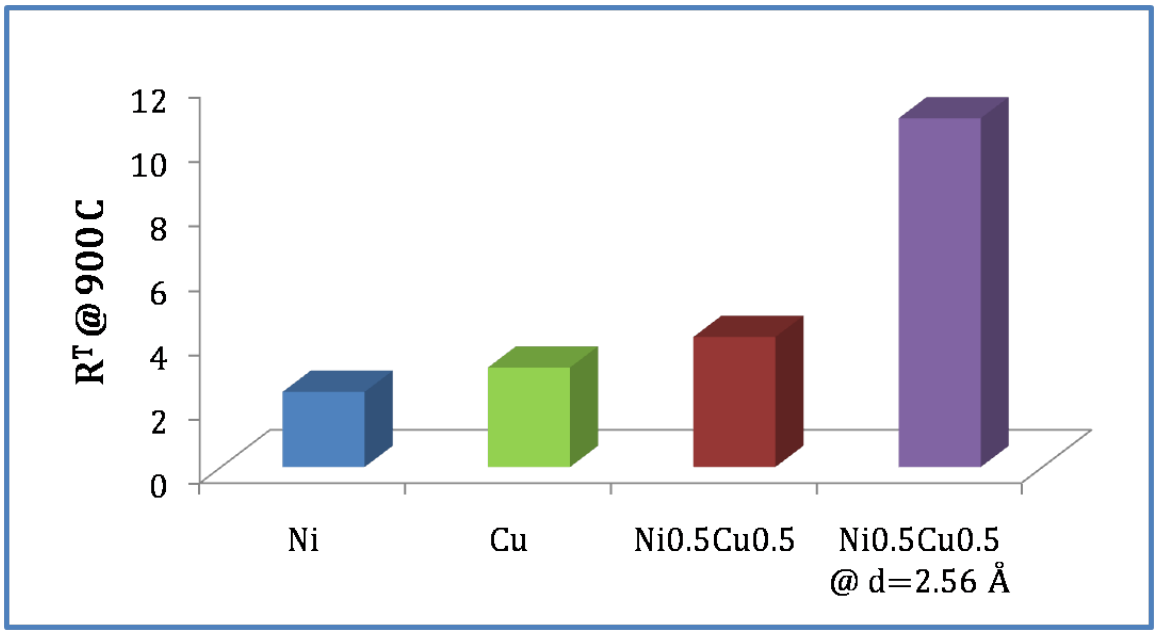

Figure 5.6: Chemical activity ratios of nanotubes grown on various metal nanocatalysts at T= 900°C.

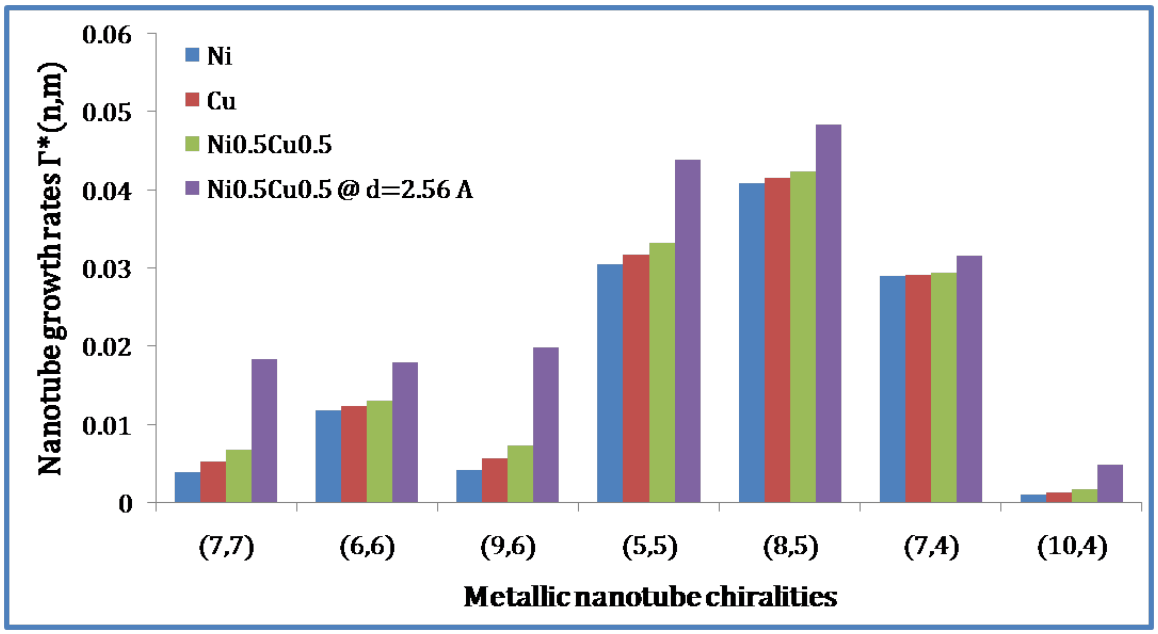

Figure 5.7: Nanotube growth rates Γ*(n,m) of various metallic nanotubes on different metal nanocatalysts at T= 900°C.

CHAPTER 6: EXPLORING THE EPITAXIAL RELATIONSHIPS BETWEEN THE GROWTH ORIENTATION OF SEMICONDUCTING NANOWIRES AND METAL CATALYST SURFACES

6.1 Introduction

Semiconductor nanowires (s-NWs) have attracted a great deal of interest as nanoscale building blocks for potential applications in advanced electronics, optical devices, sensors, and energy conversion. The quasi one-dimensionality of the nanowires leads to very interesting and unparalleled properties due to effects of quantum confinement. For example, III-V materials such as the InAs NWs are characterized by high electron mobilities[53], polarizable photoluminescence[54], and strong spin-orbit interactions.[55] Despite significant progress that has been made over the last several years to synthesize s-NWs, a significant obstacle that remains for fundamental research and technologies based on s-NWs is precise control over their structure (i.e. defects, crystalline orientation, etc.). The crystal structure of s-NWs can influence their electronic[81] and optical[78] properties and has not been sufficiently controlled. For example, III-V NWs are characterized by twin defects, stacking faults, and polytypism that result in lower quantum efficiency, carrier lifetime, and carrier mobility.[145] Nanowires are usually grown via the vapor-solid-liquid (VLS) mechanism which involves the eutectic reaction of a semiconductor vapor source on a metallic seed particle.[15] However, a vapor-solid-solid (VSS) mechanism of the s-NW growth on metallic seed particle is also possible in which the reaction takes place below the eutectic temperature and the metal seed particle remains solid.[82] The metal

nanoparticle plays a critical role in controlling the s-NW diameter and growth orientation.[56,57] In addition, the nanoparticle material also influences the dissolution of the semiconductor gas and the diffusion of the atoms in the metal nanoparticle thereby affecting nanowire growth rates. Au is often used because of its low eutectic melting temperature which facilitates VLS growth.[15] By incorporating a second metal (with Au), the eutectic melting temperature is increased, keeping the particle solid during NW growth and preventing the so called "reservoir effect" where the dissolved semiconductor rapidly diffuses out of the metal particle.

The control in growing large vertical arrays of s-NWs with specific orientations is imperative to build s-NW based nanoscale devices for commercial logic gate applications. For most of the III-V nanowires with zinc blende crystals (i.e. GaAs, InAs, InP, GaP, etc.), it has been observed that the semiconductor NW-catalyst interface usually forms a single surface at the lowest energy (111) plane and hence, the <111> nanowire orientation is the most commonly observed nanowire growth directions under most reaction conditions.[15,78] For nanowires with a wurtzite crystal structure (e.g. ZnO, GaN), the <0001> (c-axis) growth direction is the most commonly observed nanowire orientation. There has been recent evidence in the literature that the metal particle influences the final structure and orientation of the as-grown nanowires through an epitaxial relationship. Han *et al.*[82] have demonstrated that epitaxial relationships between the crystal phase of Ni_xGa_{1-x} seed nanoparticles and growth orientations of GaAs NWs. Xu *et al.*[146] grew defect-free pure ZB<111>InAs NWs on GaAs(111) substrates using palladium. More recently, epitaxial relationships have also been reported for GaAs NWs grown on non-metallic substrates like graphite and a few layers of graphene (FLG).[147] A very conclusive evidence of the epitaxial behavior is demonstrated in the horizontal in-plane growth of ZnO[80] and GaN[81] nanowires on various planes of a sapphire substrate.

6.2 Experimental Background

A particularly novel aspect of our experiments at CWRU is the study of shape-controlled particles for s-NW growth. Although there have been empirical observations of faceting of the metal particles during s-NW growth, to our knowledge, we are the only group to have used pre-formed shaped particles for s-NW growth.[83] In our experiments on InAs nanowire (NW) growth on shaped Au nanoparticles, we have observed that the growth rate of the NWs is considerably enhanced when grown on shaped Au nanoparticles compared to that on spherical nanoparticles. Shaped Au nanoparticles have highly faceted (111) and (100) surfaces as confirmed experimentally by X-ray diffraction (XRD) or HRTEM images of our colloidally synthesized Au nanoparticles. Au has a face centered cubic (fcc) lattice structure and the Au (111) facet is the most stable surface plane observed on an Au nanoparticle. Since shaped Au nanoparticles have more Au (111) and Au (100) surfaces than the spherical Au nanoparticles, our target is to explore whether an epitaxial relationship can be established between the orientation of the InAs NW growth direction and the surface facets of the gold nanoparticle on which the NW grows. If such an epitaxial relationship can be established, then this would provide insights to experimentalists about tailoring the growth of specific orientations of InAs NWs on various shape-controlled Au nanoparticles. This would ultimately allow for catalyst selection and design.

Whereas spherical particles are composed of randomly coordinated atoms on their surface, shaped particles have well-defined crystallographic orientations, much like single-crystal substrates. However, we note that shaped particles have more than one orientation since they are not extended surfaces like substrates. Nonetheless, we believe that shaped particles could have important benefits to controlling nanowire growth. This hypothesis is based on previous studies with SWCNTs (as shown in chapters 4 & 5) that have shown the preferential

growth of metallic tubes with highly faceted Ni-Fe particles. In addition, results for NWs grown from single crystal substrates suggest that the crystal structure of NWs can be controlled through a lattice matching in the case of shaped nanoparticles; this could be potentially achieved by surface faceting of the gold nanoparticles.

6.3 Computational Methods and Models

The role of the DFT calculations is to explore the epitaxial relationships that may exist between the semiconducting nanowires and the metal catalysts. The formation of different crystal structural polytypes in the III-V nanowires is quite a common phenomenon because the atomic layers have the same in-plane structure normal to the most common <111> growth direction.[148] Different crystal structures arise due to the difference in the stacking sequence of the atoms in the <111> growth direction and consequently, both the wurtzite (WZ) and zinc blende (ZB) phases co-exist in a single NW due to presence of stacking faults and twinning planes. However, single-phase purity of the InAs NWs is required for electronic applications. Hence, if an epitaxial relationship can be established between the crystal structures of the InAs NW with the Au surface facets on which the NW grows, then it can be exploited to synthesize pure single phases of WZ or ZB InAs NWs.

The total energy calculations reported in this study have been performed using VASP, a plane wave, periodic boundary conditions DFT code. For the present calculations, we have used Vanderbilt ultrasoft pseudopotentials. A generalized gradient approximation (GGA) level of theory is included through the Perdew–Wang ’91(PW91) exchange and correlation functional. Since we have a fairly large unit cell, integration over the Brillouin zone for the unit cell is achieved by sampling reciprocal space with a Γ-point sampling.

The DFT based modeling of the nanowires is very expensive as the number of atoms involved in the system increases drastically with the increase in diameter. As a result, any atomistic simulation based on *ab-initio* techniques really becomes intractable beyond the diameter of 3 nm. In addition, to study the epitaxial relationship of the nanowires with the metal catalyst surface, the number of metal atoms in the catalyst surface has to be included as well as the periodicity of the nanowires in its axial growth direction has to be terminated. All this leads to the DFT study of the epitaxial relationship between the nanowire-nanocatalyst surfaces being extremely expensive. The InAs nanowire is characterized by its surface to bulk ratio of atoms. All the atoms in the interior of the InAs nanowires are bulk-like sp^3-hybridized having tetrahedral bonds whereas the edge atoms along the circumference have dangling bonds. Hence, to model a nanowire of any diameter, one can divide the nanowire into the interior and peripheral sections. Hence, we have devised a method in which we study the binding of small diameter zinc blende and wurtzite nanowire and nanotube fragments on gold metal catalyst surfaces. For the same diameter of InAs fragment we study both the nanowire and the nanotube binding to the gold surfaces. All the atoms in the InAs nanotube have surface dangling bonds, whereas in the InAs nanowire the surface atoms have surface dangling bonds and the bulk atoms are sp^3-hybridized. Thus, to estimate the binding strength of large diameter nanowires, we estimate the surface fraction of the atoms in the nanowire and then, add the binding strength contributions of the peripheral and bulk atoms to the Au surfaces obtained from the model fragment calculations.

In this work, we have established the relative binding strengths of ZB and WZ H-terminated InAs NW fragments with particular facets of an Au nanoparticle using density functional theory (DFT) calculations. In particular, we have first established the binding strengths of (i) an H-terminated <0001>, <10-10> and <11-20> oriented wurtzite (WZ) InAs

NW and NT fragments with Au(111) and Au(100) surfaces and, (ii) an H-terminated <111>, <100>and <110> oriented zinc blende (ZB) InAs NW and NT fragments with Au(111) and Au(100) surfaces. Our current approach to model the NW-metal catalyst interaction is based on our previous efforts to model the effect of bimetallic nanoparticle composition on nanotube nucleation as in chapters 4 and 5.[132] There, we studied the binding strengths, E_b, of various nanotube chiral caps on a simplified 2D lattice of Ni(111) surface. The change in the composition of the bimetallic nanoparticles was represented by a change in the average bond length, *d*, of the Ni atoms and, the observed trends in the E_b vs. *d* plots for various nanotube chiral caps had an excellent agreement with our experimental observations of some of the nanotube chiralities grown on the Ni_xFe_{1-x} bimetallic catalyst surfaces.

Figures6.1, 6.2 and 6.3 show both ZB and WZ phases of InAs nanowire and nanotube fragments with the axial growth directions of <111>, <100> and <110>respectively. We have terminated the top layer in these fragments with hydrogen atoms such that all the interior atoms are sp^3-hybridized and the peripheral atoms are sp^2-hybridized. We have considered 8 layers of ZB nanowire and nanotube fragment having 4 In and 4 As atomic layers. However, we have only considered 4 layers for the WZ fragments since the total number of atoms become prohibitively large. It is ensured that the bottom layer for both the <111> and <100> NW consists entirely of In atoms which have unsaturated dangling bonds as it is known from the experiments that the InAs nanowire grows from the $InAu_2$ alloy. However, in the case of the <110> NW and NT fragments both the In and As atoms occupy the bottommost layer.

The binding energy (E_b) of the InAs fragments with the Au catalyst surface is calculated as

$$E_b = E_{tot} - E_{Au} - E_{frag} \tag{6.1}$$

where, E_{Au} and E_{frag} is the absolute energy of the geometry optimized isolated Au catalyst surface and the isolated H-terminated nanowire/nanotube fragment and, E_{tot} is the total energy of the NW/NT fragment and the Au catalyst surface. Though the binding energy gives an estimate of the relative binding strengths of the various fragments with the gold catalyst surfaces, it will be erroneous to compare across various fragments as the isolated nanotube and nanowire fragments undergo considerable bonding reconstruction due to the presence of unsaturated dangling bonds. So, a better way to compare the interactions of various systems is to calculate the excess energies of the adsorbed systems with respect to the bulk InAs (ZB/WZ phase) and Au surfaces as follows

$$E_x^i = E_{tot} - E_{Au} - n_B E_{InAs}^i - \frac{n_H E_{H_2}}{2} \quad (6.2)$$

where, E_{InAs} is the energy for a bulk InAs pair with i referring to either WZ or ZB phase, E_{H_2} is the energy of a H_2 molecule, and n_B and n_H are the number of InAs pairs and Hydrogen atoms in the H-terminated nanowire or nanotube fragment. These modeling efforts can be extended to study the epitaxial relationships of various orientations and phases of s-NWs with shape-controlled or bimetallic model catalyst surfaces. We expect that our modeling efforts will provide deep insights to our efforts to synthesize metallic nanoparticles that will grow defect-free single-phase s-NWs with specific orientations.

6.4 Results and Discussions

6.4.1 Geometry of Adsorbed Systems

We have first calculated the bulk energies of the WZ and ZB structures for the InAs material. The total energy minimization for the bulk unit cell results in the following lattice parameter for the ZB phase: a^{InAs} = 6.058 Å. For the WZ structures we obtain: a^{InAs} = 4.327 Å and c^{InAs} = 7.092 Å. These results are in excellent agreement with previously reported DFT

calculations and experimental data. For all the nanowire fragments adsorbed on Au surfaces studied in this work, the In atoms attached to the Au surface tend to occupy the hollow sites of Au surface such that each In atom is sp^3-hybridized and has 3 In-As bonds attached to the Au surface. As our simulated InAs NWs we are studying are quite small (< 2 nm), the In-As bonds in both the isolated fragments of WZ and ZB NWs tend to stretch and re-orient themselves by radial expansion. This radial stretching of the In-As bonds along the edge of the fragments is more pronounced for the ZB phase than that of the WZ phase. This supports the numerous experimental observations that for small diameter NWs, the WZ phase of the NW is more stable than the ZB phase. Indeed, small-diameter InAs NWs are rarely seen in experiments because of the Gibbs-Thompson effect. This can be explained atomistically by the fact that the stability of the NW increases by radial expansion as both In and As atoms are more stable when they get sp^3-hybridized. A NW gets stabilized only when the surface-to-inner atom ratio decreases considerably and this happens only in NWs with diameter larger than 5 nm.

Figures 6.4 and 6.5 show the initial and final configurations of the WZ(0001) NW adsorbed on the Au(100) surface and the ZB(111) NW adsorbed on the Au(111) surface respectively. Figure 6.6 shows the geometry optimized final configurations of the WZ(11-20) NW and ZB(110) NW with their areal cross-sectional and lateral side views. The main visible effect on the geometrical optimization of the nanowire on the Au surfaces is the interatomic bonding reconstruction at the nanowire lateral surface while the inner core of the nanowire remains unaffected. The change in the shape of the nanowire surface after relaxation can be attributed mainly due to the change in the position of cations like In atoms tending to a planar configuration. There is considerable radial strain due to bond stretching and consequently, the average In-As bond length increases significantly. The distortion of the ZB nanowire is much

greater than WZ nanowire as the As atoms in the ZB have higher energy as they are only 2 co-ordinated. Figure 6.7 shows the side views of all the <111> and <100> nanowire/nanotube fragments adsorbed on the Au(111) surface after geometrical optimization. Strong In-Au bonding is observed for the sp^3-hybridized central In atoms in the NW whereas the In-Au bonding for the peripheral In atoms is much weaker. The ZB(100) and WZ(10-10) nanowires as well as nanotubes have a bottom layer reconstruction such that In and As atoms form a single layer. Both In-Au as well as As-Au bonding is observed. On the other hand, the ZB(111) nanowire adsorbed on the Au(111) surface is the only In-Au binding with no bottom layer reconstruction and no As-Au bonds. Others have some As-Au bonding. In general, the ZB(111) and WZ(0001) nanowire and nanotube have strong In-Au bonding with very few As-Au bonds. Equal number of In-Au and As-Au bonds are observed for the (100) orientations of the nanotube and nanowire fragments adsorbed on both Au(100) and Au(111) surfaces. Since the WZ(11-20) NW and ZB(110) NW has both In and As atoms in their bottommost layer, both the atoms attach to the Au surface and hence, these <110> nanowires are likely to bind strongly to a Au(100) surface than to a Au(111) surface.

6.4.2 Energetics of Adsorbed Systems

Table 6.2 lists the binding energies (E_b) as well as the excess energies (E_x) of the nanowire/nanotube fragments adsorbed onAu(111) and Au(100) surfaces. Both E_b and E_x are reported as the energy per atom for the total number of atoms in the combined nanowire or nanotube fragments and the Au surfaces. A more negative $E_b$or a lower magnitude of E_x suggests a higher stability of the adsorbed NW-Au system. The general trends observed for the nanowire/nanotube fragments are consistent for both E_b and E_x values. As observed from Table

6.2, the WZ phase is more stable than the ZB phase on any of the Au surface facets for both the nanowire and nanotube fragments.

Similar results, as the enhanced stability of the ZB InAs NW on the Au (111) surface, has been previously observed for GaAs NWs grown on Au nanoparticles where the entire NW is in a pure ZB phase in the initial stages of nucleation. Another notable feature observed from the binding energies in Table 6.2, is that both the WZ(0001) and ZB(111) NW fragments are more stabilized by the Au(111) surface than the Au(100) surface while both the <100> and <111> NW fragments strongly bind to the Au(100) surface than that on the Au(111) surface. This suggests that spherical Au nanoparticles with higher Au(111) facets should have higher yield and formation of the InAs NWs with the general <111> growth direction. However, since the shaped NPs like Au nanocubes or Au nanotriangles have a higher abundance of ofAu(100) than Au (111) facets, both the <100> and <110> NWs are likely to preferentially grow on the shaped nanoparticles. Based on the excess energy analysis, the NT is always less stable than NW on any Au surface which is in accordance with isolated NT and NW as the NT with higher dangling bond energies is always less stable. WZ(0001) NW is the most stable fragment as it has lowest excess energy. WZ is always more stable than ZB on any Au surface facet similar to that observed in case of isolated nanowires. In particular, various epitaxial relationships have been observed. The general <111> NW orientation are more stable on the Au(111) surface than on the Au(100) surface whereas the general <100> and the <110> NW orientations are more stable on the Au(100) surface than on the Au(111) surface. Based on the E_x numbers, the <110> NW has a higher selectivity of growing on the Au(100) surface than the <100> NW. However, the overall stability of the <111> oriented NWs are always higher than the <100> oriented NWs.

6.4.3 Charge Redistribution of Adsorbed Systems

The geometry optimized structures obtained from the DFT calculations were also used to consider the electron redistribution caused by the interaction of the nanowire/nanotube fragments adsorbed on the Au surfaces. Figures 6.6 and 6.7 shows the change in electronic charge density at an isosurface of 0.005 (eV/Å^3) due to the nanowire fragments binding to the Au surface obtained by the equation $\rho_{total} - \rho_{Au} - \rho_{frag}$. The charge difference maps in Figures 6.6(a) and Figures 6.7(a) show there is strong electronic charge redistribution for the <111> oriented nanowire fragments on the Au(111) surfaces. From the above images, it becomes abundantly clear that both the ZB(111) and WZ(0001) nanowire fragments have a very strong electronic interaction with the Au(111) surface. However, while there is electron accumulation along the In-As bonds and electron depletion in the intermediate space for the ZB(111) nanowire fragments, the WZ(0001) fragment shows a layer of strong electron depletion for the In-Au bonding and a layer of strong electron accumulation for the In-As bonds. This might be a reason for stronger In-Au bonding for the WZ(0001) fragment than that of the ZB(111) fragment on the Au(111) surface. However, for the same <111> nanowire fragments adsorbed on the Au(100) surfaces there is very little electron redistribution as observed in the case of WZ(0001) nanowire adsorbed on Au(100) surface (see Figure 6.7(b)) which clearly suggests the growth preference of the <111> nanowires on the Au(111) surface over the Au(100) surface. Similarly, the <100> orientation of the nanowire fragments on both the Au(111) and Au(100) surfaces have very weak electronic charge redistribution as observed in the case of ZB(100) adsorbed on Au (100) surface (see Figure 6.6(b)) suggesting a weak binding of the <100> nanowire fragments to the Au surfaces. The trends of the electronic charge redistribution for the <110> NW orientations are similar to <100> NWs.

6.5 Summary and Conclusions

In this work, we have explored the epitaxial behavior of various specific orientations of nanowire fragments on different Au surfaces using density functional theory calculations. The results of the DFT calculations show that the <111> oriented nanowire fragments for both the wurtzite and zinc blende structures are more stable than the <100> and <110>oriented nanowire fragments and particularly, within the size range of the study (< 5 nm), the wurtzite phase is more stable than the zinc blende phase. Again, the relative stability of the <111> nanowire fragment on the Au(111) surface and that of the <100>and <110>nanowire fragment on the Au(100) surface is demonstrated by calculating the binding energies, excess energies and electronic charge redistribution of various nanowire fragments on the different Au surfaces. The results of the DFT calculations provide a very exciting prospect of growing certain nanowire orientations by selectively tailoring the metal catalyst surface to have specific surface facets. Future studies of epitaxial matching between various nanowire orientations and different surface facets of metal nanoparticles will provide deep insights to the experimentalists to design metal catalyst surfaces for desired growth of specific nanowire orientations.

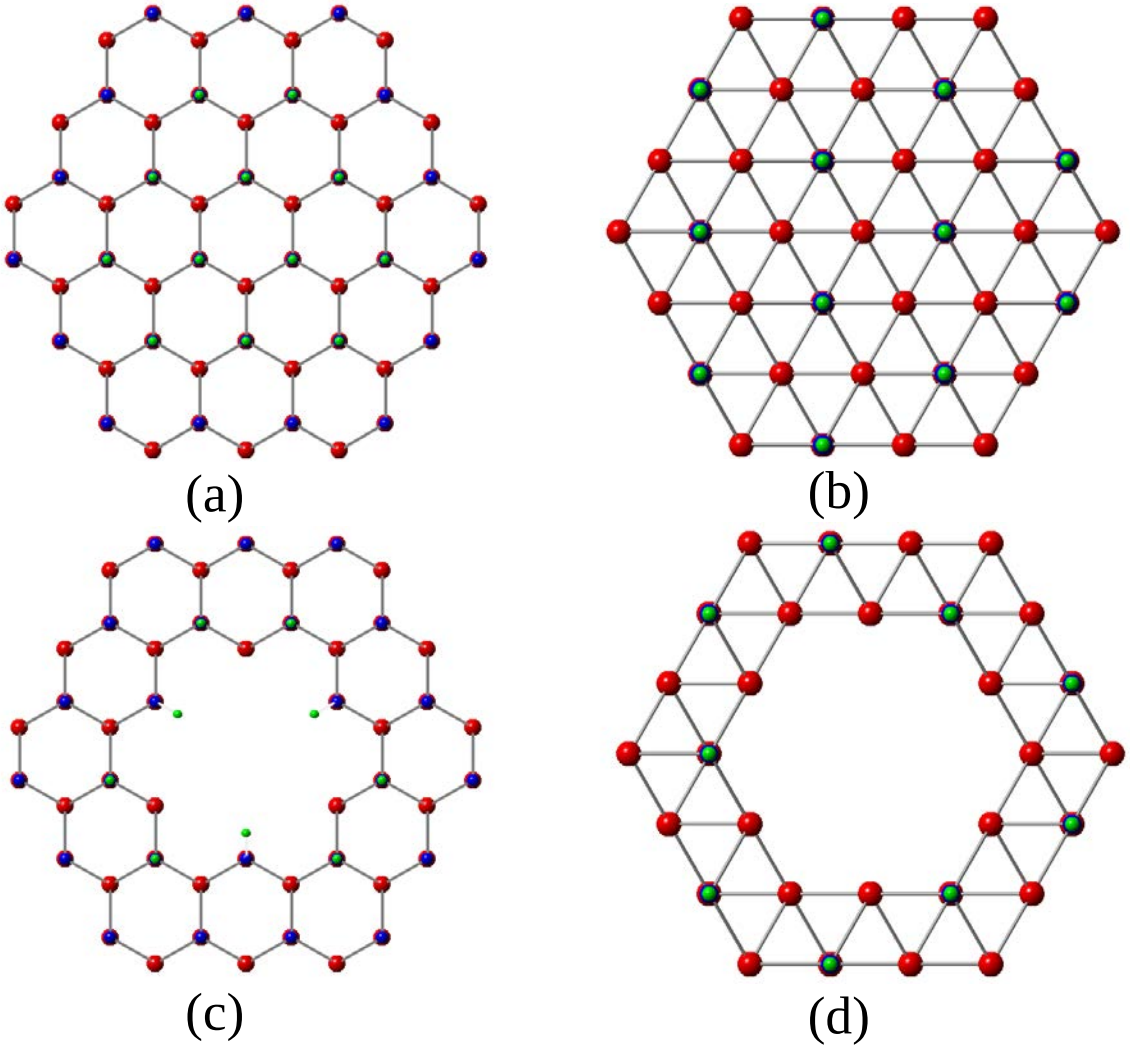

Figure 6.1: Cross-sectional view of H-terminated nanowire and nanotube fragments in the general <111> growth orientation: (a) WZ(0001) nanowire, (b) ZB(111) nanowire, (c) WZ(0001) nanotube and (d) ZB(111) nanotube. Color code of atoms: As (blue), In (red), H (green).

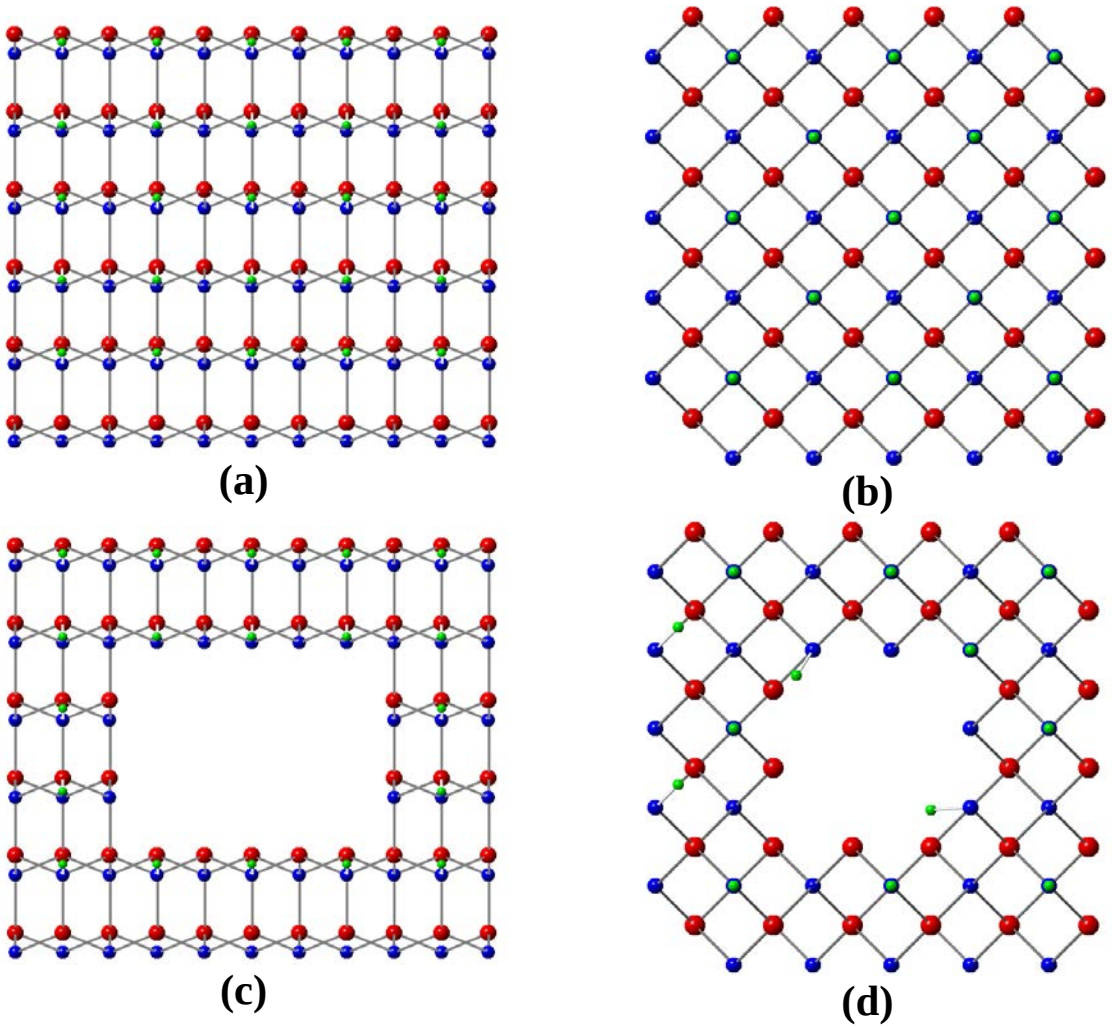

Figure 6.2: Cross-sectional view of H-terminated nanowire and nanotube fragments in the general <100> growth orientation: (a) WZ(10-10) nanowire, (b) ZB(100) nanowire, (c) WZ(10-10) nanotube and (d) ZB(100) nanotube. Color code of atoms: As (blue), In (red), H (green).

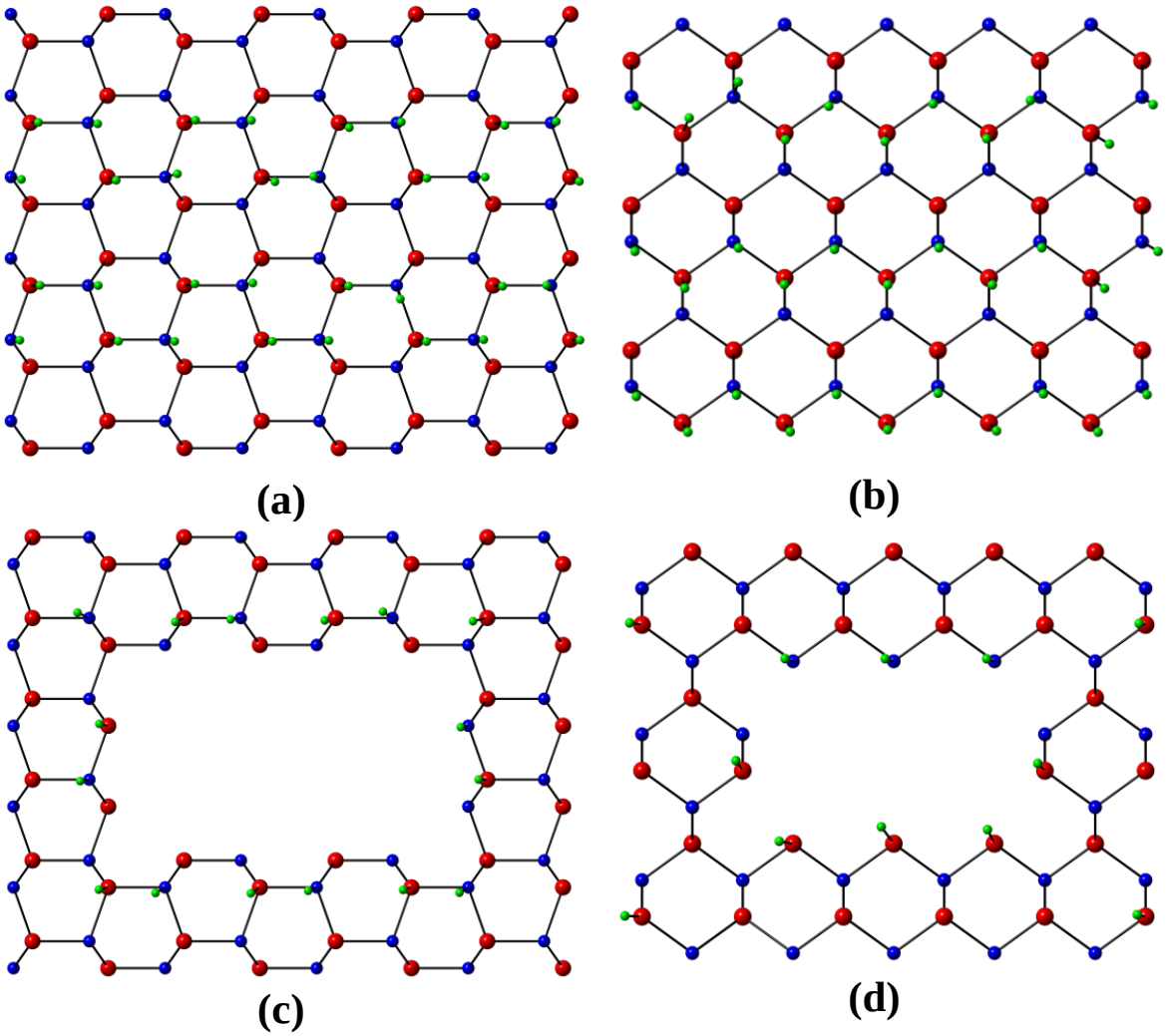

Figure 6.3: Cross-sectional view of H-terminated nanowire and nanotube fragments in the general <110> growth orientation: (a) WZ(11-20) nanowire, (b) ZB(110) nanowire, (c) WZ(11-20) nanotube and (d) ZB(110) nanotube. Color code of atoms: As (blue), In (red), H (green).

Table 6.1: Structural parameters of nanowire and nanotube fragments used in the DFT calculations.

System	Stoichiometry	Areal Shape	No. of Indium edge atoms	Surface fraction of atoms
ZB (111) NW	$As_{49}In_{49}H_{12}$	Hexagonal	12	0.48
ZB (111) NT	$As_{39}In_{39}H_{9}$	Hexagonal	9	1
ZB (100) NW	$As_{66}In_{66}H_{13}$	Square	13	0.29
ZB (100) NT	$As_{60}In_{60}H_{13}$	Square	13	1
ZB (110) NW	$As_{66}In_{66}H_{31}$	Rectangular	28	0.33
ZB (110) NT	$As_{56}In_{56}H_{12}$	Rectangular	22	1
WZ (0001) NW	$As_{54}In_{54}H_{12}$	Hexagonal	27	0.67
WZ (0001) NT	$As_{48}In_{48}H_{9}$	Hexagonal	24	1
WZ (10-10) NW	$As_{66}In_{66}H_{25}$	Rectangular	15	0.32
WZ (10-10) NT	$As_{56}In_{56}H_{19}$	Rectangular	24	1
WZ (11-20) NW	$As_{88}In_{88}H_{32}$	Square	26	0.50
WZ (11-20) NT	$As_{72}In_{72}H_{16}$	Square	22	1

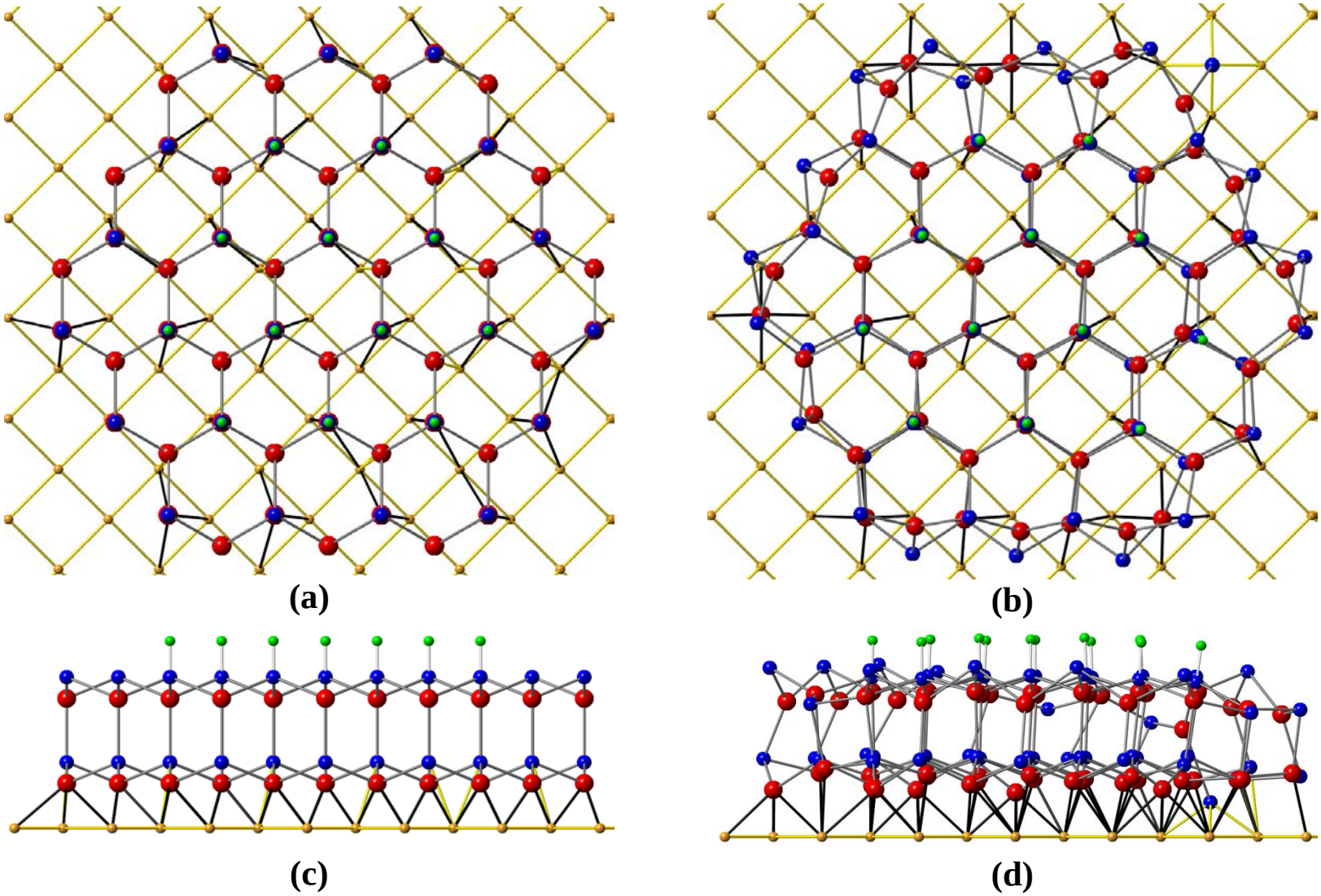

Figure 6.4: WZ(0001) nanowire adsorbed on Au(100) surface. Initial and geometry optimized final configurations: (a,b) Areal cross-sectional view & (c,d) Lateral surface view respectively. Color code of atoms: As (blue), In (red), H (green), Au(yellow).

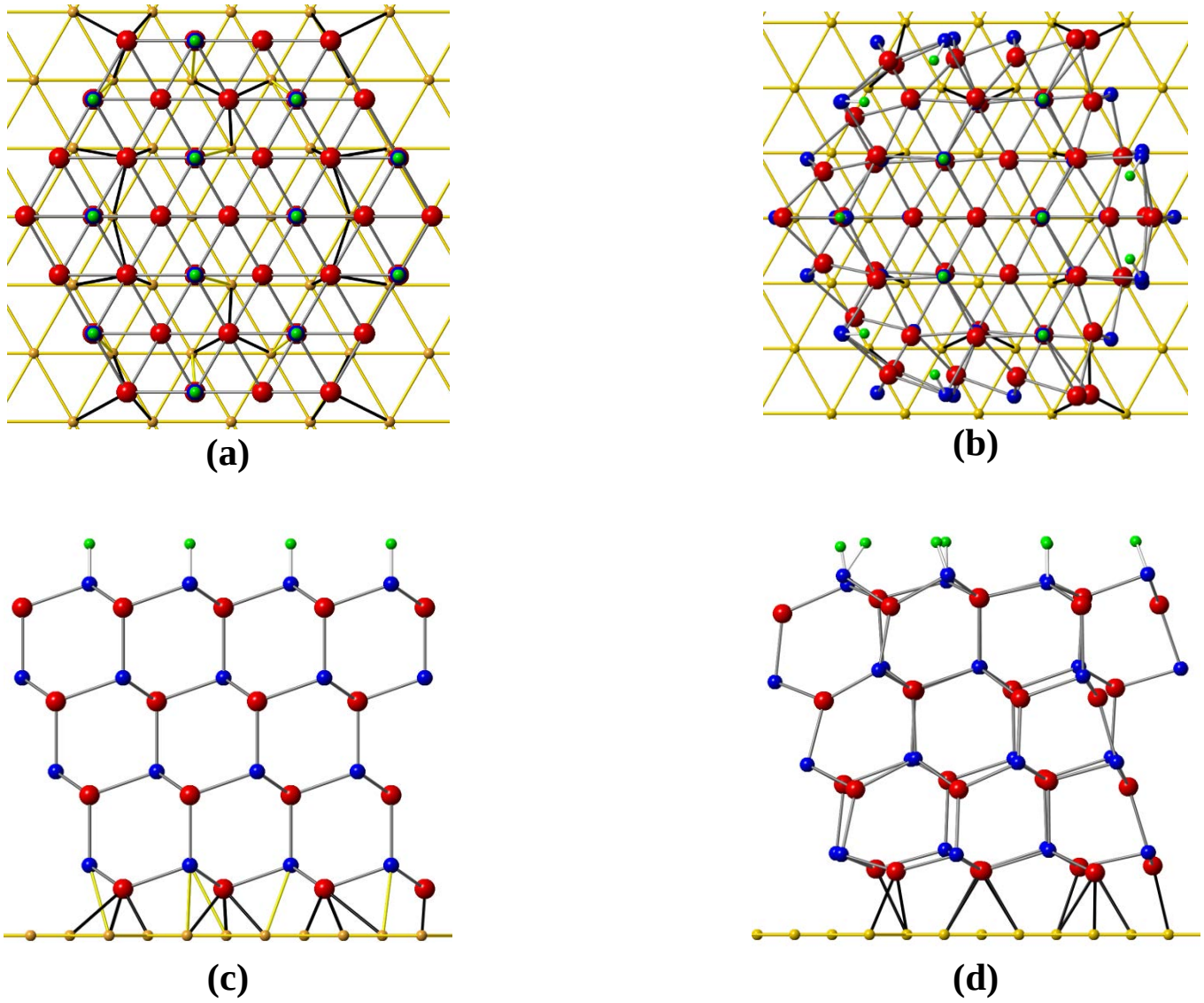

Figure 6.5: ZB(111) nanowire adsorbed on Au(111) surface. Initial and geometry optimized final configurations: (a,b) Areal cross-sectional view & (c,d) Lateral surface view respectively. Color code of atoms: As (blue), In (red), H (green), Au (yellow).

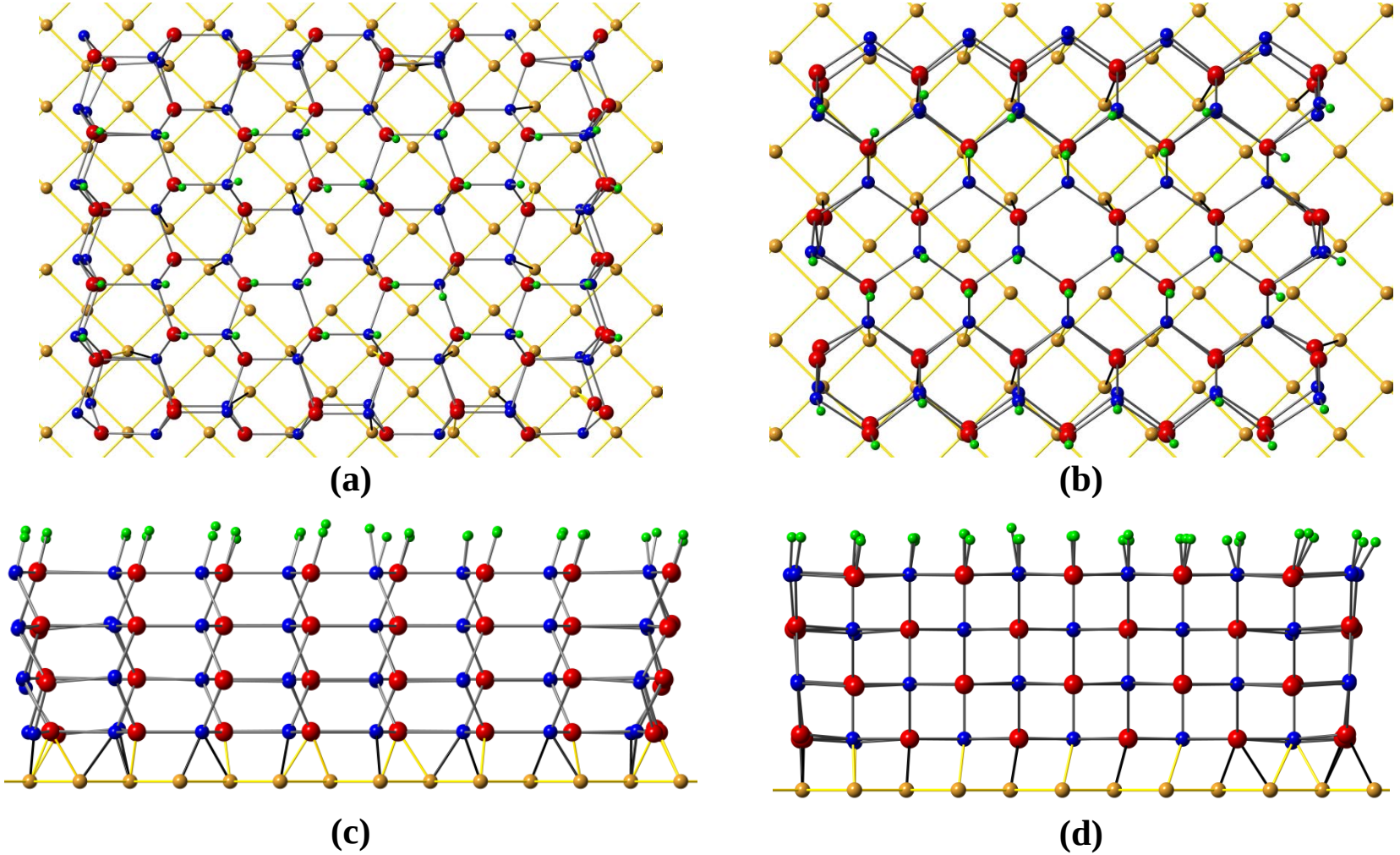

Figure 6.6: Geometry optimized final configurations of WZ(11-20) and ZB(110) nanowire adsorbed on Au(100) surface. Areal cross-sectional view of (a) WZ(11-20) & (b) ZB(110). Lateral surface view of (c) WZ(11-20) & (d) ZB(110). Color code of atoms: As (blue), In (red), H (green), Au(yellow).

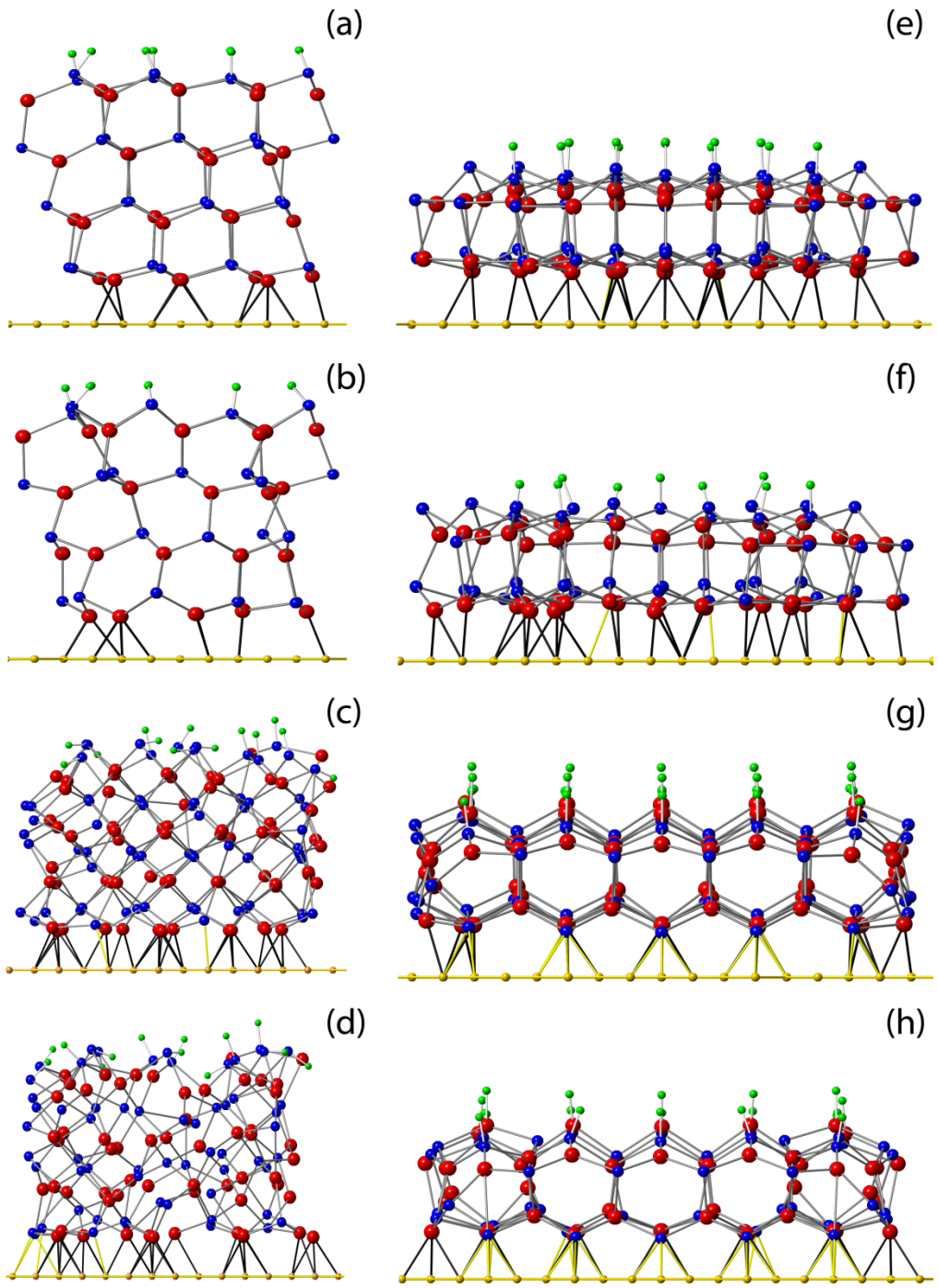

Figure 6.7: Geometry optimized side views of various H-terminated nanowire and nanotube fragments adsorbed on Au(111) surface. (a,b) ZB(111) NW & NT, (c,d) ZB(100) NW & NT, (e,f) WZ (0001)NW &NT and (g,h) WZ(10-10) NW & NT. Color code of atoms: As (blue), In (red), H (green), Au (yellow).

Table 6.2: Binding energies and excess energies for the H-terminated nanowire and nanotube fragments on the Au(111) and Au(100) surfaces.

System	E_b on Au (111) (eV/atom)	E_b on Au (100) (eV/atom)	E_x on Au (111) (eV/atom)	E_x on Au (100) (eV/atom)
ZB (111) NW	-0.068	-0.041	0.065	0.098
ZB (111) NT	-0.049	-0.040	0.136	0.174
ZB (100) NW	-0.057	-0.077	0.092	0.075
ZB (100) NT	-0.087	-0.105	0.120	0.103
ZB (110) NW	-0.062	-0.069	0.085	0.069
ZB (110) NT	-0.081	-0.095	0.117	0.097
WZ (0001) NW	-0.104	-0.093	0.049	0.055
WZ (0001) NT	-0.087	-0.074	0.072	0.080
WZ (10-10) NW	-0.082	-0.092	0.087	0.072
WZ (10-10) NT	-0.097	-0.106	0.110	0.095
WZ (11-20) NW	-0.084	-0.098	0.079	0.061
WZ (11-20) NT	-0.099	-0.108	0.102	0.085

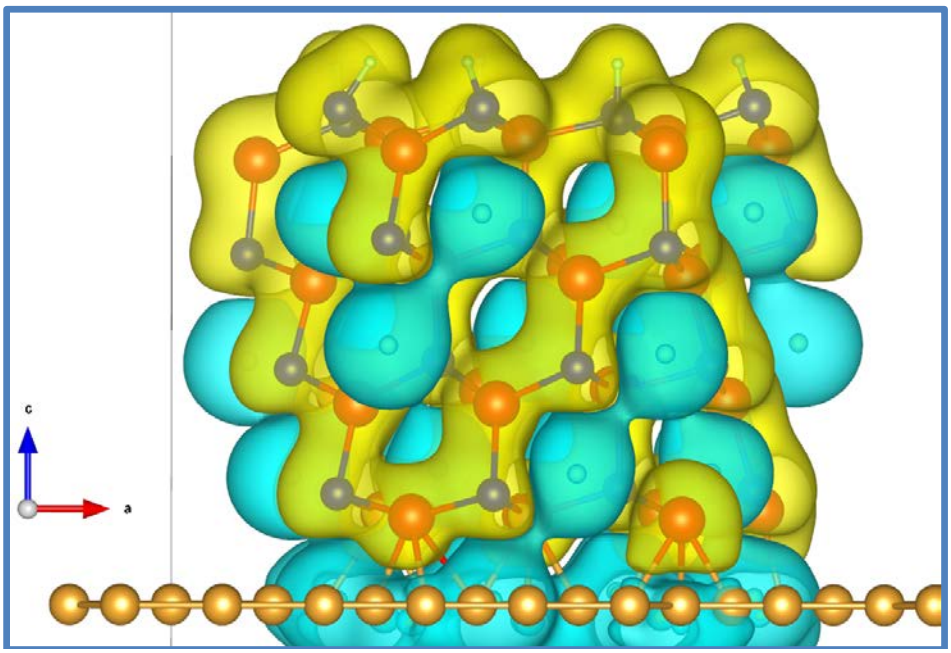

(a)

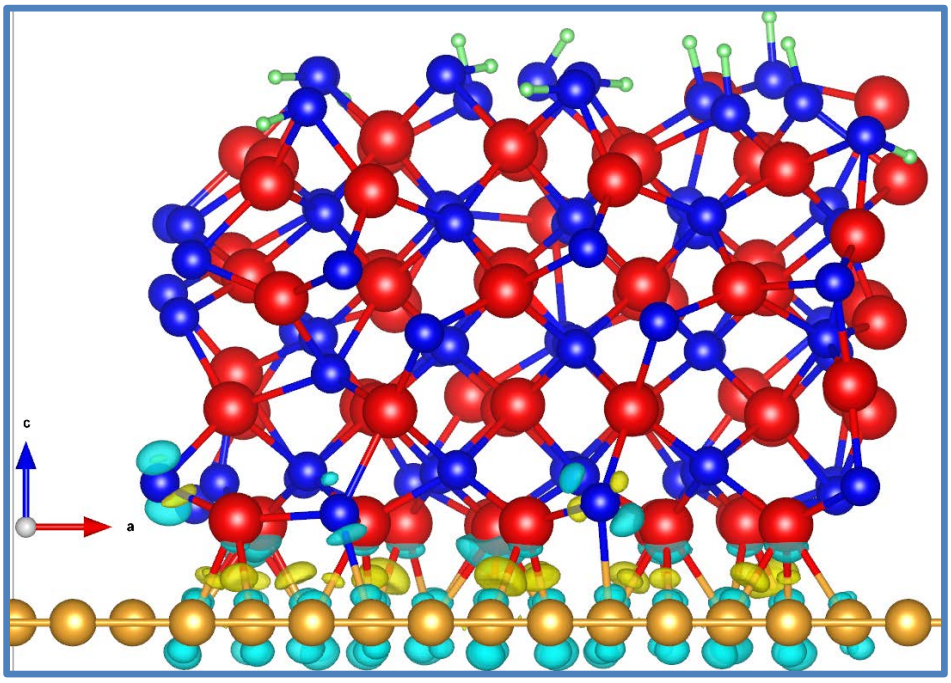

(b)

Figure 6.8: Electron charge difference maps of (a) ZB(111) and (b) ZB(100) nanowire on Au(111) surfaces. Yellow zones are electron charge depletion regions and green zones are electon charge accumulation regions.

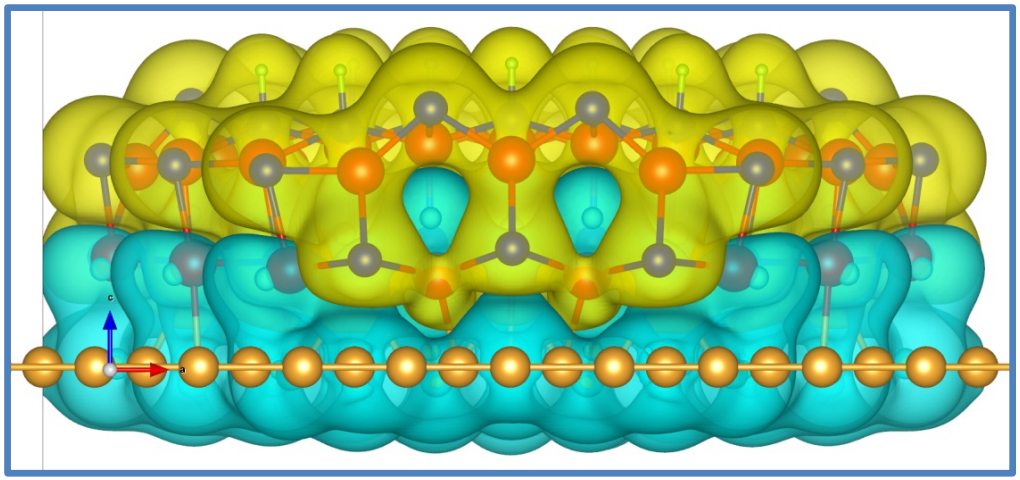

(a)

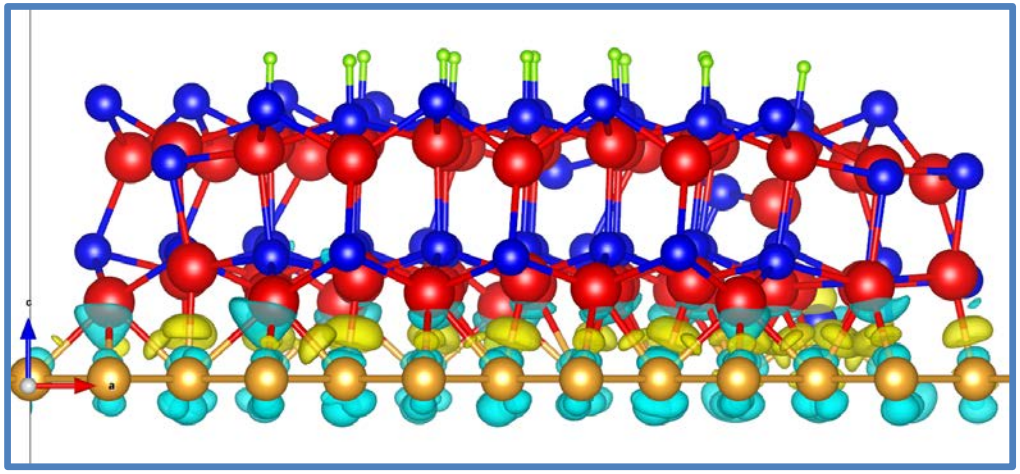

(b)

Figure 6.9: Electron charge difference maps of WZ(0001) nanowires on (a) Au(111) and (b) Au(100) surface. Yellow zones are electron charge depletion regions and green zones are electon charge accumulation regions.

CHAPTER 7: CONCLUSION AND FUTURE RESEARCH DIRECTIONS

In this dissertation, we presented an epitaxial nucleation and growth model in order to study the chiral-selective growth of semiconducting and metallic SWCNTs and to control the growth orientations of InAs nanowires. In this chapter, we want to summarize our results and draw generic conclusions about metal-catalyzed epitaxial growth of these 1D nanomaterials. In addition, we would like to give an outlook for future research directions.

Our collaborators at CWRU have previously demonstrated the growth of SWCNTs with narrow chirality distributions on various compositionally tuned NiFe bimetallic nanoparticles. In support of these experimental observations, we have presented a simplified epitaxial nucleation model where we use a two-dimensional (2D) (111) surface with varying atomic spacing as our model catalyst surface in order to study the nanotube cap nucleation of various chiralities. Our DFT calculations show that chiralities such as (8,4) and (6,5) have an enhanced binding strength on surfaces with an increased metal-metal bond length as in $Ni_{0.27}Fe_{0.73}$ catalysts, while chiralities such as (9,4) and (8,6) are more stable on surfaces corresponding to Ni catalysts, in excellent agreement with experiments. Based on our DFT calculations, we conclude that tuning the composition of the metal nanoparticles changes the average metal-metal bond length in the nanoparticle and that in turn changes the nanotube chirality distribution.

Later, we used this epitaxial nucleation model to explore the chiral enrichment of metallic nanotubes grown on Ni, Cu and Ni_xCu_{1-x} nanoparticles by calculating the binding strengths of various nanotube cap chiralities on these metal catalyst surfaces. In addition, we studied the

nanotube growth on various catalyst surfaces by calculating differences in armchair and zigzag dangling bond energies, relative chemical activity ratios and nanotube growth rates of various nanotube chiralities. Based on the binding strengths of various nanotube chiralities obtained from the DFT calculations, certain armchair and zigzag nanotube caps like (5,5) and (10,0) show higher binding strengths than the chiral caps. The stability of the caps on the various surfaces decreases as Ni > $Ni_{0.5}Cu_{0.5}$ > Cu in accordance with the respective carbon-metal adhesion strengths. Both the relative chemical activity ratios and the nanotube growth rates, obtained from differences in the armchair and zigzag dangling bond energies on various catalyst surfaces, suggest that the Ni_xCu_{1-x} bimetallic nanoparticles with increased bond length or lattice-strained surfaces can be excellent metal catalysts in growing metallic nanotubes preferentially. In particular, the metallic armchair cap (5,5) shows stronger binding with the metal catalyst at the cap nucleation stage and enhanced growth rates during the nanotube elongation stage and, can be selectively grown on pure and lattice-strained Ni-Cu nanoparticles.

Finally, we have studied the epitaxial growth of small fragments of wurtzite (WZ) and zinc blende (ZB) phases of InAs nanowires (NW) and nanotubes (NT) with growth orientations of <111> and <100> on Au(111) and Au(100) surfaces. From our DFT calculations, we observe that the WZ phase is more stable than the ZB phase on any of the Au surface facets because the surface dangling bond energies of the ZB is higher than that of the WZ and makes the small diameter ZB phase more unstable. Again, the NTs are less stable than the NWs due to higher number of surface dangling bonds. Finally, epitaxial relationships are observed between the NW fragments and the faceted Au surfaces based on our energetics and electron charge redistribution calculations. The <111> orientation of the InAs NWs have higher binding strengths and are more stable on the Au(111) than the Au(100) surface while the <100>and <110> orientations are

relatively more stable on the Au(100) surface; though the overall stability of the <111> orientations are higher than the <100> and <110> orientations of the NW. The results suggest that epitaxial growth of InAs NWs on specifically faceted Au nanoparticles can lead to preferential growth of specific orientations of the InAs nanowires.

For future research directions, we would like to state that the epitaxial nucleation model is generic and, can be applied to study the nucleation of various nanotube chiralities on different bimetallic and trimetallic nanoparticles to screen out specific nanotube chiralities. Additionally, the chirality dependent nanotube growth rate proposed by Dumlich *et al.* and as implemented here in the context of growth of metallic nanotubes on Ni-Cu surfaces is applicable for mostly armchair and near-armchair nanotubes. Using geometrical arguments, this growth model can be extended to include the growth rates of zigzag nanotubes so that the growth model becomes more generic. Thereafter, the combination of the epitaxial nucleation model and the more-generic nanotube growth model can be used to selectively screen metal nanocatalysts suitable for chiral-selective growth of any SWCNTs including zigzag nanotubes. In case of the InAs nanowire growth on Au nanoparticles, we would like to point out that we have studied the binding of the nanowire orientations on Au surface facets where the assumption is that the Au metal nanocatalyst remains essentially solid. This is applicable for a vapor-solid-solid (VSS) mechanism. However, for the more commonly observed vapor-liquid-solid (VLS) mechanism, the semiconductor reactant gas dissolves in the Au metal to form an $InAu_2$ alloy as observed in our physical vapor transport based growth of InAs nanowires on shaped nanoparticles grown in colloidal phase. Hence, future studies can be aimed at finding the appropriate surface facets of $InAu_2$ alloy on which the InAs nanowires can grow and then, establish the epitaxial relationship between the nanowire growth orientations and the surface facets of $InAu_2$ alloy. Finally, we

would conclude by saying that in addition to explaining our experimental results, the overall findings in this dissertation work suggests that a potential route to chiral selectivity of SWCNTs or the control of InAs nanowire growth orientations is to design catalysts with specific compositions or faceted surfaces such that there is enhanced epitaxial matching between the metal nanocatalysts and the as-grown 1D nanostructures.

REFERENCES

(1) White, C. T.; Mintmire, J. W.: Fundamental Properties of Single-Wall Carbon Nanotubes. *The Journal of Physical Chemistry B***2004**, *109*, 52-65.

(2) Reich, S.; Li, L.; Robertson, J.: Epitaxial growth of carbon caps on Ni for chiral selectivity. *Physica Status Solidi (B)***2006**, *243*, 3494-3499.

(3) Saito, R.; Fujita, M.; Dresselhaus, G.; Dresselhaus, M. S.: Electronic structure of graphene tubules based on C_{60}. *Physical Review B***1992**, *46*, 1804-1811.

(4) Hamada, N.; Sawada, S.-i.; Oshiyama, A.: New one-dimensional conductors: Graphitic microtubules. *Physical Review Letters***1992**, *68*, 1579-1581.

(5) Kroto, H. W.: Space, stars, C_{60}, and soot. *Science***1988**, *242*, 1139-1145.

(6) Brinkmann, G.: A census of nanotube caps. *Chemical Physics Letters***1999**, *315*, 335-347.

(7) Reich, S.; Li, L.; Robertson, J.: Structure and formation energy of carbon nanotube caps. *Physical Review B***2005**, *72*, 1-8.

(8) Chiang, W.-H.; Sankaran, R. M.: Linking catalyst composition to chirality distributions of as-grown single-walled carbon nanotubes by tuning Ni(x)Fe(1-x) nanoparticles. *Nature Materials***2009**, *8*, 882-6.

(9) Seidel, R.; Duesberg, G. S.; Unger, E.; Graham, A. P.; Liebau, M.; Kreupl, F.: Chemical Vapor Deposition Growth of Single-Walled Carbon Nanotubes at 600 °C and a Simple Growth Model. *The Journal of Physical Chemistry B***2004**, *108*, 1888-1893.

(10) Smalley, R. E.; Li, Y.; Moore, V. C.; Price, B. K.; Colorado, R.; Schmidt, H. K.; Hauge, R. H.; Barron, A. R.; Tour, J. M.: Single Wall Carbon Nanotube Amplification: En Route to a Type-Specific Growth Mechanism. *Journal of the American Chemical Society***2006**, *128*, 15824-15829.

(11) Ding, L.; Tselev, A.; Wang, J.; Yuan, D.; Chu, H.; McNicholas, T. P.; Li, Y.; Liu, J.: Selective growth of well-aligned semiconducting single-walled carbon nanotubes. *Nano Letters***2009**, *9*, 800-5.

(12) Gavillet, J.; Loiseau, A.; Journet, C.; Willaime, F.; Ducastelle, F.; Charlier, J. C.: Root-Growth Mechanism for Single-Wall Carbon Nanotubes. *Physical Review Letters***2001**, *87*, 275504.

(13) Ding, F.; Larsson, P.; Larsson, J. A.; Ahuja, R.; Duan, H.; RosÃ©n, A.; Bolton, K.: The importance of strong carbon-metal adhesion for catalytic nucleation of single-walled carbon nanotubes. *Nano letters***2008**, *8*, 463-8.

(14) Raty, J.-Y.; Gygi, F.; Galli, G.: Growth of Carbon Nanotubes on Metal Nanoparticles: A Microscopic Mechanism from Ab Initio Molecular Dynamics Simulations. *Physical Review Letters***2005**, *95*, 096103.

(15) Wagner, R. S.; Ellis, W. C.: Vapor-liquid-solid mechanism of single crystal growth *Applied Physics Letters***1964**, *4*, 89-90.

(16) Arnold, M. S.; Green, A. A.; Hulvat, J. F.; Stupp, S. I.; Hersam, M. C.: Sorting carbon nanotubes by electronic structure using density differentiation. *Nat Nano***2006**, *1*, 60-65.

(17) Iijima, S.: Helical microtubules of graphitic carbon. *Nature***1991**, *354*, 56-58.

(18) Ding, F.; Harutyunyan, A. R.; Yakobson, B. I.: Dislocation theory of chirality-controlled nanotube growth. *Proceedings of the National Academy of Sciences of the United States of America***2009**, *106*, 2506-9.

(19) Han, Z. J.; Ostrikov, K.: Uniform, Dense Arrays of Vertically Aligned, Large-Diameter Single-Walled Carbon Nanotubes. *Journal of the American Chemical Society***2012**, *134*, 6018-6024.

(20) Bower, C.; Zhou, O.; Zhu, W.; Werder, D. J.; Jin, S.: Nucleation and growth of carbon nanotubes by microwave plasma chemical vapor deposition. *Applied Physics Letters***2000**, *77*, 2767-2769.

(21) Hofmann, S.; Sharma, R.; Ducati, C.; Du, G.; Mattevi, C.; Cepek, C.; Cantoro, M.; Pisana, S.; Parvez, A.; Cervantes-Sodi, F.; Ferrari, A. C.; Dunin-Borkowski, R.; Lizzit, S.; Petaccia, L.; Goldoni, A.; Robertson, J.: In situ Observations of Catalyst Dynamics during Surface-Bound Carbon Nanotube Nucleation. *Nano Letters***2007**, *7*, 602-608.

(22) Amara, H.; Bichara, C.; Ducastelle, F.: Understanding the Nucleation Mechanisms of Carbon Nanotubes in Catalytic Chemical Vapor Deposition. *Physical Review Letters***2008**, *100*, 1-4.

(23) Amama, P. B.; Pint, C. L.; McJilton, L.; Kim, S. M.; Stach, E. A.; Murray, P. T.; Hauge, R. H.; Maruyama, B.: Role of Water in Super Growth of Single-Walled Carbon Nanotube Carpets. *Nano Letters***2008**, *9*, 44-49.

(24) Hofmann, S.; Csányi, G.; Ferrari, A. C.; Payne, M. C.; Robertson, J.: Surface Diffusion: The Low Activation Energy Path for Nanotube Growth. *Physical Review Letters***2005**, *95*, 036101.

(25) Neyts, E. C.; Shibuta, Y.; van Duin, A. C. T.; Bogaerts, A.: Catalyzed Growth of Carbon Nanotube with Definable Chirality by Hybrid Molecular Dynamicsâ^'Force Biased Monte Carlo Simulations. *ACS Nano***2010**, *4*, 6665-6672.

(26) Ohta, Y.; Okamoto, Y.; Page, A. J.; Irle, S.; Morokuma, K.: Quantum Chemical Molecular Dynamics Simulation of Single-Walled Carbon Nanotube Cap Nucleation on an Iron Particle. *ACS nano***2009**, *3*, 3413-3420.

(27) Artyukhov, V. I.; Liu, Y.; Yakobson, B. I.: Equilibrium at the edge and atomistic mechanisms of graphene growth. *Proceedings of the National Academy of Sciences of the United States of America***2012**, *109*, 15136-15140.

(28) Jose; X; Yacaman, M.; Miki; Yoshida, M.; Rendon, L.; Santiesteban, J. G.: Catalytic growth of carbon microtubules with fullerene structure. *Applied Physics Letters***1993**, *62*, 657-659.

(29) Harutyunyan, A. R.; Chen, G.; Paronyan, T. M.; Pigos, E. M.; Kuznetsov, O. a.; Hewaparakrama, K.; Kim, S. M.; Zakharov, D.; Stach, E. a.; Sumanasekera, G. U.: Preferential growth of single-walled carbon nanotubes with metallic conductivity. *Science***2009**, *326*, 116-20.

(30) He, M.; Liu, B.; Chernov, A. I.; Obraztsova, E. D.; Kauppi, I.; Jiang, H.; Anoshkin, I.; Cavalca, F.; Hansen, T. W.; Wagner, J. B.; Nasibulin, A. G.; Kauppinen, E. I.; Linnekoski, J.; Niemela, M.; Lehtonen, J.: Growth Mechanism of Single-Walled Carbon Nanotubes on Iron− Copper Catalyst and Chirality Studies by Electron Diffraction. *Chemistry of Materials***2012**.

(31) Lolli, G.; Zhang, L.; Balzano, L.; Sakulchaicharoen, N.; Tan, Y.; Resasco, D. E.: Tailoring (n,m) Structure of Single-Walled Carbon Nanotubes by Modifying Reaction Conditions and the Nature of the Support of CoMo Catalysts. *The Journal of Physical Chemistry B***2006**, *110*, 2108-2115.

(32) Reich, S.; Li, L.; Robertson, J.: Control the chirality of carbon nanotubes by epitaxial growth. *Chemical Physics Letters***2006**, *421*, 469-472.

(33) Zhu, W.; Borjesson, A.; Bolton, K.: DFT and tight binding Monte Carlo calculations related to single-walled carbon nanotube nucleation and growth. *Carbon***2010**, *48*, 470-478.

(34) Gómez-Gualdrón, D. A.; Zhao, J.; Balbuena, P. B.: Nanocatalyst structure as a template to define chirality of nascent single-walled carbon nanotubes. *The Journal of Chemical Physics***2011**, *134*, 252-258.

(35) Borjesson, A.; Zhu, W.; Amara, H.; Bichara, C.; Bolton, K.: Computational studies of metal-carbon nanotube interfaces for regrowth and electronic transport. *Nano letters***2009**, *9*, 1117-20.

(36) Fan, X.; Buczko, R.; Puretzky, A.; Geohegan, D.; Howe, J.; Pantelides, S.; Pennycook, S.: Nucleation of Single-Walled Carbon Nanotubes. *Physical Review Letters***2003**, *90*, 1-4.

(37) Dumlich, H.; Reich, S.: Chirality-dependent growth rate of carbon nanotubes: A theoretical study. *Physical Review B***2010**, *82*, 1-5.

(38) Susi, T.; Zhu, Z.; Ruiz-Soria, G.; Arenal, R.; Ayala, P.; Nasibulin, A. G.; Lin, H.; Jiang, H.; Stephan, O.; Pichler, T.; Loiseau, A.; Kauppinen, E. I.: Nitrogen-doped SWCNT synthesis using ammonia and carbon monoxide. *Physica Status Solidi (B)***2010**, *247*, 2726-2729.

(39) Yazyev, O.; Pasquarello, A.: Effect of Metal Elements in Catalytic Growth of Carbon Nanotubes. *Physical Review Letters***2008**, *100*, 156102-156102.

(40) Rao, R.; Liptak, D.; Cherukuri, T.; Yakobson, B. I.; Maruyama, B.: In situ evidence for chirality-dependent growth rates of individual carbon nanotubes. *Nat Mater***2012**, *advance online publication*.

(41) Liu, Y.; Dobrinsky, A.; Yakobson, B. I.: Graphene Edge from Armchair to Zigzag: The Origins of Nanotube Chirality? *Physical Review Letters***2010**, *105*, 235502.

(42) Diarra, M.; Zappelli, A.; Amara, H.; Ducastelle, F.; Bichara, C.: Importance of Carbon Solubility and Wetting Properties of Nickel Nanoparticles for Single Wall Nanotube Growth. *Physical Review Letters***2012**, *109*, 185501.

(43) Yoshida, H.; Takeda, S.; Uchiyama, T.; Kohno, H.; Homma, Y.: Atomic-Scale In-situ Observation of Carbon Nanotube Growth from Solid State Iron Carbide Nanoparticles. *Nano Letters***2008**, *8*, 2082-2086.

(44) Gomez-Gualdron, D. A.; McKenzie, G. D.; Alvarado, J. F. J.; Balbuena, P. B.: Dynamic Evolution of Supported Metal Nanocatalyst/Carbon Structure during Single-Walled Carbon Nanotube Growth. *ACS nano*, *6*, 720-735.

(45) Neyts, E. C.; van Duin, A. C. T.; Bogaerts, A.: Changing Chirality during Single-Walled Carbon Nanotube Growth: A Reactive Molecular Dynamics/Monte Carlo Study. *Journal of the American Chemical Society*, *133*, 17225-17231.

(46) Wang, Q.; Ng, M.-F.; Yang, S.-W.; Yang, Y.; Chen, Y.: The Mechanism of Single-Walled Carbon Nanotube Growth and Chirality Selection Induced by Carbon Atom and Dimer Addition. *ACS nano***2010**, *4*, 939-946.

(47) Li, X.; Tu, X.; Zaric, S.; Welsher, K.; Seo, W. S.; Zhao, W.; Dai, H.: Selective Synthesis Combined with Chemical Separation of Single-Walled Carbon Nanotubes for Chirality Selection. *Journal of the American Chemical Society***2007**, *129*, 15770-15771.

(48) Liu, H.; Nishide, D.; Tanaka, T.; Kataura, H.: Large-scale single-chirality separation of single-wall carbon nanotubes by simple gel chromatography. *Nat Commun***2011**, *2*, 309.

(49) Odom, T. W.; Huang, J.-L.; Kim, P.; Lieber, C. M.: Atomic structure and electronic properties of single-walled carbon nanotubes. *Nature***1998**, *391*, 62-64.

(50) Duan, X.; Huang, Y.; Cui, Y.; Wang, J.; Lieber, C. M.: Indium phosphide nanowires as building blocks for nanoscale electronic and optoelectronic devices. *Nature***2001**, *409*, 66-69.

(51) Cui, Y.; Wei, Q.; Park, H.; Lieber, C. M.: Nanowire Nanosensors for Highly Sensitive and Selective Detection of Biological and Chemical Species. *Science***2001**, *293*, 1289-1292.

(52) Tian, B.; Zheng, X.; Kempa, T. J.; Fang, Y.; Yu, N.; Yu, G.; Huang, J.; Lieber, C. M.: Coaxial silicon nanowires as solar cells and nanoelectronic power sources. *Nature***2007**, *449*, 885-889.

(53) Dayeh, S. A.; Aplin, D. P. R.; Zhou, X.; Yu, P. K. L.; Yu, E. T.; Wang, D.: High Electron Mobility InAs Nanowire Field-Effect Transistors. *Small***2007**, *3*, 326-332.

(54) Masumoto, Y.; Hirata, Y.; Mohan, P.; Motohisa, J.; Fukui, T.: Polarized photoluminescence from single wurtzite InP/InAs/InP core-multishell nanowires. *Applied Physics Letters***2011**, *98*, 211902-3.

(55) Hansen, A. E.; Bjork, M. T.; Fasth, C.; Thelander, C.; Samuelson, L.: Spin relaxation in InAs nanowires studied by tunable weak antilocalization. *Physical Review B***2005**, *71*, 205328.

(56) Morales, A. M.; Lieber, C. M.: A Laser Ablation Method for the Synthesis of Crystalline Semiconductor Nanowires. *Science***1998**, *279*, 208-211.

(57) Holmes, J. D.; Johnston, K. P.; Doty, R. C.; Korgel, B. A.: Control of Thickness and Orientation of Solution-Grown Silicon Nanowires. *Science***2000**, *287*, 1471-1473.

(58) Hiruma, K.; Murakoshi, H.; Yazawa, M.; Katsuyama, T.: Self-organized growth of GaAsInAs heterostructure nanocylinders by organometallic vapor phase epitaxy. *Journal of Crystal Growth***1996**, *163*, 226-231.

(59) Gudiksen, M. S.; Lauhon, L. J.; Wang, J.; Smith, D. C.; Lieber, C. M.: Growth of nanowire superlattice structures for nanoscale photonics and electronics. *Nature***2002**, *415*, 617-620.

(60) Wu, Y.; Fan, R.; Yang, P.: Block-by-Block Growth of Single-Crystalline Si/SiGe Superlattice Nanowires. *Nano Letters***2002**, *2*, 83-86.

(61) Qian, F.; Li, Y.; Gradečak, S.; Wang, D.; Barrelet, C. J.; Lieber, C. M.: Gallium Nitride-Based Nanowire Radial Heterostructures for Nanophotonics. *Nano Letters***2004**, *4*, 1975-1979.

(62) Lauhon, L. J.; Gudiksen, M. S.; Wang, D.; Lieber, C. M.: Epitaxial core-shell and core-multishell nanowire heterostructures. *Nature***2002**, *420*, 57-61.

(63) Haraguchi, K.; Katsuyama, T.; Hiruma, K.; Ogawa, K.: GaAs p-n junction formed in quantum wire crystals. *Applied Physics Letters***1992**, *60*, 745-747.

(64) Ertekin, E.; Greaney, P. A.; Chrzan, D. C.; Sands, T. D.: Equilibrium limits of coherency in strained nanowire heterostructures. *Journal of Applied Physics***2005**, *97*, -.

(65) Mårtensson, T.; Svensson, C. P. T.; Wacaser, B. A.; Larsson, M. W.; Seifert, W.; Deppert, K.; Gustafsson, A.; Wallenberg, L. R.; Samuelson, L.: Epitaxial III−V Nanowires on Silicon. *Nano Letters***2004**, *4*, 1987-1990.

(66) Bryllert, T.; Wernersson, L. E.; Froberg, L. E.; Samuelson, L.: Vertical high-mobility wrap-gated InAs nanowire transistor. *Electron Device Letters, IEEE***2006**, *27*, 323-325.

(67) Fortuna, S. A.; Xiuling, L.: GaAs MESFET With a High-Mobility Self-Assembled Planar Nanowire Channel. *Electron Device Letters, IEEE***2009**, *30*, 593-595.

(68) Huang, M. H.; Mao, S.; Feick, H.; Yan, H.; Wu, Y.; Kind, H.; Weber, E.; Russo, R.; Yang, P.: Room-Temperature Ultraviolet Nanowire Nanolasers. *Science***2001**, *292*, 1897-1899.

(69) Qian, F.; Gradečak, S.; Li, Y.; Wen, C.-Y.; Lieber, C. M.: Core/Multishell Nanowire Heterostructures as Multicolor, High-Efficiency Light-Emitting Diodes. *Nano Letters***2005**, *5*, 2287-2291.

(70) Pettersson, H.; Trägårdh, J.; Persson, A. I.; Landin, L.; Hessman, D.; Samuelson, L.: Infrared Photodetectors in Heterostructure Nanowires. *Nano Letters***2006**, *6*, 229-232.

(71) Kelzenberg, M. D.; Turner-Evans, D. B.; Kayes, B. M.; Filler, M. A.; Putnam, M. C.; Lewis, N. S.; Atwater, H. A.: Photovoltaic Measurements in Single-Nanowire Silicon Solar Cells. *Nano Letters***2008**, *8*, 710-714.

(72) Mårtensson, T.; Wagner, J. B.; Hilner, E.; Mikkelsen, A.; Thelander, C.; Stangl, J.; Ohlsson, B. J.; Gustafsson, A.; Lundgren, E.; Samuelson, L.; Seifert, W.: Epitaxial Growth of Indium Arsenide Nanowires on Silicon Using Nucleation Templates Formed by Self-Assembled Organic Coatings. *Advanced Materials***2007**, *19*, 1801-1806.

(73) Braun, W.; Kaganer, V. M.; Trampert, A.; Schönherr, H.-P.; Gong, Q.; Nötzel, R.; Däweritz, L.; Ploog, K. H.: Diffusion and incorporation: shape evolution during overgrowth on structured substrates. *Journal of Crystal Growth***2001**, *227–228*, 51-55.

(74) Hiruma, K.; Yazawa, M.; Katsuyama, T.; Ogawa, K.; Haraguchi, K.; Koguchi, M.; Kakibayashi, H.: Growth and optical properties of nanometer-scale GaAs and InAs whiskers. *Journal of Applied Physics***1995**, *77*, 447-462.

(75) Gradečak, S.; Qian, F.; Li, Y.; Park, H.-G.; Lieber, C. M.: GaN nanowire lasers with low lasing thresholds. *Applied Physics Letters***2005**, *87*, -.

(76) Duan, X.; Lieber, C. M.: Laser-Assisted Catalytic Growth of Single Crystal GaN Nanowires. *Journal of the American Chemical Society***1999**, *122*, 188-189.

(77) Chen, R.-S.; Wang, S.-W.; Lan, Z.-H.; Tsai, J. T.-H.; Wu, C.-T.; Chen, L.-C.; Chen, K.-H.; Huang, Y.-S.; Chen, C.-C.: On-Chip Fabrication of Well-Aligned and Contact-Barrier-Free GaN Nanobridge Devices with Ultrahigh Photocurrent Responsivity. *Small***2008**, *4*, 925-929.

(78) Kuykendall, T.; Pauzauskie, P. J.; Zhang, Y.; Goldberger, J.; Sirbuly, D.; Denlinger, J.; Yang, P.: Crystallographic alignment of high-density gallium nitride nanowire arrays. *Nat Mater***2004**, *3*, 524-528.

(79) Koguchi, M.; Kakibayashi, H.; Yazawa, M.; Hiruma, K.; Katsuyama, T.: *Crystal Structure Change of GaAs and InAs Whiskers from Zinc-Blende to Wurtzite Type*.

(80) Tsivion, D.; Schvartzman, M.; Popovitz-Biro, R.; Joselevich, E.: Guided Growth of Horizontal ZnO Nanowires with Controlled Orientations on Flat and Faceted Sapphire Surfaces. *ACS Nano***2012**, *6*, 6433-6445.

(81) Tsivion, D.; Schvartzman, M.; Popovitz-Biro, R.; von Huth, P.; Joselevich, E.: Guided Growth of Millimeter-Long Horizontal Nanowires with Controlled Orientations. *Science***2011**, *333*, 1003-1007.

(82) Han, N.; Hui, A. T.; Wang, F.; Hou, J. J.; Xiu, F.; Hung, T.; Ho, J. C.: Crystal phase and growth orientation dependence of GaAs nanowires on NixGay seeds via vapor-solid-solid mechanism. *Applied Physics Letters***2011**, *99*, -.

(83) Lin, P. A.; Liang, D.; Reeves, S.; Gao, X. P. A.; Sankaran, R. M.: Shape-Controlled Au Particles for InAs Nanowire Growth. *Nano Letters***2011**, *12*, 315-320.

(84) Fortuna, S. A.; Li, X.: Metal-catalyzed semicondutor nanowires: a review on the control of growth directions. *Semicond. Sci. Technol.***2010**, *25*, 024005.

(85) Cui, Y.; Lauhon, L. J.; Gudiksen, M. S.; Wang, J.; Lieber, C. M.: Diameter-controlled synthesis of single-crystal silicon nanowires. *Applied Physics Letters***2001**, *78*, 2214-2216.

(86) Schmidt, V.; Senz, S.; Gösele, U.: Diameter-Dependent Growth Direction of Epitaxial Silicon Nanowires. *Nano Letters***2005**, *5*, 931-935.

(87) Wu, Y.; Cui, Y.; Huynh, L.; Barrelet, C. J.; Bell, D. C.; Lieber, C. M.: Controlled Growth and Structures of Molecular-Scale Silicon Nanowires. *Nano Letters***2004**, *4*, 433-436.

(88) Lugstein, A.; Steinmair, M.; Hyun, Y. J.; Hauer, G.; Pongratz, P.; Bertagnolli, E.: Pressure-Induced Orientation Control of the Growth of Epitaxial Silicon Nanowires. *Nano Letters***2008**, *8*, 2310-2314.

(89) Li, C. P.; Lee, C. S.; Ma, X. L.; Wang, N.; Zhang, R. Q.; Lee, S. T.: Growth Direction and Cross-Sectional Study of Silicon Nanowires. *Advanced Materials***2003**, *15*, 607-609.

(90) Hanrath, T.; Korgel, B. A.: Crystallography and Surface Faceting of Germanium Nanowires. *Small***2005**, *1*, 717-721.

(91) Mikkelsen, A.; Skold, N.; Ouattara, L.; Lundgren, E.: Nanowire growth and dopants studied by cross-sectional scanning tunneling microscopy. *Nanotechnology***2006**, *17*, S362-S368.

(92) Fortuna, S. A.; Wen, J.; Chun, I. S.; Li, X.: Planar GaAs Nanowires on GaAs (100) Substrates: Self-Aligned, Nearly Twin-Defect Free, and Transfer-Printable. *Nano Letters***2008**, *8*, 4421-4427.

(93) Ghosh, S. C.; Kruse, P.; LaPierre, R. R.: The effect of GaAs (100) surface preparation on the growth of nanowires. *Nanotechnology***2009**, *20*, 115602.

(94) Wu, Z. H.; Mei, X.; Kim, D.; Blumin, M.; Ruda, H. E.; Liu, J. Q.; Kavanagh, K. L.: Growth, branching, and kinking of molecular-beam epitaxial 〈110〉 GaAs nanowires. *Applied Physics Letters***2003**, *83*, 3368-3370.

(95) Givargizov, E. I.: Fundamental aspects of VLS growth. *Journal of Crystal Growth***1975**, *31*, 20-30.

(96) Soo-Ghang, I.; Jong-In, S.; Young-Hun, K.; Yong Lee, J.; Il-Ho, A.: Growth of GaAs Nanowires on Si Substrates Using a Molecular Beam Epitaxy. *Nanotechnology, IEEE Transactions on***2007**, *6*, 384-389.

(97) Wacaser, B. A.; Deppert, K.; Karlsson, L. S.; Samuelson, L.; Seifert, W.: Growth and characterization of defect free GaAs nanowires. *Journal of Crystal Growth***2006**, *287*, 504-508.

(98) Mattila, M.; Hakkarainen, T.; Jiang, H.; Kauppinen, E. I.; Lipsanen, H.: Effect of substrate orientation on the catalyst-free growth of InP nanowires. *Nanotechnology***2007**, *18*, 155301-.

(99) Krishnamachari, U.; Borgstrom, M.; Ohlsson, B. J.; Panev, N.; Samuelson, L.; Seifert, W.; Larsson, M. W.; Wallenberg, L. R.: Defect-free InP nanowires grown in [001] direction on InP (001). *Applied Physics Letters***2004**, *85*, 2077-2079.

(100) Seifert, W.; Borgström, M.; Deppert, K.; Dick, K. A.; Johansson, J.; Larsson, M. W.; Mårtensson, T.; Sköld, N.; Patrik T. Svensson, C.; Wacaser, B. A.; Reine Wallenberg, L.; Samuelson, L.: Growth of one-dimensional nanostructures in MOVPE. *Journal of Crystal Growth***2004**, *272*, 211-220.

(101) Zhang, X.; Zou, J.; Paladugu, M.; Guo, Y.; Wang, Y.; Kim, Y.; Joyce, H. J.; Gao, Q.; Tan, H. H.; Jagadish, C.: Evolution of Epitaxial InAs Nanowires on GaAs (111)B. *Small***2009**, *5*, 366-369.

(102) Huang, Y.; Duan, X.; Cui, Y.; Lieber, C. M.: Gallium Nitride Nanowire Nanodevices. *Nano Letters***2002**, *2*, 101-104.

(103) Yang, P.; Yan, H.; Mao, S.; Russo, R.; Johnson, J.; Saykally, R.; Morris, N.; Pham, J.; He, R.; Choi, H. J.: Controlled Growth of ZnO Nanowires and Their Optical Properties. *Advanced Functional Materials***2002**, *12*, 323-331.

(104) Nikoobakht, B.; Michaels, C. A.; Stranick, S. J.; Vaudin, M. D.: Horizontal growth and in situ assembly of oriented zinc oxide nanowires. *Applied Physics Letters***2004**, *85*, 3244-3246.

(105) Johnson, J. C.; Choi, H.-J.; Knutsen, K. P.; Schaller, R. D.; Yang, P.; Saykally, R. J.: Single gallium nitride nanowire lasers. *Nat Mater***2002**, *1*, 106-110.

(106) Chen, C.-C.; Yeh, C.-C.; Chen, C.-H.; Yu, M.-Y.; Liu, H.-L.; Wu, J.-J.; Chen, K.-H.; Chen, L.-C.; Peng, J.-Y.; Chen, Y.-F.: Catalytic Growth and Characterization of Gallium Nitride Nanowires. *Journal of the American Chemical Society***2001**, *123*, 2791-2798.

(107) Li, Q.; Creighton, J. R.; Wang, G. T.: The role of collisions in the aligned growth of vertical nanowires. *Journal of Crystal Growth***2008**, *310*, 3706-3709.

(108) Kuykendall, T.; Pauzauskie, P.; Lee, S.; Zhang, Y.; Goldberger, J.; Yang, P.: Metalorganic Chemical Vapor Deposition Route to GaN Nanowires with Triangular Cross Sections. *Nano Letters***2003**, *3*, 1063-1066.

(109) Kohanoff, J.: *Electronic structure calculations for solids and molecules: Theory and Computational Methods*; Cambridge University Press: Cambridge, UK, 2006.

(110) Martin, R. M.: *Electronic structure: basic theory and methods*; Cambridge University Press: Cambridge, UK, 2004.

(111) Hohenberg, P.; Kohn, W.: Inhomogeneous Electron Gas. *Physical Review***1964**, *136*, B864-B871.

(112) Kohn, W.; Sham, L. J.: Self-Consistent Equations Including Exchange and Correlation Effects. *Physical Review***1965**, *140*, A1133-A1138.

(113) Dresselhaus M.S.; Dresselhaus G.; Eklund, P. C.: *Science of Fullerenes and Carbon Nanotubes*; Elsevier Inc.: Academic Press: San Diego, 1996.

(114) Bachilo, S. M.; Balzano, L.; Herrera, J. E.; Pompeo, F.; Resasco, D. E.; Weisman, R. B.: Narrow (n,m)-Distribution of Single-Walled Carbon Nanotubes Grown Using a Solid Supported Catalyst. *Journal of the American Chemical Society***2003**, *125*, 11186-11187.

(115) Miyauchi, Y.; Chiashi, S.; Murakami, Y.; Hayashida, Y.; Maruyama, S.: Fluorescence spectroscopy of single-walled carbon nanotubes synthesized from alcohol. *Chemical Physics Letters***2004**, *387*, 198-203.

(116) Zhang, M.; Yudasaka, M.; Iijima, S.: Production of Large-Diameter Single-Wall Carbon Nanotubes by Adding Fe to a NiCo Catalyst in Laser Ablation. *The Journal of Physical Chemistry B***2004**, *108*, 12757-12762.

(117) Gomez-Gualdron, D. A.; Balbuena, P. B.: Effect of Metal Cluster-Cap Interactions on the Catalyzed Growth of Single-Wall Carbon Nanotubes. *The Journal of Physical Chemistry C***2008**, *113*, 698-709.

(118) Gomez-Gualdron, D. A.; Balbuena, P. B.: Growth of chiral single-walled carbon nanotube caps in the presence of a cobalt cluster *Nanotechnology***2009**, *20*, 215601.

(119) Neyts, E. C.; van Duin, A. C. T.; Bogaerts, A.: Insights in the Plasma-Assisted Growth of Carbon Nanotubes through Atomic Scale Simulations: Effect of Electric Field. *Journal of the American Chemical Society*, *134*, 1256-1260.

(120) Abild-Pedersen, F.; Norskov, J.; Rostrup-Nielsen, J.; Sehested, J.; Helveg, S.: Mechanisms for catalytic carbon nanofiber growth studied by ab initio density functional theory calculations. *Physical Review B***2006**, *73*, 1-13.

(121) Helveg, S.; Lopez-Cartes, C.; Sehested, J.; Hansen, P. L.; Clausen, B. S.; Rostrup-Nielsen, J. R.; Abild-Pedersen, F.; Norskov, J. K.: Atomic-scale imaging of carbon nanofibre growth. *Nature***2004**, *427*, 426-429.

(122) Chiang, W.-H.; Sankaran, R. M.: Microplasma synthesis of metal nanoparticles for gas-phase studies of catalyzed carbon nanotube growth. *Applied Physics Letters***2007**, *91*, 121503-3.

(123) Chiang, W.-H.; Sankaran, R. M.: In-Flight Dimensional Tuning of Metal Nanoparticles by Microplasma Synthesis for Selective Production of Diameter-Controlled Carbon Nanotubes. *The Journal of Physical Chemistry C***2008**, *112*, 17920-17925.

(124) Chiang, W.-H.; Sankaran, R. M.: Synergistic Effects in Bimetallic Nanoparticles for Low Temperature Carbon Nanotube Growth. *Advanced Materials***2008**, *20*, 4857-4861.

(125) Chiang, W.-H.; Sankaran, R. M.: Relating carbon nanotube growth parameters to the size and composition of nanocatalysts. *Diamond and Related Materials***2009**, *18*, 946-952.

(126) Oyama, Y.; Saito, R.; Sato, K.; Jiang, J.; Samsonidze, G. G.; GrÃ¼neis, A.; Miyauchi, Y.; Maruyama, S.; Jorio, A.; Dresselhaus, G.; Dresselhaus, M. S.: Photoluminescence intensity of single-wall carbon nanotubes. *Carbon***2006**, *44*, 873-879.

(127) Kresse, G.; Furthmüller, J.: Efficient iterative schemes for ab initio total-energy calculations using a plane-wave basis set. *Physical Review B***1996**, *54*, 11169-11186.

(128) Perdew, J. P.; Chevary, J. A.; Vosko, S. H.; Jackson, K. A.; Pederson, M. R.; Singh, D. J.; Fiolhais, C.: Atoms, molecules, solids, and surfaces: Applications of the generalized gradient approximation for exchange and correlation. *Physical Review B***1992**, *46*, 6671-6687.

(129) Brinkmann, G.: A constructive enumeration of nanotube caps. *Discrete Applied Mathematics***2002**, *116*, 55-71.

(130) Ghorannevis, Z.; Kato, T.; Kaneko, T.; Hatakeyama, R.: Narrow-Chirality Distributed Single-Walled Carbon Nanotube Growth from Nonmagnetic Catalyst. *Journal of the American Chemical Society***2010**, *132*, 9570-9572.

(131) Ostrikov, K.; Mehdipour, H.: Thin Single-Walled Carbon Nanotubes with Narrow Chirality Distribution: Constructive Interplay of Plasma and Gibbsâ€“Thomson Effects. *ACS nano*, *5*, 8372-8382.

(132) Dutta, D.; Chiang, W.-H.; Sankaran, R. M.; Bhethanabotla, V. R.: Epitaxial nucleation model for chiral selective growth of SWCNTs on bimetallic catalyst surfaces. *Carbon***2012**, *50*, 3766-3773.

(133) Dai, H.; Rinzler, A. G.; Nikolaev, P.; Thess, A.; Colbert, D. T.; Smalley, R. E.: Single-wall nanotubes produced by metal-catalyzed disproportionation of carbon monoxide. *Chemical Physics Letters***1996**, *260*, 471-475.

(134) Moors, M.; Amara, H.; Visart de BocarmeÌ, T.; Bichara, C.; Ducastelle, F. o.; Kruse, N.; Charlier, J.-C.: Early Stages in the Nucleation Process of Carbon Nanotubes. *ACS nano***2009**, *3*, 511-516.

(135) Yu, X.; Zhang, J.; Choi, W.; Choi, J.-Y.; Kim, J. M.; Gan, L.; Liu, Z.: Cap Formation Engineering: From Opened C60 to Single-Walled Carbon Nanotubes. *Nano Letters***2010**, *10*, 3343-3349.

(136) He, M.; Chernov, A. I.; Fedotov, P. V.; Obraztsova, E. D.; Sainio, J.; Rikkinen, E.; Jiang, H.; Zhu, Z.; Tian, Y.; Kauppinen, E. I.; Niemelä, M.; Krause, a. O. I.: Predominant (6,5) single-walled carbon nanotube growth on a copper-promoted iron catalyst. *Journal of the American Chemical Society***2010**, *132*, 13994-6.

(137) Harutyunyan, A. R.; Chen, G.; Paronyan, T. M.; Pigos, E. M.; Kuznetsov, O. a.; Hewaparakrama, K.; Kim, S. M.; Zakharov, D.; Stach, E. a.; Sumanasekera, G. U.: Preferential growth of single-walled carbon nanotubes with metallic conductivity. *Science (New York, N.Y.)***2009**, *326*, 116-20.

(138) Zhou, W.; Han, Z.; Wang, J.; Zhang, Y.; Jin, Z.; Sun, X.; Zhang, Y.; Yan, C.; Li, Y.: Copper Catalyzing Growth of Single-Walled Carbon Nanotubes on Substrates. *Nano Letters***2006**, *6*, 2987-2990.

(139) Dumlich, H.; Robertson, J.; Reich, S.: Nanotube caps on Ni , Fe , and NiFe nano particles : A path to chirality selective growth. 1-25.

(140) Vanderbilt, D.: Soft self-consistent pseudopotentials in a generalized eigenvalue formalism. *Physical Review B***1990**, *41*, 7892-7895.

(141) Ahmed, J.; Ramanujachary, K. V.; Lofland, S. E.; Furiato, A.; Gupta, G.; Shivaprasad, S. M.; Ganguli, A. K.: Bimetallic Cu–Ni nanoparticles of varying composition (CuNi3, CuNi, Cu3Ni). *Colloids and Surfaces A: Physicochemical and Engineering Aspects***2008**, *331*, 206-212.

(142) Lin, P. A.; Sankaran, R. M.: Plasma-assisted dissociation of organometallic vapors for continuous, gas-phase preparation of multimetallic nanoparticles. *Angewandte Chemie (International ed. in English)***2011**, *50*, 10953-6.

(143) Odom, T. W.; Huang, J.-l.: Atomic structure and electronic properties of single-walled carbon nanotubes. *Nature***1998**, *391*, 1997-1999.

(144) Dumlich, H.; Reich, S.: Rims of carbon nanotubes – influence of chirality. *Physica Status Solidi (B)***2010**, *247*, 2722-2725.

(145) Woo, R. L.; Xiao, R.; Kobayashi, Y.; Gao, L.; Goel, N.; Hudait, M. K.; Mallouk, T. E.; Hicks, R. F.: Effect of Twinning on the Photoluminescence and Photoelectrochemical Properties of Indium Phosphide Nanowires Grown on Silicon (111). *Nano Letters***2008**, *8*, 4664-4669.

(146) Xu, H.; Wang, Y.; Guo, Y.; Liao, Z.; Gao, Q.; Tan, H. H.; Jagadish, C.; Zou, J.: Defect-Free <110> Zinc-Blende Structured InAs Nanowires Catalyzed by Palladium. *Nano Letters***2012**.

(147) Munshi, A. M.; Dheeraj, D. L.; Fauske, V. T.; Kim, D.-C.; van Helvoort, A. T. J.; Fimland, B.-O.; Weman, H.: Vertically Aligned GaAs Nanowires on Graphite and Few-Layer Graphene: Generic Model and Epitaxial Growth. *Nano Letters***2012**, *12*, 4570-4576.

(148) Kriegner, D.; Panse, C.; Mandl, B.; Dick, K. A.; Keplinger, M.; Persson, J. M.; Caroff, P.; Ercolani, D.; Sorba, L.; Bechstedt, F.; Stangl, J.; Bauer, G. n.: Unit Cell Structure of Crystal Polytypes in InAs and InSb Nanowires. *Nano Letters***2011**, *11*, 1483-1489.

APPENDIX A: COPYRIGHT PERMISSION FOR CHAPTER 4

ELSEVIER LICENSE
TERMS AND CONDITIONS

Jan 02, 2014

This is a License Agreement between Debosruti Dutta ("You") and Elsevier ("Elsevier") provided by Copyright Clearance Center ("CCC"). The license consists of your order details, the terms and conditions provided by Elsevier, and the payment terms and conditions.

All payments must be made in full to CCC. For payment instructions, please see information listed at the bottom of this form.

Supplier	Elsevier Limited The Boulevard,Langford Lane Kidlington,Oxford,OX5 1GB,UK
Registered Company Number	1982084
Customer name	Debosruti Dutta
Customer address	4202 E Fowler Avenue Tampa, FL 33613
License number	3300840747370
License date	Jan 02, 2014
Licensed content publisher	Elsevier
Licensed content publication	Carbon
Licensed content title	Epitaxial nucleation model for chiral-selective growth of single-walled carbon nanotubes on bimetallic catalyst surfaces
Licensed content author	Debosruti Dutta,Wei-Hung Chiang,R.Mohan Sankaran,Venkat R. Bhethanabotla
Licensed content date	August 2012
Licensed content volume number	50
Licensed content issue number	10
Number of pages	8
Start Page	3766
End Page	3773
Type of Use	reuse in a thesis/dissertation
Portion	figures/tables/illustrations
Number of figures/tables/illustrations	All